UNIVERSITY OF CALGARY

Aerothermodynamic Measurements in Hypersonic Non-Equilibrium Flows

by

Connor Charles McDougall

A THESIS

SUBMITTED TO THE FACULTY OF GRADUATE STUDIES

IN PARTIAL FULFILLMENT OF THE REQUIREMENTS FOR THE

DEGREE OF DOCTOR OF PHILOSOPHY

DEPARTMENT OF MECHANICAL AND MANUFACTURING ENGINEERING

CALGARY, ALBERTA

October, 2022

Abstract

High enthalpy arc-jets are unique facilities particularly suited for producing complex flows in the aerospace field, such as the aerothermodynamics of a re-entry vehicle. Arc-jets are often used to evaluate important design factors that include heat shield materials and vehicle design. Characterization of these facilities is important, as studies often aim to match specific in-flight environments during experiments. Due to the complex environment produced by an arc-jet, with effects such as thermodynamic and chemical non-equilibrium occurring in the flow, characterization experiments are significantly more difficult than in conventional blow-down wind tunnels. The current work aims to characterize an arc-jet facility through spatially-resolved measurements of flow unsteadiness, temperature, and velocity. To achieve this goal, a non-intrusive imaging technique called "planar laser-induced fluorescence" was performed in the NASA Langley Hypersonic Materials Environmental Test System arc-jet facility. The experimental data was analysed to produce the quantitative measurements in multiple regions of the flow around a blunt body specimen. A three-temperature low fidelity numerical solver was created to simulate the flow in order to investigate thermal non-equilibrium effects occurring outside the imaging region in the arc-jet nozzle. Unsteadiness in the test section of the arc-jet was minimized by analyzing a subset of data assessing the gas injection configuration. Radial velocity, rotational temperature and translational temperature measurements are provided that can be used to validate future computational studies. The temperature measurements revealed rotational non-equilibrium occurring behind the bow-shock near the specimen surface. Computational results show the facility is capable of producing thermal non-equilibrium flow in the arc-jet nozzle. This work provides the first experimental and computational evidence of thermal trans-rotational non-equilibrium occurring in multiple regions of this arc-jet facility. Significant improvements to the methodology are also identified as recommendations for future arc-jet characterization studies.

Acknowledgments

I would like to thank my family and Danika for their continued support over the years, my colleagues for their valuable insights on my research, our collaborators at NASA for the opportunity to acquire and work with an interesting data set, and my supervisor Dr. Craig Johansen for providing the opportunities for me to succeed in my studies.

Preface

The experimental campaign was performed at the Hypersonic Materials Environmental Test System arc-jet facility by a team of researchers from NASA Langley Research Center: Dr. Paul Danehy, Dr. Scott Splinter, Dr. Daniel Reese, Mr. Roland Stanzel, and Mr. Jeff Gragg. The author and the author's supervisor Dr. Craig Johansen were both present for the experiments and provided input on the experimental campaign. The rest of the thesis is solely the work of the author.

Table of Contents

List of Tables

List of Figures and Illustrations

List of Symbols, Abbreviations and Nomenclature

Symbol	Definition
χ	Fluorescence species mole fraction
β	Dimensionless time step constant
Δ_A	Absorption broadening
Δ_C	Collisional broadening
Δ_D	Doppler broadening
Δ_L	Spectral laser linewidth
Δ_P	Pressure broadening
ΔT_{CW}	Cooling system temperature difference
Δ_t	Time step
Δ_W	Arbitrary spectral width
δ_C	Collisional shift
δ_D	Doppler shift
δ_u	Translational fit parameter
δ_W	Arbitrary spectral shift
γ	Heat capacity ratio
γ_f	Collisional full-width half-maximum
λ	Mean free path
μ	Dynamic viscosity
η	Detector efficiency
ν	Laser spectral center
ν_o	Transition spectral center
Ω	Rotational temperature parameter for energy equation
Ω_d	Detector solid angle

θ	Vibrational temperature parameter for energy equation
ϕ	Translational temperature parameter for energy equation
Φ	Fluorescence yield
ρ	Density
σ	Quenching cross section
τ_c	Mean collision time
τ_r	Rotational relaxation time
τ_v	Vibrational relaxation time
A	Saturation analysis scaling parameter
A_e	Einstein spontaneous emission coefficient
A_r	Nozzle area ratio
B_{12}	Einstein absorption coefficient
B_{21}	Einstein stimulated emission coefficient
c	Speed of light
C_p	Heat capacity
$C1$	Landau-Teller vibrational relaxation constant
$C2$	Landau-Teller vibrational relaxation constant
CW	Flow rate of cooling water
ΔT_{CW}	Temperature difference across HyMETS water cooling system
e_{rot}	Rotational energy
e_{vib}	Vibrational energy
f''	Rotational ground state energy
F_B	Boltzmann fraction
F_b	Boltzmann factor
g	Vibrational energy function
G	Spectral overlap integral

h	Planck's constant
H_o	Bulk enthalpy
I_L	Laser irradiance
I_{SAT}	Saturation laser irradiance
I_o	Unabsorbed laser irradiance
J''	Rotational quantum number
k	Transition index for spectral peak thermometry
k_a	Absorption coefficient
k_o	Transition-independent absorption coefficient
K_B	Boltzmann constant
Kn	Knudsen number
l	Laser path length
m	Molecular mass
m_a	Molecular mass of absorber species
m_e	Collisional broadening constant
M_{total}	Mass flow rate of gas
n_e	Collisional shift constant
N_o	Number of absorbers
N_T	Number density
P	Pressure
Q_c	Collisional quenching coefficient
R	Specific gas constant
s	Saturation term
S_f	Fluorescence signal
T_{or}	Reference temperature
t_{det}	Camera detection time

T_t	Translational temperature
T_r	Rotational temperature
T_v	Vibrational temperature
u	Streamwise velocity
v''	Vibrational quantum number
V	Velocity parameter for momentum equation
V_o	Volume
V_r	Radial velocity
V_p	Physical volume
V_v	Voltage
w_d	Diatomic species mass fraction
W_A	Arbitrary scale parameter for DSV
W_B	Arbitrary scale parameter for SPT
W_C	Arbitrary scale parameter for DBT
x	Stream-wise location
X	Arbitrary computational variable
y	Transverse location
Z	Density parameter for continuity equation
Z_p	Partition function
Z_{inf}	Infinite temperature collision number

Abbreviation	Definition
a.u.	Arbitrary Units
ARC1D	Aerothermodynamic Relaxation Code
CFD	Computational Fluid Dynamics
DBT	Doppler Broadening Thermometry

DSV	Doppler Shift Velocimetry
FOV	Field Of View
HyMETS	Hypersonic Materials Environmental Test System
NLLS	Non-Linear Least Squares
MTV	Molecular Tagging Velocimetry
NO	Nitric Oxide
PLIF	Planar Laser-Induced Fluorescence
SPT	Spectral Peak Thermometry
SiC	Silicon Carbide
SLPM	Standard Litre Per Minute
SNR	Signal to Noise Ratio
TPS	Thermal Protection System

Chapter 1

INTRODUCTION

The hypersonic blunt body problem is critically useful for the design of atmospheric re-entry vehicles. These vehicles experience extreme heat loads on their leading surfaces as a result of the hypersonic velocity reached while ballistically entering the atmosphere [Anderson Jr, 1970; Ellington, 1963; Kang, 1970; Katzen and Kaattari, 1965; Park, 1993]. The heat transfer from the flow to the surface of the vehicle is dependent on the behavior of the chemical and thermal non-equilibrium multi-species flow in the region close to the vehicle [Edquist et al., 2009; Park, 1993]. A thermal protection system (TPS) is installed on the surfaces of re-entry vehicles to protect the vehicle from these environments. A TPS needs to be tested and characterized in a controlled setting prior to implementation to ensure it is capable of withstanding the expected flow conditions [Splinter et al., 2011]. The complex flow near the surface of a hypersonic blunt body is produced by the strong leading bow shock, which ionizes the oncoming flow and significantly changes the species composition near the vehicle [Anderson Jr, 1970; Park, 1993]. As a result, atmosphere species composition largely impacts the heat transfer to the vehicle surface [Park, 1993; Splinter et al., 2011]. The sudden change in conditions created by a strong bow shock also causes the energy partitions of diatomic and polyatomic molecules to drop out of equilibrium, producing energy differences between the translational, rotational, and vibrational modes. The energy partition theorem explains this effect, and is typically encountered in the thermodynamics field when investigating the heat capacities of molecules [Schroeder, 1999]. As illustrated in Figure 1.1, as the temperature of a diatomic gas increases, additional energy modes become available, resulting in a non-linear increase in heat capacity. However, in the hypersonic blunt body problem, the energy in these modes are unable to exchange energy with the other modes of the molecule in the time scale of the flow problem, resulting in a partitioned molecule where energy cannot leave each mode. In this case,

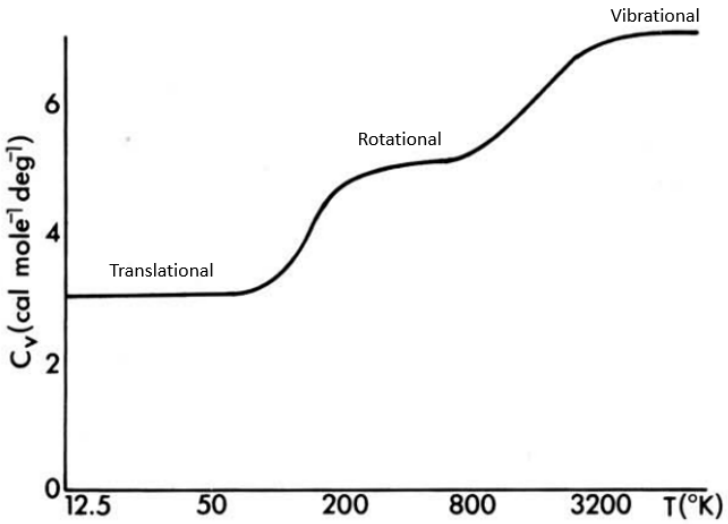

Figure 1.1: Heat capacity of diatomic hydrogen. Reproduced from Dence [1972].

the molecule has three distinct temperatures that describe its thermodynamic state, corresponding to the energy modes of the molecule [Anderson Jr, 1970]. This thermal non-equilibrium between each mode is often observed in high-speed low-density flow, where the mean free path does not allow for enough molecular collisions for these modes to achieve equilibrium [Anderson Jr, 1970; Parker, 1959]. The rate each mode exchanges energy with the translational mode varies by orders of magnitude, resulting in flows where the vibrational mode can be in non-equilibrium with the trans-rotational modes [Parker, 1959]. Furthermore, the chemical and thermal non-equilibrium effects produced by the bow shock are coupled, as the species composition of ionic, atomic, diatomic and polyatomic species impacts how energy is stored in the flow. Due to the diverse aerothermodynamic phenomena that occur in the hypersonic blunt body problem, non-equilibrium effects have large implications for the design of heat shields on re-entry vehicles [Anderson Jr, 2006].

TPS materials used on the surfaces of re-entry vehicles are typically tested in high-speed facilities where the properties of the flow can be controlled. Arc-heated ground test facilities, commonly known as arc-jets, are often used for TPS evaluation studies [Bose et al., 2013; Savino et al., 2010]. Arc-jets are capable of producing high-enthalpy flow conditions for long run times that simulate the re-entry environment, and are therefore ideal for TPS testing [Calomino et al., 2010; Savino

et al., 2010; Splinter et al., 2011; Zhang et al., 2008]. These facilities have been used extensively in the past sixty years to establish a better understanding of hypersonic flow around a blunt body (see Figure 1.2 for an experimental image from an early arc-jet experiment, from Hartman [1970]). Unfortunately, arc-jets are known to produce unsteady, thermal non-equilibrium, chemically reacting, radiating flows that are difficult to characterize accurately [Danehy et al., 2015; Inman et al., 2013]. Arc-jets do not exactly simulate the re-entry vehicle flow problem, as the flow is *already* in a state of non-equilibrium in the free-stream, whereas it is the strong bow shock in front of the vehicle that produces the non-equilibrium flow in flight. Knowledge of the flow properties prior to TPS testing is important for determining if the entry environment is being simulated as accurately as possible. The use of physical probes (e.g., slug calorimeters, pitot tubes) and non-intrusive optical diagnostics (e.g., laser-induced fluorescence (LIF), molecular tagging velocimetry (MTV), and emission spectroscopy) have been used to characterize some arc-jet facilities [Danehy et al., 2012; Grinstead et al., 2011, 2003; Liebeskind et al., 1993; Johansen et al., 2016; Rob et al., 1997; Splinter et al., 2011; Winter et al., 2018, 2019]. Additionally, a significant effort has been made in previous works to simulate the arc-jet environment using non-equilibrium computational fluid dynamics (CFD) simulations [Brune et al., 2019; Davuluri et al., 2016; Düzel et al., 2019; Sakai et al., 2007; Ventura Diaz et al., 2019]. These complex non-equilibrium computational solvers need to be validated using accurate experimental measurements of multiple aerodynamic, thermodynamic and chemical flow properties. If these models are not validated using experimental data, it is difficult to interpret whether the computational results are accurately representing the flow in the facility.

LIF is a laser-based optical technique that can produce accurate, time-averaged measurements of multiple aerodynamic and thermodynamic properties [Bessler and Schulz, 2004; Bathel et al., 2011; Kychakoff et al., 1982; Ivey et al., 2011; Inman et al., 2013; McDougall et al., 2020b, 2018a,b; Palma et al., 1999]. A short-wavelength pulsed laser is used to radiatively excite a tracer species within the flow, which subsequently gives off long-wavelength radiation that is captured by

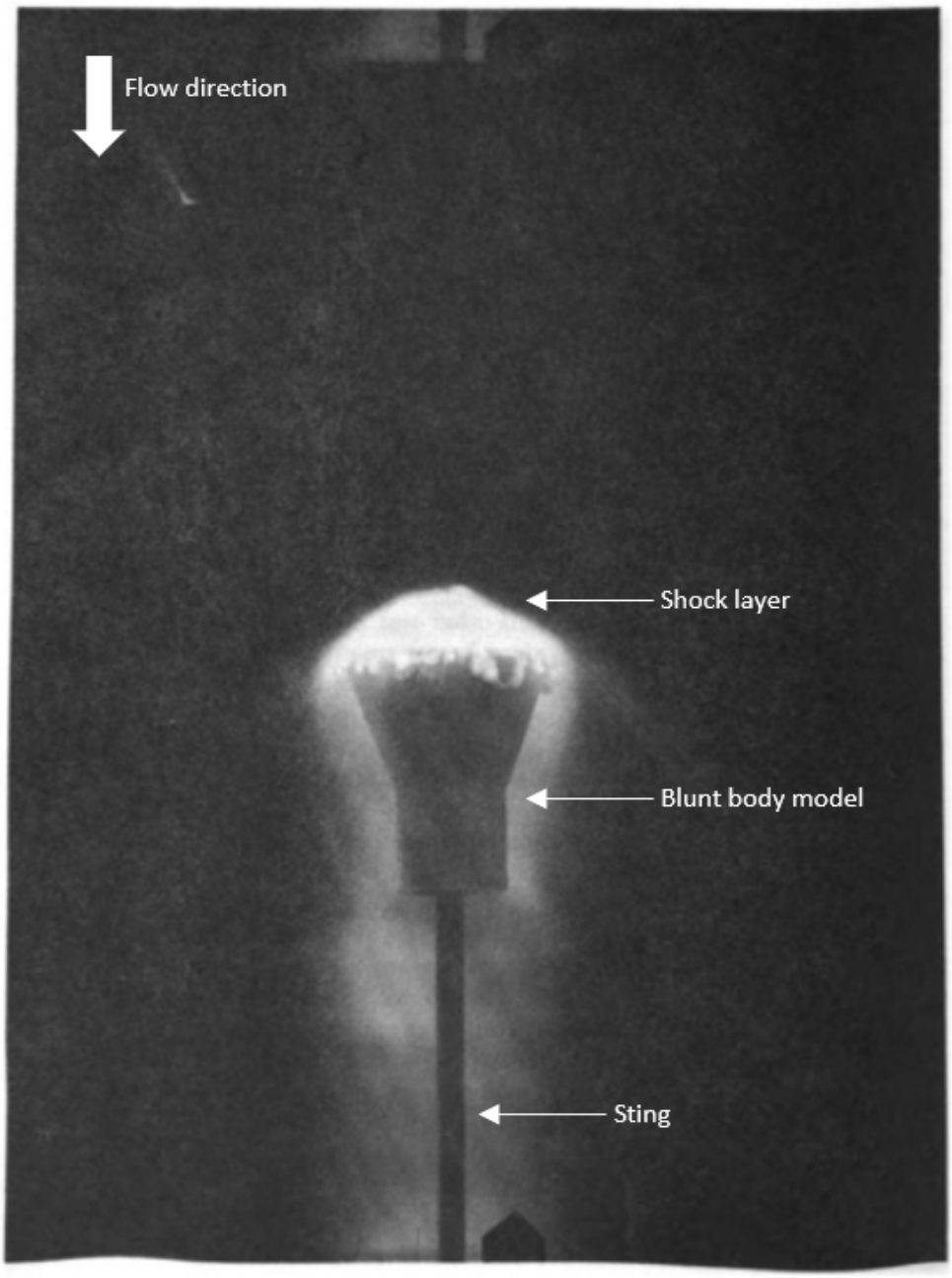

Figure 1.2: A blunt body experiment within an arc-jet facility at NASA Ames Research Center in the 1960's. Adapted from "Adventures in Research: A History of Ames Research Center" by Hartman [1970].

a detector or camera. The long wavelength emission is dependent on the thermodynamic, chemical and flow properties of the surrounding flow, and therefore can be used to make quantitative measurements. LIF can also produce 2D spatially-resolved measurements if a laser sheet is used in place of a laser beam, known as planar LIF (PLIF). LIF/PLIF have been successfully used in a wide variety of high-speed flow experiments to measure quantitative variables [Bathel et al., 2011; Bessler and Schulz, 2004; Inman et al., 2013; Ivey et al., 2011; McDougall et al., 2018b, 2020a; Yoo et al., 2010]. Arc-jets present a challenging environment in which to acquire time-averaged quantitative PLIF measurements due to a long laser path length, large variation in saturation and absorption effects in flow regions within the facility, and unsteady flow properties. These facility characteristics introduce significant systematic errors in the interpretation of PLIF spectra in each region of the flow. Correcting the PLIF spectra for these effects is difficult, as absorption and saturation corrections often require knowledge of the thermodynamic and flow properties of each region *a priori*. Multiple studies in the literature have observed asymmetry in quantitative PLIF measurements radially across the jet, when the expected result was a symmetric property profile [Inman et al., 2013; Kirschner et al., 2018]. These observations are likely due to saturation and absorption effects, both of which are spatially and spectrally dependent. Currently no solution to this problem exists in the literature, apart from attempting estimated corrections to these complex effects [Inman et al., 2013; McDougall et al., 2020a]. Although there are drawbacks to completing time-averaged quantitative PLIF in arc-jet facilities, there are a number of advantages for using these facilities. Arc-jets can typically be operated on run times orders of magnitude larger than shock tube or blow-down wind tunnel facilities (hours vs. seconds), and for relatively lower operational cost. Therefore arc-jets can produce large comprehensive data sets for relatively low investment [Splinter et al., 2011].

Computational studies of arc-jets have been completed in the literature to capture the complex physics occurring in the facility. These studies have produced varying results for similar testing conditions [Brune et al., 2019; Düzel et al., 2019]. Due to the extreme environments within an arc-

jet, the computational modelling of these effects can be difficult to implement accurately [Brune et al., 2019]. To reduce computation time, certain phenomena are removed from the computational models if they are believed to be negligible compared to other physics occurring in the flow. These studies have been compared to experimentally measured velocity fields and slug calorimeter heat flux measurements in arc-jets [Brune et al., 2019; Inman et al., 2013], but a comprehensive comparison to experimental measurements has not been completed. Computational models which are thoroughly verified and validated against arc-jet experimental measurements would be highly valuable, as a wider range of test conditions could instead be simulated rather than requiring an arc-jet facility for experimental evaluation.

1.1 Objectives

The flow within arc-jets is highly complex, and has not been comprehensively characterized in the literature, either experimentally or computationally. This lack of characterization is due to traditional quantitative imaging techniques being insufficient "as is" for application to an arc-jet flow. Therefore, this work aims to provide a marked improvement in the experimental measurement of aerothermodynamic variables in an arc-jet flow by correcting for significant systematic errors, and accurately quantifying uncertainty. The focus of the current work is to provide a partial characterization of the aerothermodynamic state (flow unsteadiness, radial velocity, translational/rotational temperatures) in flow regions within an arc-jet facility. Additionally, a low-fidelity, thermal non-equilibrium, quasi-1D computational solver is developed to investigate the arc-jet flow in the optically-inaccessible nozzle. To summarize, the main objectives of the current work are:

1. Tailor existing PLIF acquisition and analysis techniques to unsteady non-equilibrium flows in order to experimentally measure aerothermodynamic properties of an arc-jet facility.

2. Adapt an existing numerical solver to model thermal non-equilibrium in order to

produce computational property predictions in the optically-inaccessible arc-jet nozzle.

3. Investigate the degree of thermal non-equilibrium occurring in the facility through interpretation of the experimental measurements and computational predictions.

A review of the literature covering experimental and computational studies in arc-jets is presented in Chapter 2. The physics that governs LIF emission is detailed in Chapter 3. In the current work, a campaign of nitric oxide (NO) PLIF experiments was designed and performed in the Hypersonic Materials Environmental Test System (HyMETS) arc-jet at NASA Langley Research Center. A detailed explanation of the HyMETS NO-PLIF experimental set-up and campaign is presented in Chapter 4. Chapter 5 begins with an overview of the analysis procedure to provide a clear guide for the subsequent chapters in the thesis, followed by a description of the image processing steps and initial studies completed prior to the main quantitative measurements. The measurement methodology for the velocity and temperature measurements is presented in Chapter 6. Chapter 7 details the low-fidelity solver developed in the current work. All experimental and computational results, along with discussion and interpretation, are presented in Chapter 8. Significant contributions by the current work and recommendations for future work in this area are summarized in Chapter 9.

Chapter 2

LITERATURE REVIEW

To understand the contributions of the present work, a review of the literature is presented that details arc-jet experimental studies, non-equilibrium computational studies simulating conditions similar to an arc-jet, and quantitative LIF studies. This chapter begins with an overview of the design of an arc-jet as these components are referred to throughout the current work.

2.1 Arc-jet design

An arc-jet facility consists of many components, but of primary interest in the current work are the arc-generator, the nozzle, the test section, and the test specimen. These components are shown in Figure 2.1, which is a schematic of the NASA Ames Interaction Heating Facility arc-jet. This general design is similar to the arc-jet facilities discussed in the current chapter.

The arc-generator consists of a cathode and anode located at opposite ends of a hollow cylindrical chamber. A voltage is applied across these two components such that an electric arc forms down the center of the cylinder. Test gasses are injected into the chamber and are energized by the arc, producing a high pressure, high enthalpy chamber of gas. This gas moves through a region called the plenum before being expanded through a converging-diverging nozzle directed into the test chamber of the facility, where optical windows are located to observe the high-speed flow. Optionally, a test specimen or physical probe (such as a pitot tube or calorimeter) can be placed into the flow for observation. The terminology described here will be referred to in the following sections and chapters.

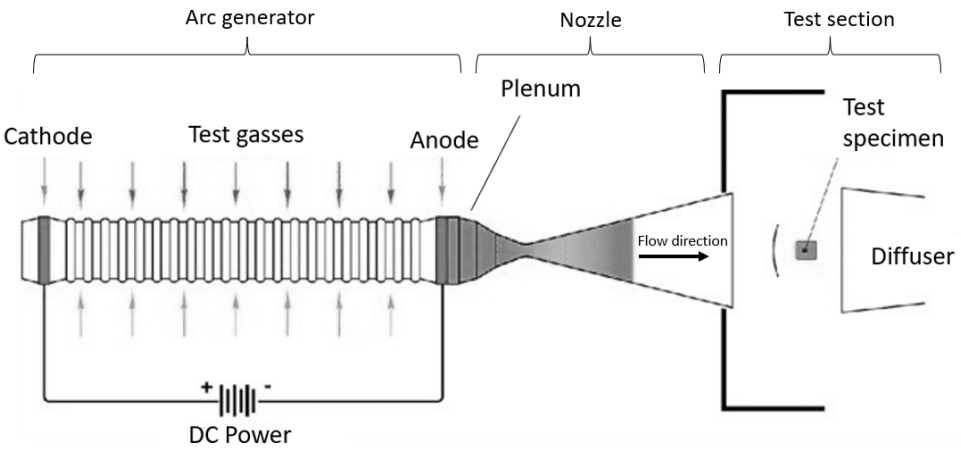

Figure 2.1: A schematic of the NASA Ames Interaction Heating Facility arc-jet, adapted from Grinstead et al. [2005]. This schematic generally represents the design of most arc-jet facilities.

2.2 Arc-jet experimental studies

This section is focused on studies that gathered experimental measurements of the flow within an arc-jet around a blunt body. Previous work has studied blunt bodies in an arc-jet, ranging from surface coating evaluations, surface temperature measurements, and free-stream quantitative measurements. Gaining perspective on these studies in terms of their contributions and suggestions for future work in the field is important for the design of the current study.

Splinter et al. [2011] conducted a comprehensive study of the capabilities and run conditions possible in the HyMETS arc-jet facility. This study also compared the surface heat flux on a slug calorimeter for Martian and Earth atmospheric compositions. The work additionally provides a thorough reference of uncertainties of the probes used for stagnation pressure and heat flux measurements. The study describes the method to determine the flow enthalpy for experiments completed in the facility (energy balance dependent on facility sensors for flow rate, coolant temperature change, and current/voltage measurements).

Knowledge of the flow enthalpy within arc-jets is critically important when matching computational studies to experimental arc-jet data. Pope [1968] studied methods of determining the enthalpy of low-density arc-jet flows in the 1960's, and determined that the options available to

measure flow enthalpy have high associated uncertainties. Park et al. [2006] also completed a more recent study focused on comprehensively evaluating arc-jet enthalpy calculation methods. The conclusions from this study were similar and found that enthalpy is a complex property to measure in arc-jets [Park et al., 2006]. More recently, a promising method of producing a plenum enthalpy profile through an iterative correction with a slug calorimeter in the flow was presented by Brune et al. [2019].

Savino et al. [2010] studied differences between various ultra-high temperature ceramic models in a high enthalpy hypersonic flow. The models used were a variety of blunt and streamlined bodies. Surface temperatures were measured using a combination of in-model thermocouples, infrared spectroscopy and a pyrometer. The models were able to be tested for several minutes at a time in the high temperature non-equilibrium flow to gather information about the heating effects on the models under sustained exposure to the non-equilibrium flow conditions. Bailey et al. [2018] studied ablative heat shields in an arc-jet, tracking particles ejected from the shield due to spallative events to determine their effect on total ablation rate. These studies both used arc-jets in the evaluation of the thermal response of high temperature heat shield materials.

Danehy et al. [2012] studied the spectral radiance of the flow within the HyMETS arc-jet across the bow shock in front of a flat-faced blunt body specimen. The purpose of this study was to identify species present in the flow at specific enthalpy conditions. Shock stand-off distances were estimated using the results and compared to expected values. A major finding from this study was that the spectroscopic data acquired was not repeatable over multiple experiments (15 - 100% differences) and indicates the flow composition changed significantly between experimental runs. Johansen et al. [2016] conducted simultaneous NO/O LIF in the HyMETS facility to investigate the presence of NO and O-atom species in the arc-jet flow, and compare their relationship over varying enthalpy conditions. The NO fluorescence followed predicted equilibrium trends at lower enthalpies, but O-atom LIF deviated significantly from the expected fluorescence signal trend, as shown in Figure 2.2. Additionally, this study investigated shot-to-shot correlations between the

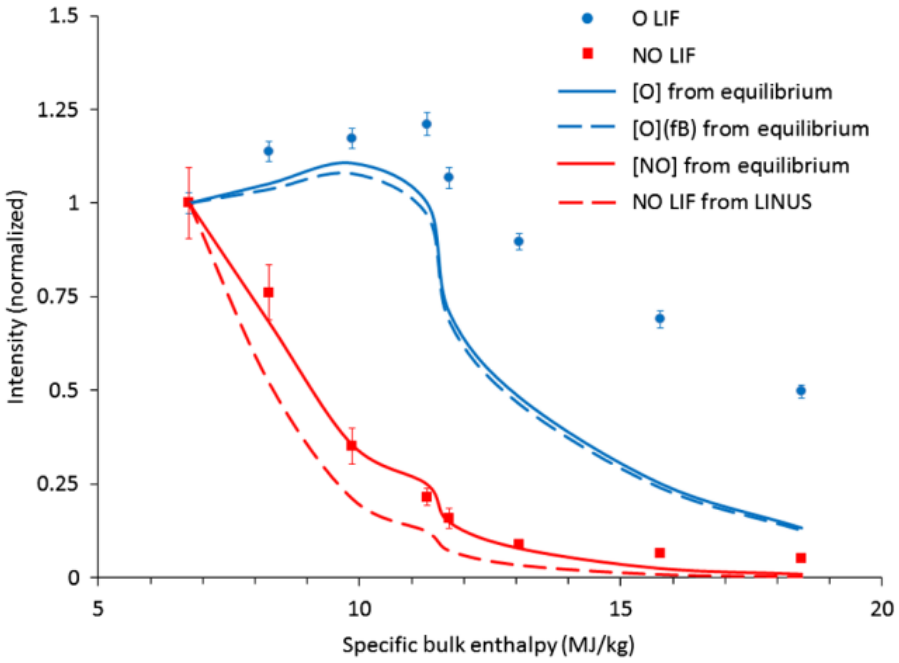

Figure 2.2: Normalized intensities of O and NO fluorescence compared to equilibrium calculations in the HyMETS arc-jet. Reproduced from Johansen et al. [2016].

species. The results showed significant differences in fluid composition with enthalpy condition, but there were no correlations in the shot-to-shot data.

Gopal et al. [2021] were the first to apply "Femtosecond Laser Electronic Excitation Tagging" to an arc-jet flow to obtain velocity measurements. Significant efforts were made to remove or reduce the background radiation in the images such that the tag emission could be tracked accurately, which is used to produce an accurate velocity measurement. Inman et al. [2013] performed NO-PLIF in the HyMETS arc-jet facility. This study provided flow visualization and quantitative radial and flow-direction velocity measurements. Significant efforts were made to correct for laser-path absorption through the core flow of the facility. This study was restricted to the free-stream region of the facility in front of the sample injection point. Inman et al. [2013] also measured the Doppler shift of NO-PLIF in the HyMETS arc-jet in the free-stream region immediately after the nozzle exit. This study produced a full-field of radial velocity measurements, as shown in Figure 2.3. Additionally, MTV measurements were produced in the same study to measure the axial velocity

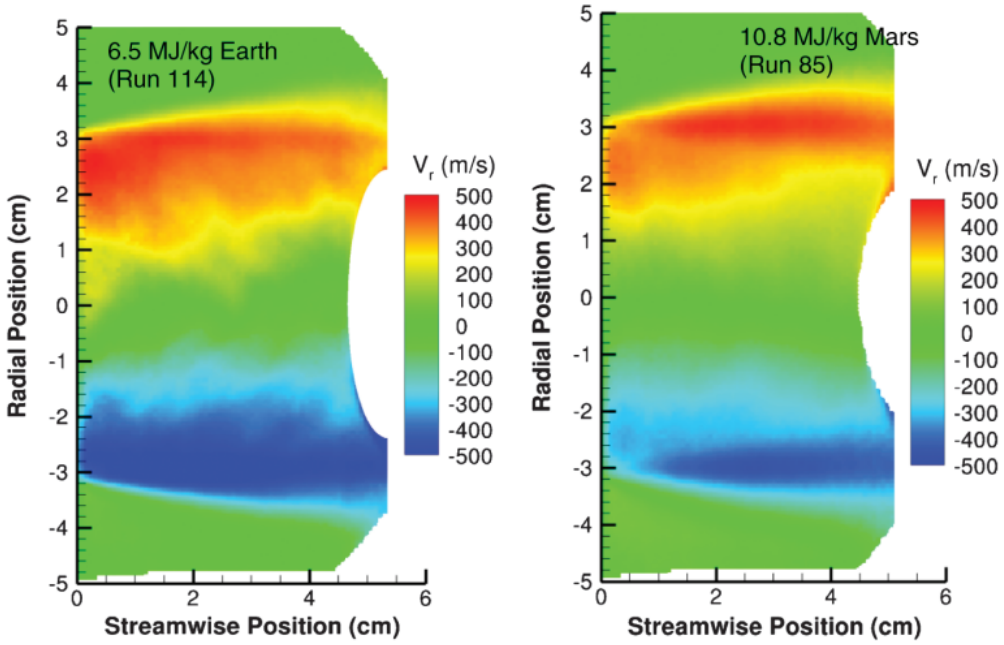

Figure 2.3: Radial velocity field measured in the HyMETS arc-jet at two enthalpy conditions. Reproduced from Inman et al. [2013].

field in the same imaging region. A study by Palmer and Hanson [1993] completed single-shot Doppler velocimetry in an arc-jet using NO-PLIF. The experiment used a broadband excitation of a transition imaged using two cameras to capture the radial and axial components of the velocity field. The results agreed well with a method of characteristics prediction. These laser-based experimental studies described were successfully designed for the complex arc-jet conditions, such that meaningful quantitative information was produced.

Blackwell et al. [1997] measured profiles of rotational and vibrational temperatures in the bow shock layer in front of a blunt body by analyzing natural emissions from nitrogen in the flow. Significant differences in vibrational and rotational energies were detected, indicating the vibrational mode had frozen in the free-stream after the nozzle. This method has been applied to multiple other non-equilibrium flows with varying levels of success [Winter and Auweter-Kurtz, 1998; Passaro et al., 2011]. These studies did not measure the translational temperature of the flow.

Winter et al. [2012] investigated the radiative heat flux from the arc chamber impinging on a sample injected into the the freestream of the NASA Ames Interaction Heating Facility. A

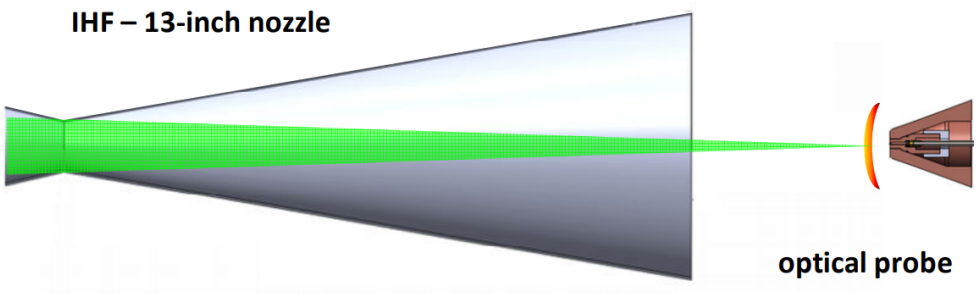

Figure 2.4: A radiative emissions experiment to determine if radiation from the arc chamber impinging on the sample surface was a significant source of heat transfer. Reproduced from Winter et al. [2012].

schematic of their experimental set-up is shown in Figure 2.4. This study completed experiments at bulk enthalpies of 8-24 MJ/kg. The study concluded that radiative heat transfer was negligible to the total heat flux impinging on the surface of the injected specimen. This result ruled out the hypothesis that radiative heat flux originating from the plenum contributed to calorimeter-based heat flux measurements in the NASA Ames Interaction Heating Facility, which could have been a significant design flaw in arc-jets.

2.3 Non-equilibrium computational studies

There are many groups that have studied various levels of non-equilibrium in hypersonic flows. This section focuses on studies that simulated an arc-jet facility for the purposes of computational model validation, and included some level of non-equilibrium modelling. Additional non-equilibrium studies are included that produced relevant results that are needed for the interpretation of the current study results.

Gokcen [1996] numerically solved the axisymmetric Navier-Stokes equations to determine the effects of non-equilibrium flows on convective heat transfer over a hemispheric blunt body. This study aimed to determine if arc-jets were appropriate facilities for simulating in-flight conditions. The work accounted for non-equilibrium effects using a three-temperature thermochemical model. The goal of the study was to determine differences between an arc-jet flow where non-equilibrium

occurs in the free-stream, and free-flight where the free-stream is in equilibrium. The study focused on convective heat transfer to the surface of the blunt body for free-stream and arc-jet conditions. The study concluded that under certain conditions, the convective heat transfer to the surface of an in-flight vehicle could be produced in an arc-jet facility for similar conditions.

Brune et al. [2019] simulated the axisymmetric geometry of the HyMETS arc-jet with a blunt body inserted into the test section using the "Langley Aerothermodynamic Upwind Relaxation Algorithm", producing predictions to compare to experimental velocity profiles produced by Inman et al. [2013]. The study achieved close agreement between the simulations and the velocimetry from Inman et al. [2013]. A diagram of their computational domain is shown in Figure 2.5. Additionally, the group obtained experimental measurements at the HyMETS facility, acquiring heat flux measurements at various enthalpy conditions using a slug calorimeter. This data was further used to validate their solver by comparing simulated heat flux to experimental heat flux. The heat flux measurement was also used in a novel iterative method developed by the group to determine the plenum enthalpy profile, which was then used as an initial condition for the simulations. The study presented multiple simulations at varying assumptions of catalytic efficiency at the surface of the test specimen, and then matched the catalytic efficiency to the simulation that best matched the experimental heat flux reading. Through this study, it was determined that the surface of the slug calorimeter had approximately a 10% catalytic efficiency. A similar study was completed by Ventura Diaz et al. [2019] that examined various blunt bodies under similar conditions. This study achieved close agreement with heat flux data taken at the HyMETS facility. Finally, Düzel et al. [2019] simulated the HyMETS arc-jet using the "Kentucky Aerothermodynamics and Thermal response System" CFD software, and used a similar methodology as Brune et al. [2019]. However, they used a constant enthalpy profile in the radial direction across the plenum, and a smaller blunt body sample. The velocity field produced by this study also achieved close agreement with the experimental data provided by Inman et al. [2013].

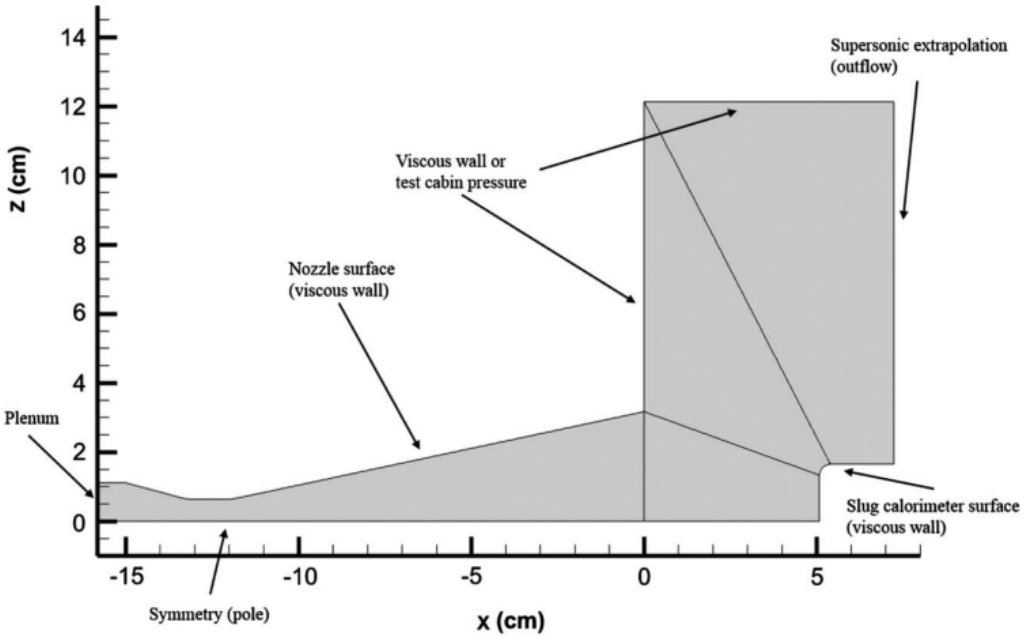

Fig. 7 Computational grid layout for arcjet flow CFD simulations.

Figure 2.5: Computational domain depicting the HyMETS arc-jet facility. Reproduced from Brune et al. [2019].

Gardner and Agarwal [2019] simulated a blunt body in a Mach 7.1 flow with a three temperature model. This study found that at large Knudsen numbers (0.001 and above) trans-rotational non-equilibrium effects began to occur as the flow crossed the bow shock in front of the blunt body, as shown in Figure 2.6. The rotational and translational modes decoupled crossing the shock, and attained a much lower post-shock rotational temperature than the translational temperature. As the flow becomes more rarefied, the Knudsen number increases, and the non-equilibrium effect becomes more prominent in the data. Additionally, the bow shock begins to "blur" when Knudsen number is increased, as rarefied molecular effects begin to affect the shock. A major outcome of this work was to show the transition to the trans-rotational non-equilibrium regime and at which Knudsen numbers this transition occurs at.

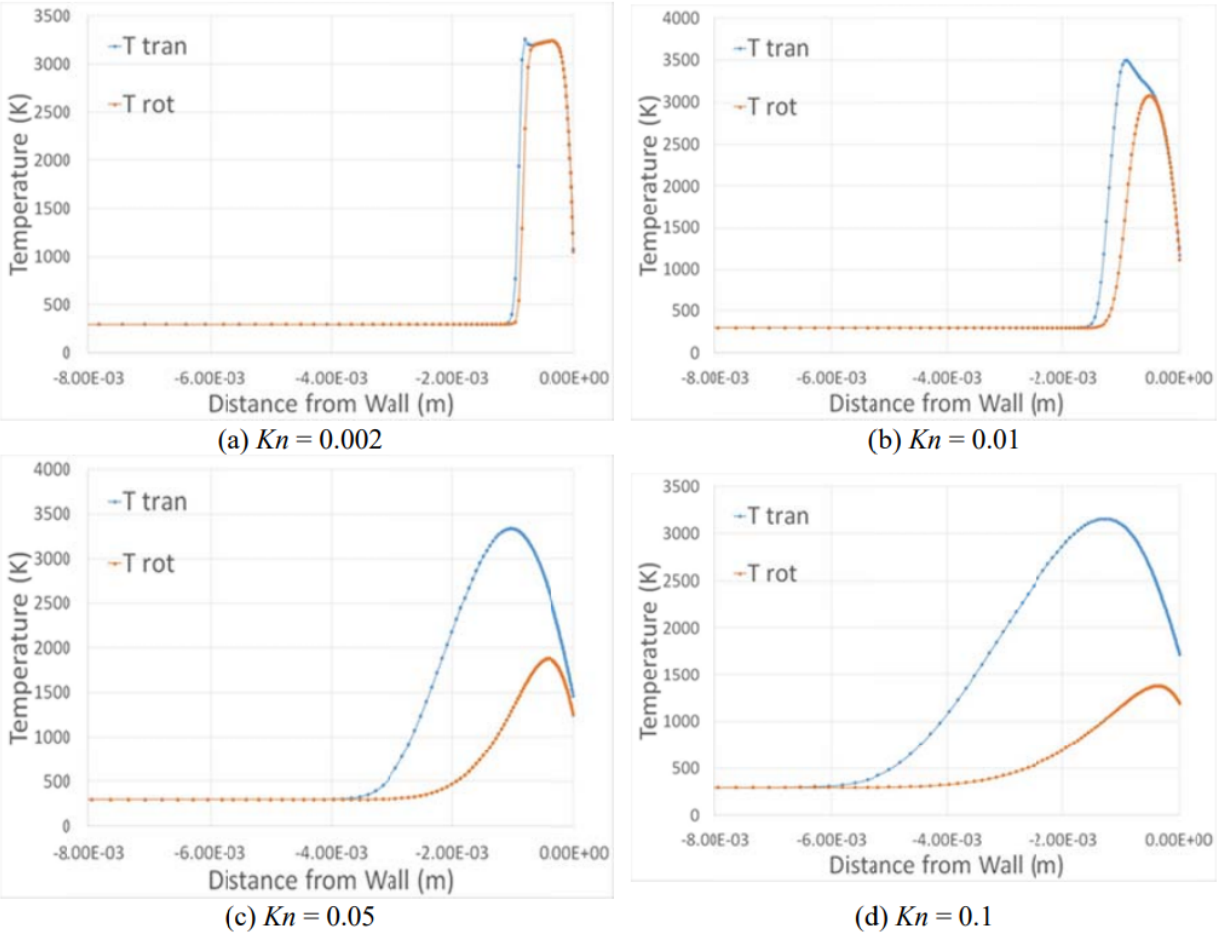

(a) $Kn = 0.002$ (b) $Kn = 0.01$

(c) $Kn = 0.05$ (d) $Kn = 0.1$

Figure 2.6: Trans-rotational non-equilibrium in a high Knudsen number blunt body flow. Reproduced from Gardner and Agarwal [2019]. Note that "distance from wall" indicates the distance from the surface of a flat-faced blunt body sample.

2.4 Quantitative laser-induced fluorescence experiments

LIF has been widely used in a variety of flow problems to make quantitative measurements. This section will focus on NO-LIF quantitative experiments completed in supersonic and hypersonic flows.

Sánchez-González et al. [2012] developed the "Vibrationally Excited NO Monitoring" technique that probes two rotational states of NO to achieve simultaneous velocity and temperature field measurement in a single experiment. The technique requires a specific laser and camera set-up to be completed. The results from this technique have been applied in a multitude of studies, achieving high quality thermometry results [Sánchez-González et al., 2012; Sánchez-González and North, 2018; Pan et al., 2016].

Palma et al. [1998] studied the flow around a cylinder in a shock tunnel, imaging the regions in the free-stream, post-shock, and wake of the cylinder. The study fit the PLIF spectra using NO fluorescence modelling. This method involved measuring the relative amplitudes of the spectral peaks and extracting the rotational temperature by fitting the data to a Boltzmann distribution (the function that describes the thermodynamic state of the energy levels of a molecule at a specific temperature). The work identified saturation as a significant confounder in the results, and work was undertaken to minimize the laser energy to ensure the spectra was unsaturated, while still preserving sufficient signal-to-noise ratio (SNR). The study successfully produced rotational temperature fields in the free-stream, post-shock and aft-body regions of the cylinder. Barker et al. [1998] also conducted NO-PLIF imaging experiments of a cylinder in a supersonic wind tunnel. This experiment measured the free-stream and wake temperatures of the flow, achieving significantly higher precision in the free-stream due to transients in the wake that affects the time-averaging of most PLIF thermometry methods.

Kaseman et al. [2017] used NO-PLIF to study the hypersonic flow around a 30 degree wedge in a shock tunnel. The study measured the temperature across the oblique shock formed in front of the wedge. A notable observation made in this study was the presence of "fluorescence bleed",

where strong signal on one side of the shock "bled" into the other flow region, increasing the detected signal, and therefore introducing a systematic error to the thermometry results. McDougall et al. [2020a] also used NO-PLIF in a wedge flow while instead focusing on the boundary layer. The study injected NO through a seeding slot near the front of the wedge, such that NO would diffuse into the boundary layer for imaging downstream. The study evaluated temperature dependence of multiple spectral peaks and quantified Doppler broadening to measure temperature in the boundary layer of a wedge injected into a hypersonic wind tunnel. This study identified spectral line saturation, laser absorption, and facility fluorescence reflections as significant confounders to the results, and suggested that these effects need to be quantified and corrected prior to applying typical quantitative measurement methodologies. This study closely matched the thermometry produced by a CFD study of the identical flow conditions [Arisman et al., 2013].

Chapter 3

FLUORESCENCE MODELLING

This chapter outlines the NO-LIF modelling utilized in the current work. This fluorescence model forms the basis of the measurement methodology that will be applied to the experimental NO-PLIF data in later chapters.

3.1 Two-level model

The current work utilizes the two-level model, which is a simplification of NO-LIF physics [Palma et al., 1999]. This model reduces the complexity of the energy levels of NO to only considering the ground state and excited state of a specific "transition" [Palma et al., 1999]. If the energy of an incident photon matches this energy gap between the ground and excited states (i.e. the transition), the ground state population can absorb the photon, and become promoted to the higher energy state. In this way, photons of a specific frequency can promote a percentage of the total ground state population to the excited energy level. In NO-LIF, the photons are delivered to NO through a pulsed single-wavelength laser in order to tune to a specific transition's energy gap. Once the source of the photons is removed (ie. the pulse ends), the system moves towards equilibrium, and population from the excited state begins to drop to the ground state through a process called a fluorescence cascade, where long wavelength radiation is emitted from the absorber at multiple intermediate energy levels, finally leading the absorber to the ground state [Di Rosa, 1996; Engleman, 1970; Palma et al., 1999]. The LIF emission is then captured by a camera system. Since the emission is proportional to the absorption of the laser light, the two-level model does not need to account for the intermediate energy levels, and only captures the absorption physics of the two energy levels.

3.2 Fluorescence equation

The two-level model can be represented by the governing equation below [Palma et al., 1999]:

$$S_f = \frac{1}{1+s}\chi N_T B_{12} F_B I_L G \Phi t_{det} V \frac{\Omega_d}{4\pi}\eta \tag{3.1}$$

where s, χ, N_T, B_{12}, F_B, I_L, G, Φ, t_{det}, V_o, Ω_d, η represent the saturation parameter, fluorescence species mole fraction, total population of absorbers per unit volume, Einstein B absorption coefficient, Boltzmann fraction, laser irradiance, spectral overlap integral, fluorescence yield, detection time of the detector/camera, volume probed by the laser, detection solid angle, and the detector efficiency of the camera being used, respectively [Palma et al., 1999; Reisel et al., 1992; Engleman, 1970]. The equation is derived from the fluorescence steady rate equations when considering a two-level system of energy levels [Palma et al., 1999]. The following subsections will detail each term in the equation and identify signal dependencies on velocity as well as rotational and translational temperature which will be utilized for quantitative measurements in the current work.

3.2.1 Population of absorbers

The number of absorbers per unit volume (N_T) term can be obtained by using the ideal gas law in Boltzmann form:

$$PV_p = N_o K_B T \tag{3.2}$$

where N_o is the number of absorbers, T is the temperature (K), P is the pressure (Pa), K_B is the Boltzmann constant, and the physical volume V_p. This equation can be rearranged to obtain the number of absorbers per unit volume N_o/V:

$$N_T = \frac{N_o}{V_p} = \frac{P}{K_B T} \tag{3.3}$$

3.2.2 Einstein absorption coefficient

The Einstein absorption coefficient (B_{12}) represents the probability of an incident photon at the transition frequency of being absorbed by NO. Each transition has a unique coefficient specific to the transition. Coefficient values were sourced from Reisel et al. [1992] for use in the current work.

3.2.3 Spectral overlap integral

The spectral overlap integral (G) accounts for overlap between the laser lineshape and the transition absorption lineshape. Due to broadening effects, the absorption line and laser line are not a single frequency, and therefore not a specific energy. The absorption lineshape can be affected by collisional and thermal (Doppler) broadening effects, while the laser lineshape can be broadening as a part of the process used by the hardware to create the laser beam. If a laser is spectrally scanned over a transition, the resulting fluorescence spectra is a convolution of the laser lineshape with the absorption lineshape. This convolution produces what is known as a Voigt profile (convolution of a Gaussian absorption lineshape with a Lorentzian laser lineshape). In the literature, an approximation to the Voigt profile has successfully been applied to other NO-PLIF experiments in order to gain an analytical solution. Instead of Lorentzian broadening mechanisms, all mechanisms are approximated as having a Gaussian lineshape [Ivey et al., 2011]. This is known as the triple Gaussian approximation:

$$G_\nu = \sqrt{\frac{4\ln(2)}{\pi[\Delta_D^2+\Delta_C^2+\Delta_L^2]}}\exp\Big(-4ln(2)\frac{[(\nu-\nu_o+\delta_C+\delta_D)]^2}{\Delta_D^2+\Delta_C^2+\Delta_L^2}\Big) \tag{3.4}$$

where ν is the laser wavenumber, and ν_o is the center transition wavenumber, and G_ν is the spectral overlap integral for a spectral scan across a transition. δ and Δ are spectral shift and spectral broadening terms, respectively, and are defined in the following subsections.

3.2.4 Collision broadening & shift

Collisional broadening (Δ_C) is known as a homogenous broadening mechanism, meaning that all absorbers are affected equally. Due to collisions between absorbers, the absorption and emission process is affected [Di Rosa, 1996]. This effect introduces a Lorentzian profile to the absorption lineshape as broadening becomes significant. The function describing a collisional-broadened transition is given by:

$$F_C(\nu) = \frac{\Delta_C/4\pi^2}{(\nu - \nu_o + \Delta_{cs})^2 + (\Delta_C/4\pi)^2} \tag{3.5}$$

where the width of this Lorentzian profile, Δ_C, is the collisional broadening term. This term can be determined using the following empirical formula from Di Rosa [1996]:

$$\Delta_c = P\sum_i 2\chi\gamma_f^{T_o}(\frac{T_o}{T_t})^{m_e} \tag{3.6}$$

where m_o is an experimentally measured exponent, T_o is a reference temperature, T_t is the translational temperature, γ_f is the full-width half-maximum (FWHM) collision width per unit pressure, and P is pressure. Collisions also introduce a shift (δ_C) in the center frequency of the transition, and can be determined using the following empirical formula [Di Rosa, 1996]:

$$\Delta_{cs} = P\sum_i \chi\delta_c^{T_o}(\frac{T_o}{T_t})^{n_e} \tag{3.7}$$

where δ is the collision shift per unit pressure, and n_e is an experimentally measured exponent.

3.2.5 Doppler broadening & shift

Due to the Doppler effect, a moving absorber either parallel or anti-parallel to the laser propagation direction will experience a shift in absorption frequency. On a scale where there are multiple absorbers with relatively random motion, the resulting effect is a broadening of the absorption lineshape. This movement is dependent on translational temperature. Therefore, as the translational temperature increases, the Doppler broadening term grows larger. Additionally, if the group of

absorbers as a whole is moving with a uniform velocity, the center frequency of the absorption line can shift. These two effects are known as Doppler broadening and Doppler shift, given by the following equations:

$$\Delta_D = \frac{2\nu_o}{c}\sqrt{\frac{2ln(2)K_B T_t}{m}} \tag{3.8}$$

$$\delta_D = \frac{\nu_o V_r}{c} \tag{3.9}$$

where c is the speed of light, m is the molecular mass, V_r is the velocity of the absorbers parallel or anti-parallel to the laser propagation direction, and T_t is the translational temperature.

3.2.6 Fluorescence yield

Due to collisions between absorbers and other molecules, energy can be transferred non-radiatively through these collisions. This energy transfer causes a quenching effect, reducing the amount of fluorescence emitted due to this alternative path to equilibrium. The term that accounts for this effect is called fluorescence yield (Φ), and is defined by the following equation:

$$\Phi = \frac{A_e}{A_e + Q_c} \tag{3.10}$$

where A_e is the Einstein A coefficient, and Q_c is the collisional quenching term. The quenching term is represented by a superposition of the quenching factors from each molecular or atomic species. The quenching effect is proportional to the total density of all species (N), the mole fraction of that species (χ), the average velocity (v), and the quenching cross section (σ). This can be represented as a sum of all involved species i:

$$Q_c = N\sqrt{\frac{8K_B T_t}{\pi m_a}}\sum_i \chi_i \sigma_i \frac{1}{\frac{m_i}{m_a+m_i}} \tag{3.11}$$

where m_a is the mass of the absorber species, and m_i is the mass of species i in the flow. Quenching cross sections σ can be experimentally determined by estimating the coefficients in the equation

shown below [Palma et al., 1999].

$$\sigma_{NO} = c_0 + c_1 e^{-c_2(T_o/T)} + c_3 e^{-c_4(T_o/T)} \tag{3.12}$$

3.2.7 Boltzmann fraction

This term represents the fraction of the ground state population that has been excited to a higher energy state due to the absorption of incident radiation [Di Rosa, 1996]. NO energy levels are primarily characterized by the rotational (J'') and vibrational (v") quantum numbers [Palma et al., 1999]. Equations 3.13 to 3.15 define the Boltzmann factor (F_b), partition function (Z_p), and the Boltzmann fraction (F_B). The Boltzmann factor defines the energy partitioned in rotational energy level J". The partition function defines the total energy of the absorber held in all energy levels. The Boltzmann fraction is the ratio of energy held in a specific energy level, to the total energy available in the absorber.

$$F_b = (2J"+1)\exp\left[-\frac{1}{K_B}\left(\frac{g(v")}{T_v} + \frac{f(J",v")}{T_r}\right)\right] \tag{3.13}$$

$$Z_p = 2\sum_{v"=0}^{7}\sum_{i=1}^{2}\sum_{J"=0.5}^{90.5}(2J"+1)\exp\left[-\frac{1}{K_B}\left(\frac{g(v")}{T_v} + \frac{f(J",v")}{T_r}\right)\right] \tag{3.14}$$

$$F_B = \frac{F_b}{Z_p} \tag{3.15}$$

The functions g and f are specific to the vibrational and rotational energy levels of NO, respectively [Palma et al., 1999; Di Rosa, 1996].

3.2.8 Saturation

The saturation term (s) represents an effect that occurs when the ground state of NO is depleted under high irradiance. This effect can particularly occur in low density conditions where the mechanisms for re-filling the depleted levels are slow (collisional energy transfer) [Palma et al., 1999].

The saturation term is dependent on laser irradiance and the NO transition parameters. A definition is given in the literature to calculate an approximate value of s [Palma et al., 1999]:

$$s = \frac{I_L(B_{12} + B_{21})}{A_e + Q_c} \tag{3.16}$$

where A_e, B_{21} and Q_c are the Einstein A coefficient, Einstein emission B_{21} coefficient, and collision quenching term, respectively.

3.2.9 Absorption

As a laser propagates through NO, laser energy is attenuated from absorption by the absorber species. Laser absorption occurs at different rates for each transition, as the absorption coefficient is dependent on the population of the ground state transition energy level. Beer's law of absorption describes the absorption characteristics of each transition, and is defined by the following equation:

$$I_L = I_o e^{-k_a(J'')l} \tag{3.17}$$

where l is the laser path length. The transition-dependent absorption coefficient k_a is defined as:

$$k_a(J'') = \frac{1}{1+s} B_{12} F_B k_o \tag{3.18}$$

where the transition-independent absorption coefficient k_o is defined as:

$$k_o = N_T G h \nu c \tag{3.19}$$

3.2.10 Camera terms

A number of other terms are included in the fluorescence equation such as the detection time of the detector/camera (t_{det}), volume probed by the laser (V_o), detection solid angle (Ω_d), and the detector efficiency of the camera being used (η). These terms do not need to be considered for the measurements in the current work, as the quantitative measurements depend on relative changes in the fluorescence signal, not absolute changes that would be affected by the camera terms.

Chapter 4

EXPERIMENTAL SETUP

This chapter outlines the experimental set-ups for the main HyMETS arc-jet study, as well as a static gas cell study used to quantify the spectral linewidth of the laser. The LIF experimental apparatus was designed and assembled by Dr. Paul Danehy and his colleagues. The author and Dr. Craig Johansen provided input on the experimental campaign including selection of the spectral ranges and spectral scan step sizes, and the design of the saturation study. The purpose of the experimental campaign was to acquire NO-PLIF imaging data that could be post-processed to provide quantitative measurements such as temperature and velocity. The arc current of the arc-jet was varied to produce flows with varying enthalpy.

4.1 Arc-jet facility

The HyMETS arc-jet facility is located at NASA Langley Research Center and is a 400kW segmented constrictor direct-current electric arc heater system, producing flow in the test section at approximately Mach 5 [Splinter et al., 2011]. The range of possible operating conditions for the facility are shown in Table 4.1. Figure 4.1 shows a photo of the facility, which consists of four major parts. First, there is the control bay where the interfaces for operating the facility are located. Adjacent to the control bay is the main test chamber, which consists of the arc generator, nozzle, test section, four optical windows for imaging and four flow-injectable probe instruments. Next to the test chamber is the diffuser, which is linked into the vacuum pump system used to keep the test section at low pressure. The arc generator consists of a copper cathode with a tungsten button emitter and 32 electrically-isolated copper segment constrictors each with a 12.7 mm bore hole, and a copper divergent ring shaped anode. Test gases are injected tangentially into the cylindrical arc generator, and an electric arc is produced axially down the center of the cylinder, attaching at

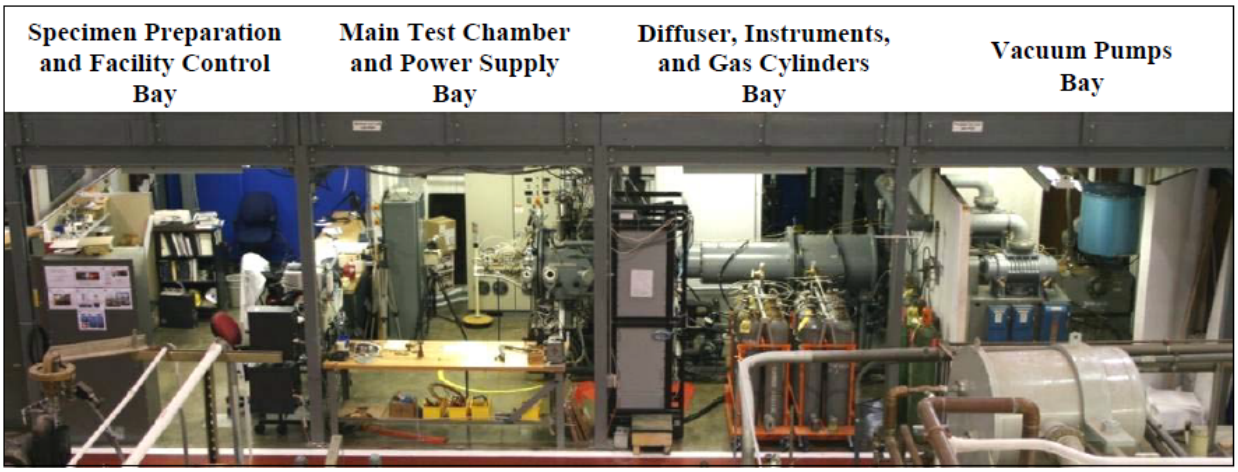

Figure 4.1: The HyMETS arc-jet facility. Reproduced from Splinter et al. [2011].

the anode and cathode. Gas injectors are located at the back, middle and nozzle locations of the arc-generator, and the flow rate can be adjusted to each injector. The tangential injection of test gases spin-stabilizes the arc in the center of the cylinder, theoretically reducing the fluctuation in arc motion away from the radial center [Splinter et al., 2011]. The electric arc ionizes the test gasses, producing a non-equilibrium plasma, which passes through the plenum and is expanded through the converging diverging nozzle (12.7 mm diameter throat, 8 degree half-angle conical nozzle) into the optically accessible test section (0.6 m diameter, 0.9 m long). The nozzle is a copper convergent-divergent nozzle designed to produce flow at approximately Mach 5 at the nozzle exit into the test section. The ionization process within the arc generator naturally produces NO, which is utilized as the tracer species for NO-PLIF measurements. The test section is vacuum pumped to maintain a low back pressure, normally less than 1000 Pa [Splinter et al., 2011]. The arc current and mass flow rate of injection gases can be varied to achieve a wide range of flow enthalpy conditions.

Multiple probes can be injected into the test section of HyMETS. A pitot tube can be used to measure the stagnation pressure, which is located on a lower injection sting. The Gardon gauge can be utilized, which can measure fully-catalytic cold-wall heat flux, and is located on the remaining lower sting. The copper slug calorimeter is used to measure fully catalytic heat flux as well, and is

Table 4.1: Operation conditions of the HyMETS arc-jet facility. Data from Splinter et al. [2011].

Variable	Value
Specimen surface temperature (K)	1530 - 2750
Specimen surface pressure (kPa)	1.3 - 8
Freestream Mach number	5.0
Freestream enthalpy (MJ/Kg)	5.3 - 26.7

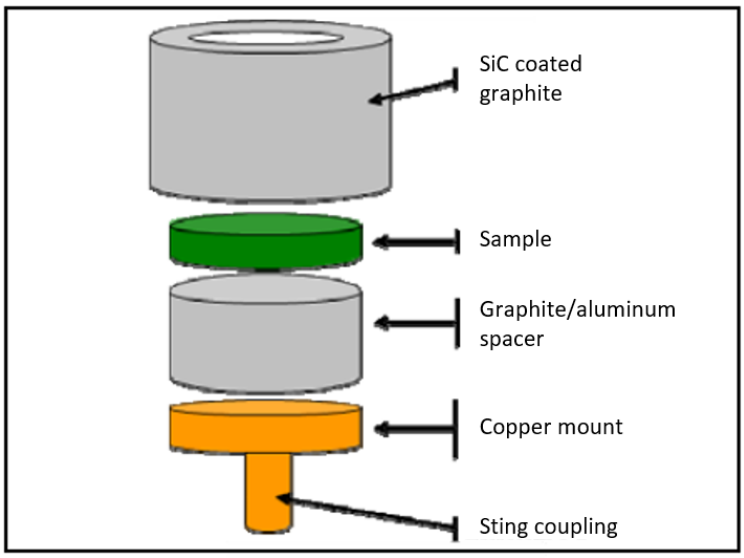

Figure 4.2: The components of the SiC probe used in the current study. Reproduced from Splinter et al. [2011].

located on an upper sting. The final sting can be interchanged between: a teflon slug calorimeter, or a silicon-carbide (SiC) probe, which measures non-catalytic heat flux and semi-catalytic heat flux, respectively. The standard dimensions for all probes (except the SiC probe) is a 33 mm diameter flat-faced cylinder with a 3.1 mm edge radius. In the current work, HyMETS was operated with a SiC test specimen. The specimen used has a recessed center (23 mm inner diameter, 33 mm outer diameter, 0.76 mm recession depth), due to the SiC specimen being comprised of an SiC disk held in place by an SiC shroud, connected to a main sting structure. Figures 4.2 and 4.3 illustrate the components of the SiC probe, while Figure 4.6 illustrates the specimen geometry in the facility. Note that in the current study, the "specimen" referred to was the SiC probe.

To calculate the bulk enthalpy of the facility while operating, an energy balance is performed

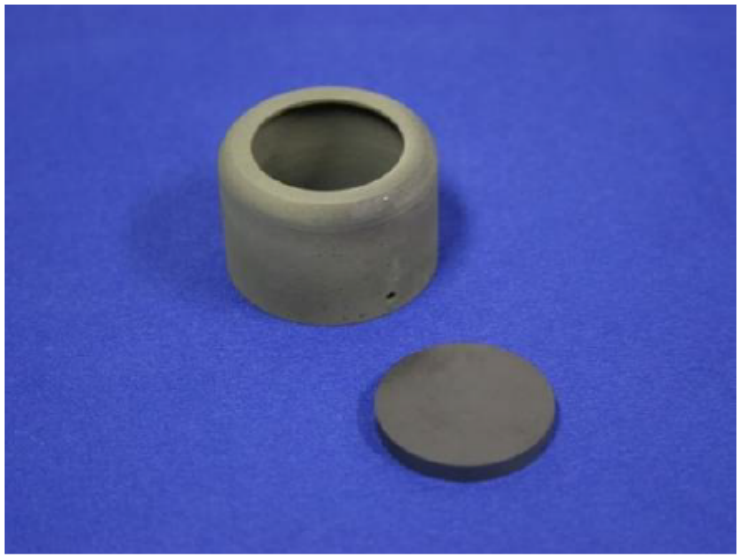

Figure 4.3: A photograph of the SiC probe. Reproduced from Splinter et al. [2011].

on the arc generator. Energy entering the system is defined as the product of the voltage and current. Energy leaving the system is defined as the product of the cooling water flow rate and the differential temperature measured from the inlet and outlet of the cooling water system. Then, the energy that remains in the generator is divided by the measured mass flow rate. This energy balance analysis results in the following equation:

$$H_o = \frac{V_v I - CWC_p \rho \Delta T_{cw}}{M_{total}} \tag{4.1}$$

where H_o is the bulk enthalpy of the flow within HyMETS, V_v is the voltage, I is the current, CW is the flow rate, C_p is the heat capacity of water, ρ is the density of water, ΔT_{CW} is the difference in the inlet and outlet temperatures for the water cooling system, and M_{total} is the mass flow rate through the nozzle into the test section. This equation is used to calculate the enthalpy of each run detailed in Table 4.2.

4.2 Laser-induced fluorescence setup

A planar ultraviolet laser (225-226 nm, approximately 0.07 nm spectral width) sheet was directed horizontally into the test section through an optical window to radiatively excite the naturally occurring NO in the test section. The laser sheet is oriented in the horizontal plane, perpendicular to the flow direction. The sheet passes through the stagnant, shear-layer and free-stream regions. The sheet path is oriented such that approximately 6 mm of the beam is blocked by the side of the specimen. The laser sheet continues past the specimen, illuminating the second shear layer and stagnant regions. An example PLIF image is shown in Figure 4.7, where each flow region is labelled. The optical path begins with a Spectra-Physics Pro 230 Nd:YAG laser producing a laser beam pulse at a wavelength of 1064 nm, a pulse width of 10 ns, and a repetition rate frequency of 10 Hz. The beam pulse is directed through a beam splitter, producing two separate beam paths. The first path is frequency tripled to 355 nm, and the second path is frequency doubled to 532 nm. The 532 nm beam pulse pumps a Sirah Cobra-Stretch dye laser to produce a 632 nm beam pulse. The 355 nm beam pulse is sum-frequency mixed with the 632 nm beam pulse in a Sirah frequency conversion unit, which produces a final beam pulse of approximately 225-226 nm. The center wavelength of the beam pulse can be tuned by adjusting the angle of a diffraction grating within the frequency conversion unit. The optical set-up produces beam pulses within the spectral range of the $A^2\Sigma^+$ - $X^2\Pi$ system of NO, where multiple transitions are optically accessible. The beam path is directed through cylindrical and spherical lenses (focal length of 5 cm and 50 cm, respectively) to form a planar laser sheet. The laser sheet path is split into two separate paths using a beam splitter. The first path directs a small fraction of the initial beam energy into a dye bath, where the laser sheet profile is monitored using a Photometrics Coolsnap camera. The second laser sheet path, containing the majority of the initial beam energy, is directed through the facility optical window into the HyMETS test section. The laser sheet pulse excites the NO present in the flow, radiatively exciting the molecule to a higher energy state. The subsequent fluorescence cascade creates a long wavelength emission. The emitted radiation is captured using a combination of a

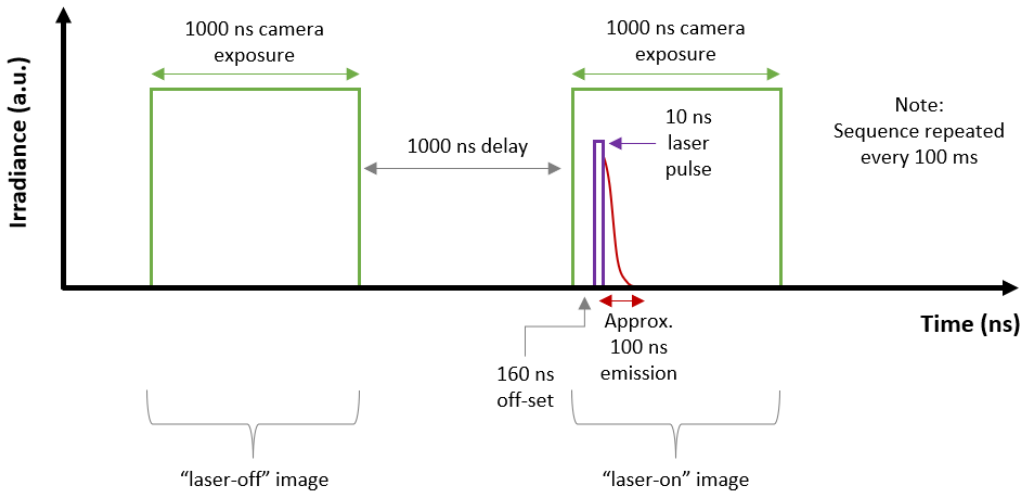

Figure 4.4: Camera and laser timing used in the current study.

ultraviolet filter (either (1) LayerTec GmbH longpass filter or (2) UG5 bandstop filter) and a PCO DICAM C1 intensified CMOS high-speed camera. The optical filter blocks the laser frequency radiation, allowing only fluorescence emission and long-wavelength flow luminosity to reach the camera sensor. To remove the natural luminosity from the image that passes through the filter, two images are acquired during each laser pulse cycle: the first is to capture the fluorescence radiation with background natural luminosity, and the second is captured off-pulse to record the natural luminosity of the flow. The natural luminosity is removed from the fluorescence image by subtracting the first image from the second image for each laser pulse cycle. To further reduce the impact of the natural luminosity, the exposure time is minimized (1000 ns) for each image captured. An off-set of 160 ns is included to ensure the camera is capturing the complete fluorescence lifetime emission from NO. The timing of the laser and camera is shown in Figure 4.4. The laser can either be scanned spectrally across the frequency domain to excite multiple rotational transitions in NO in a single run, or be spectrally stationary, therefore only exciting a single transition at a fixed wavelength. The NO-PLIF set-up is detailed in Figures 4.5 and 4.6.

Table 4.2: Run conditions.

Run	Bulk enthalpy (MJ/kg)	Arc current (A)	Mass flow rate (slpm)	Laser energy (mJ/pulse)	Scan step size (nm)	Scan range
G1	-	-	-	0.5	0.00002	C
R1	5.7	100	402	variable	-	Fixed
R2	5.7	100	402	3.0	0.00013	A
R3	5.7	100	402	0.5	0.00013	A
R4	5.7	100	402	0.6	0.00004	B
R5	6.9	125	402	1.0	0.00004	B
R6	8.4	150	402	0.7	0.00004	B
R7	5.7	100	402	0.6	-	Fixed

4.3 Experimental campaign

The full experimental campaign consisted of 26 experiments in the HyMETS arc-jet facility at varying enthalpy conditions, and three gas cell experiments performed in a small sealed vessel containing NO placed into the laser path within the test chamber while the facility was not running. Significant effort was invested in reducing the data set to seven runs for quantitative analysis, and a single gas cell experiment. Reasons for removal of data included oversaturation of the camera, missing data from the sheet profiling camera, extreme fluctuations in the data at high enthalpy conditions, laser energies that produced fluorescence data unusable for quantitative analysis due to low SNR or extreme saturation effects, and data acquisition errors. Only the highest spectral resolution gas cell experiment was retained, as this was used to determine the exact linewidth of the laser. Table 4.2 contains the arc current, mass flow rate, and bulk enthalpy values for each operating condition.

The enthalpy conditions chosen in the current study were in a similar range of previous CFD studies examining the HyMETS facility [Inman et al., 2013; Brune et al., 2019]. For all tests, the gas composition was kept constant at 75% N_2, 20% O_2, and 5% Ar, which closely resembles air. Three spectral ranges are scanned across in the current study (see Tables 4.2, 4.3 and Figure 4.8). A number of overlapped transitions are defined as “transition groups”, and are detailed in Table 4.3. Note that the Q1 band head region was removed, as it consists of many overlapping transitions

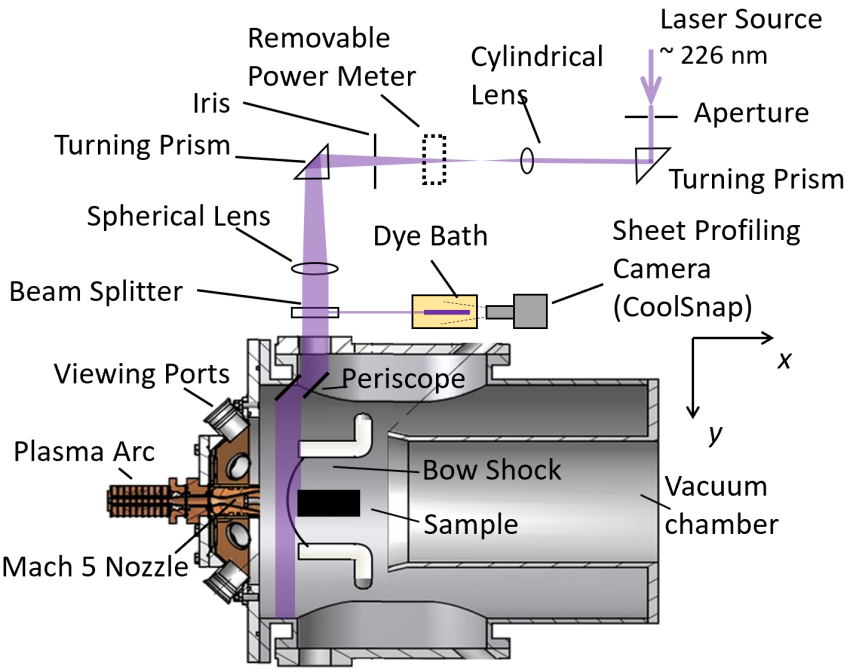

Figure 4.5: Top view of the HyMETS arc-jet facility.

that are not useful for the quantitative measurements in this work. These runs were completed at a finer spectral resolution than the minimum spectral resolution to produce accurate temperature results, as previously suggested in the literature [McDougall et al., 2020a]. Two runs (R1 and R7) used a fixed wavelength (tuned to transition group #5) for saturation analysis and unsteadiness minimization, respectively.

4.4 Gas cell

The gas cell experiment was conducted using a small cubic gas cell approximately 30 cm wide in each dimension. The cell contained 5% NO and 95% nitrogen, by volume. The cell was placed within the HyMETS test section (while the facility was not running) to ensure the path length of the laser is identical to the main experiment. Optical windows on either side of the cell were oriented such that the laser sheet passes through one window, propagates through the gas cell, and exits through the second optical window. A third optical window on the bottom face of the cell was oriented toward the lower optical window mounted on the bottom of the HyMETS facility, such

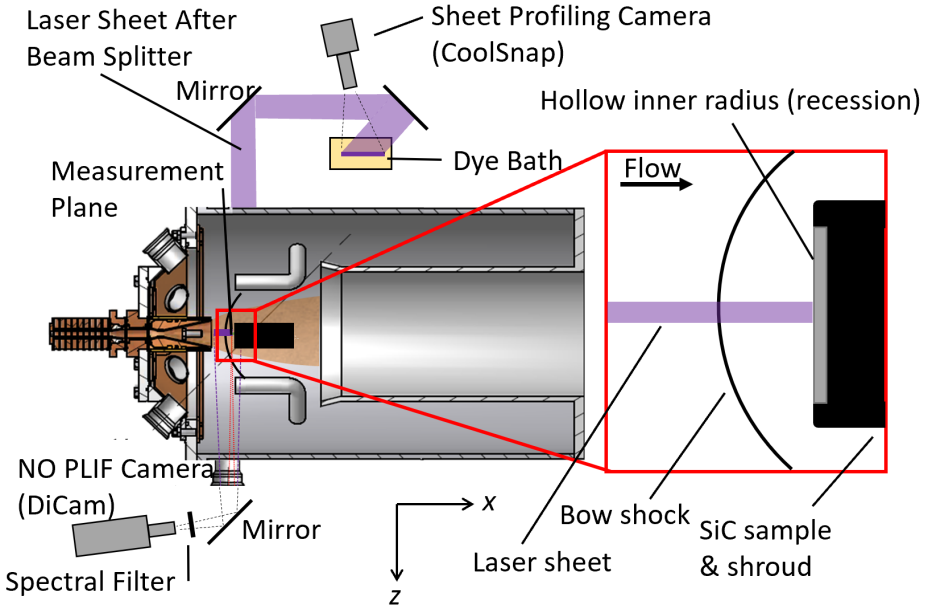

Figure 4.6: Side view of the HyMETS arc-jet facility.

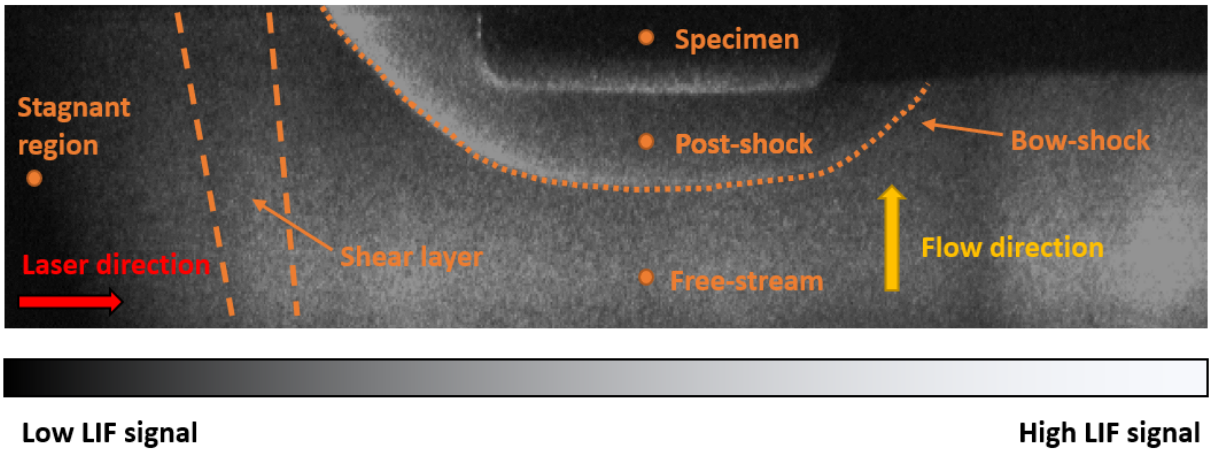

Figure 4.7: Example PLIF image with major flow structures labelled.

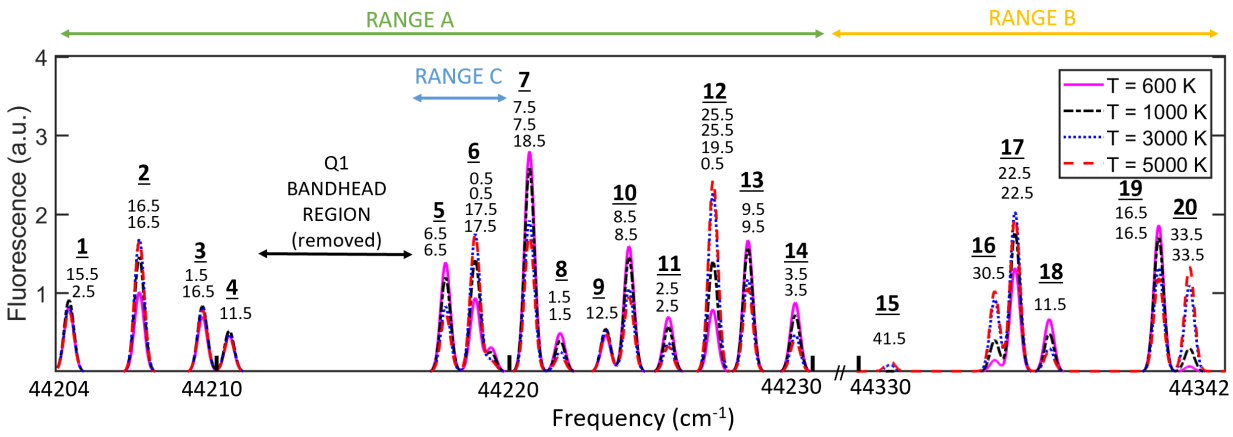

Figure 4.8: Scan range A , B and C overlayed onto generated NO spectra with J″ values labelled.

that the laser sheet could be viewed perpendicularly. The gas cell data was used to determine the spectral linewidth of the laser, which is then used in the translational temperature measurement. The gas cell was kept at room temperature (295 K) during the duration of the tests. The laser was tuned over spectral range C, as shown in Figure 4.8.

Table 4.3: Transitions excited in the current study. Data obtained from Reisel et al. [1992].

Transition	Range	J''	Einstein B_{12} absorption coefficient	Centre wavenumber (air) (cm^{-1})	Transition group index (k)
P_1	A	15.5	135.955	44205.138	1
P_1	A	2.5	86.669	44205.132	1
Q_2	A	16.5	278.194	44207.480	2
${}^{Q}R_{12}$	A	16.5	48.501	44207.454	2
P_1	A	16.5	138.205	44209.568	3
P_1	A	1.5	70.371	44209.555	3
R_2	A	11.5	115.800	44210.484	4
Q_1	A/C	6.5	232.560	44217.690	5
${}^{Q}P_{21}$	A/C	6.5	70.004	44217.672	5
R_1	A/C	0.5	129.551	44219.040	6
${}^{R}Q_{21}$	A/C	0.5	259.101	44219.061	6
Q_2	A/C	17.5	282.165	44219.560	6
${}^{Q}R_{12}$	A/C	17.5	46.954	44219.563	6
P_1	A/C	18.5	142.429	44220.467	7
Q_1	A/C	7.5	237.548	44220.512	7
${}^{Q}P_{21}$	A/C	7.5	68.417	44220.520	7
R_1	A	1.5	119.843	44221.444	8
${}^{R}Q_{21}$	A	1.5	198.432	44221.485	8
R_2	A	12.5	118.996	44223.037	9
Q_1	A	8.5	242.497	44223.804	10
${}^{Q}P_{21}$	A	8.5	66.650	44223.821	10
R_1	A	2.5	117.214	44225.129	11
${}^{R}Q_{21}$	A	2.5	184.751	44225.131	11
${}^{S}R_{21}$	A	0.5	129.527	44226.565	12
P_1	A	19.5	144.410	44226.588	12
P_2	A	25.5	160.930	44226.591	12
${}^{P}Q_{12}$	A	25.5	78.685	44226.594	12
Q_1	A	9.5	247.375	44227.778	13
${}^{Q}P_{21}$	A	9.5	64.779	44227.790	13
R_1	A	3.5	116.930	44229.358	14
${}^{R}Q_{21}$	A	3.5	176.466	44229.361	14
${}^{O}P_{12}$	B	41.5	24.243	44331.343	15
P_1	B	30.5	161.248	44334.854	16
Q_1	B	22.5	299.799	44335.569	17
${}^{Q}P_{21}$	B	22.5	41.341	44335.573	17
${}^{S}R_{21}$	B	11.5	70.585	44336.657	18
Q_1	B	16.5	139.899	44334.034	19
${}^{Q}P_{21}$	B	16.5	109.887	44334.041	19
P_2	B	33.5	168.811	44341.355	20
${}^{P}Q_{12}$	B	33.5	58.880	44341.374	20

Chapter 5

PREPROCESSING METHODOLOGY

This chapter describes the procedure used to prepare NO-PLIF experimental data for quantitative variable measurements. The chapter begins with a brief overview of the analysis procedure for clarity. The preprocessing procedure included image processing steps that aim to prepare the images for analysis, as well as reduce sources of error and uncertainty. Also included in this chapter is a number of initial studies that are completed prior to the quantitative measurements.

5.1 Methodology overview

This brief section provides an overview of the analysis that will be applied to the NO-PLIF data acquired in the HyMETS arc-jet facility. This overview is provided for clarity due to the inter-dependence of many preprocessing and quantitative measurement steps completed in this work. Figure 5.1 presents a high-level overview of the analysis procedure.

The analysis completed in the current work can be grouped into two categories: preprocessing and quantitative measurements, which each form their own chapters 5 and 6. Chapter 5, the current chapter, includes image processing steps and three initial studies. The results of these studies are used in the quantitative measurements, as shown in Figure 5.1. Chapter 6 describes how the data is prepared for each quantitative measurement, and how the measurement is made.

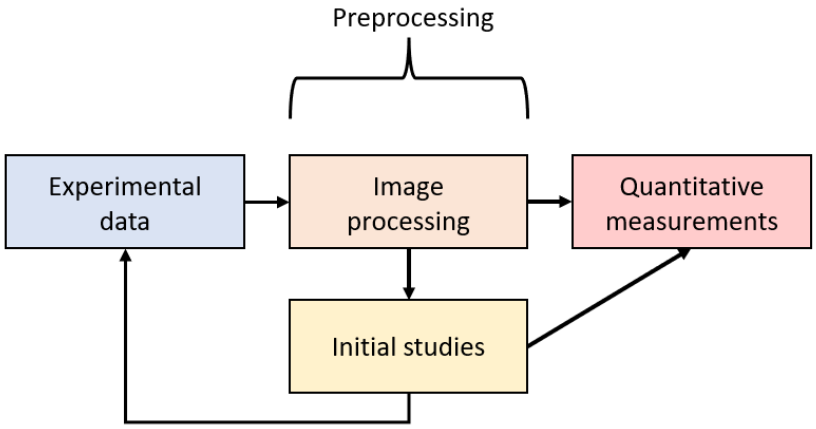

Figure 5.1: Analysis procedure chart.

5.2 Image processing

This section presents the image processing steps required for all NO-PLIF and laser-profiling images captured during the experimental campaign. These processes correct for various effects to produce images that provide accurate fluorescence information. The NO-PLIF and sheet profiling camera images were processed to remove the following sources of error or uncertainty: background natural luminosity, image distortion, orientation corrections, shot-to-shot laser fluctuations, flow unsteadiness, and laser absorption. Laser and emission refraction through the shock-wave was investigated, but was determined to be insignificant for the flow conditions in the current experiment [Panda and Adamovsky, 1995]. The following subsections describe each image processing step in detail.

5.2.1 Luminosity subtraction

As described in Chapter 4, the NO-PLIF camera captures two consecutive images, followed by a large delay. The first image (laser-off) is captured while the laser is off between pulses, while the second image (laser-on) is captured as the laser pulse is incident on the flow in the test section. To correct for natural luminescence visible in the shock layer in front of the blunt body specimen, the

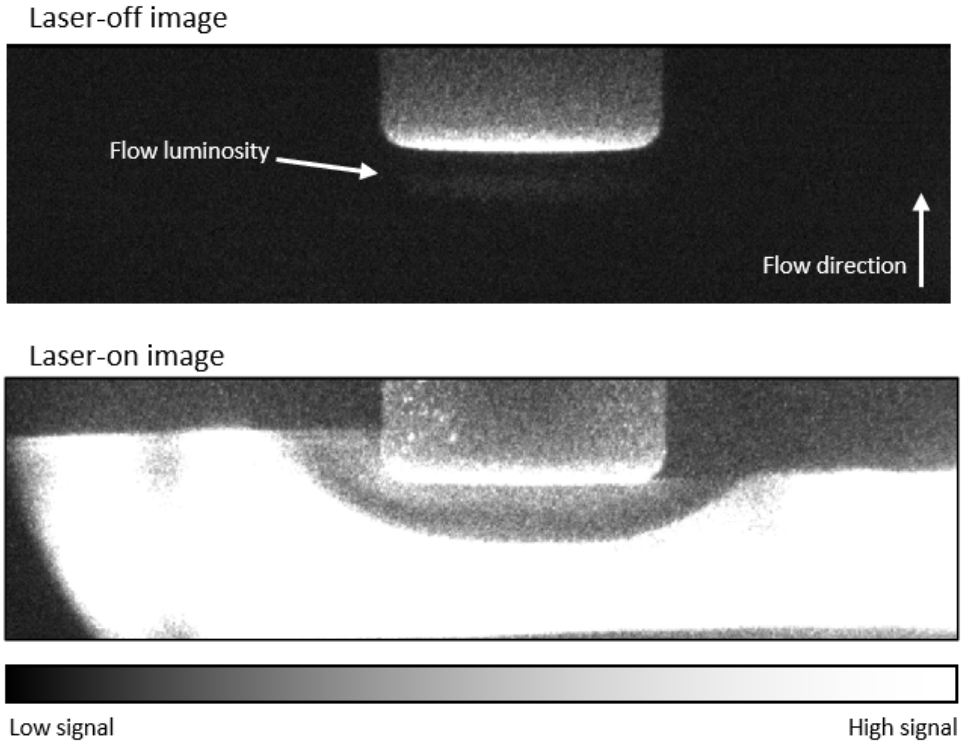

Figure 5.2: Flow luminosity example.

laser-off image is subtracted from the laser-on image. This analysis step is completed for every pair of images in the image stack. The pair of images have a temporal separation of 1000 nanoseconds, freezing the flow, and preventing flow perturbations from affecting the subtraction. Additionally, since the images are acquired with the same camera and field of view (FOV), the images can be perfectly overlayed and subtracted without any alignment steps. An example of the paired images is shown in Figure 5.2.

5.2.2 De-warping

Image distortion from optical effects such as perspective and lens distortion is corrected by using a dot card de-warping technique. This method has been used in previous studies to correct for distortion [Inman et al., 2010]. Prior to the experiment, a dot card is inserted in-plane with the laser sheet into the imaging region. An image is captured while illuminating the dot card in the frame, with the dots clearly visible to the camera. This image is saved, and will be referred to

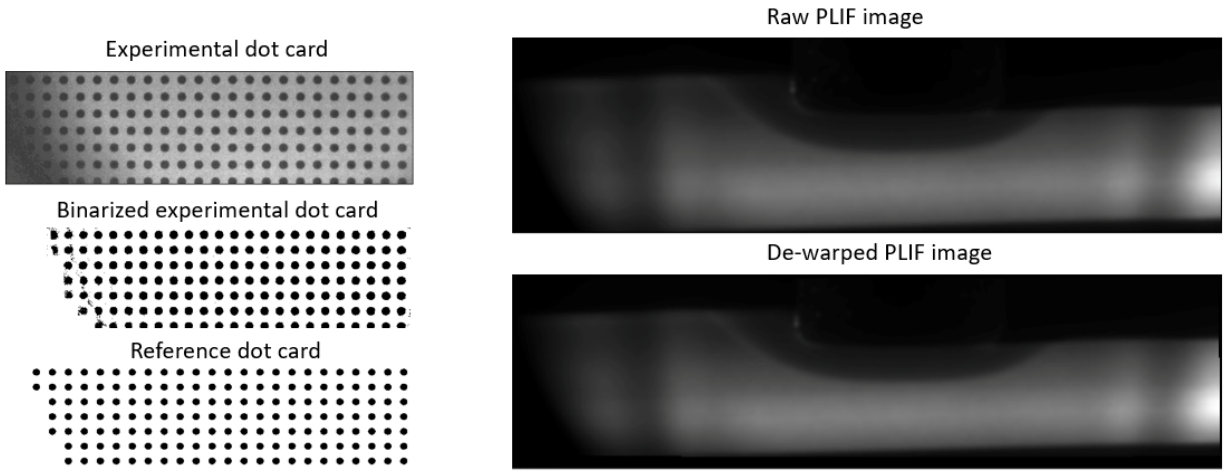

Figure 5.3: The dot card de-warping process.

as the "experimental dot card". The experimental dot card is first binarized, then undergoes a process called image registration, where each dot is matched with the original image of the dot card, known as the "reference dot card". An affine transform is fitted to the experimental dot card (translation, rotation, scaling, and shear mapping), such that the experimental dots line up exactly with the corresponding dots on the reference dot card. The transform that is fitted to the experimental dot card is saved, and applied to all experimental images. This process allows for the correction of distortion in the experimental image that can affect the spatially-resolved quantitative measurements. An example of the de-warping process is illustrated in Figure 5.3.

5.2.3 Rotation correction

Both the laser profiling camera and the NO-PLIF camera are not perfectly oriented to the laser sheet, such that the laser is at an angle in the acquired images. Subsequent processing steps (i.e. subsection 5.2.4) require the laser sheet in the NO-PLIF images and the laser profile in the sheet profiling images to be exactly parallel to the pixel grid of the image. The process to correct this requires a comb-like object with a pattern of openings and blockings on it. This object is inserted into the beam path upstream of the beam splitter, such that a pattern emerges in the beam downstream that can be viewed in both the laser profiling dye bath and in the test section of the facility.

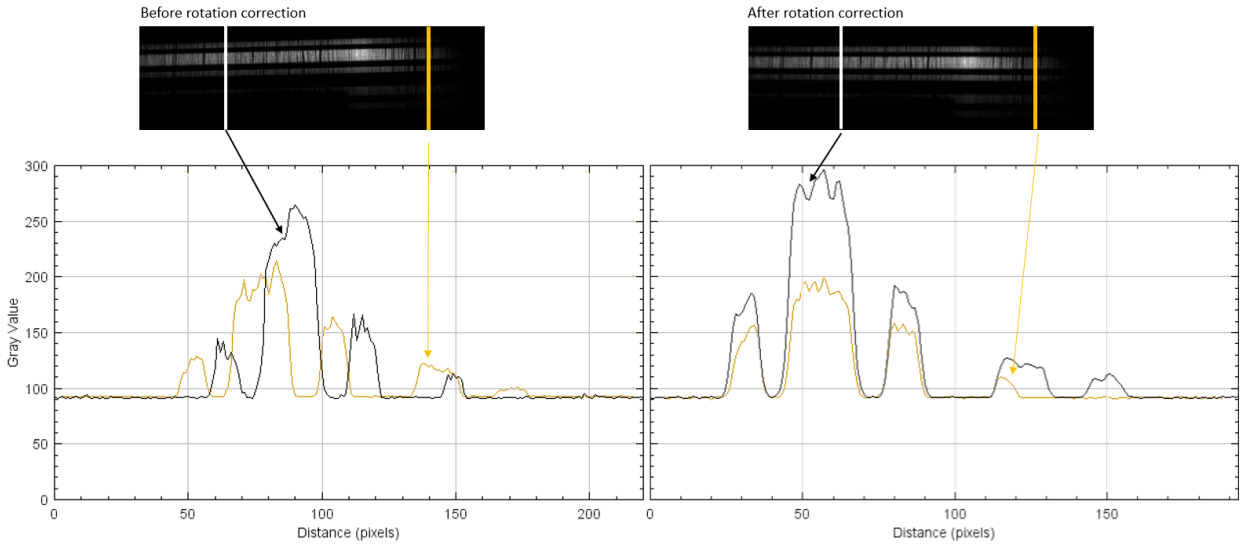

Figure 5.4: The rotation correction process for NO-PLIF images.

The pattern produces straight lines on the image that correspond to the laser path orientation, and are used to manually correct each image stack. This operation is completed in the ImageJ program, using the rotation and plotting utilities. The images are manually corrected until the half-maximum of the edge of the comb pattern lines up across all locations of the image. The rotation correction process is depicted in Figure 5.4.

5.2.4 Scaling alignment

The scaling alignment step maps the laser profile to the NO-PLIF image such that each location on the width of the image has an associated laser thickness profile. The comb object is also required for this analysis, as the comb pattern on the laser profile image is lined up to the comb pattern on the NO-PLIF camera image. This step is done manually to align the images, then the transformation is applied to all images in the laser profile image stack. Figure 5.5 details the major steps of this procedure.

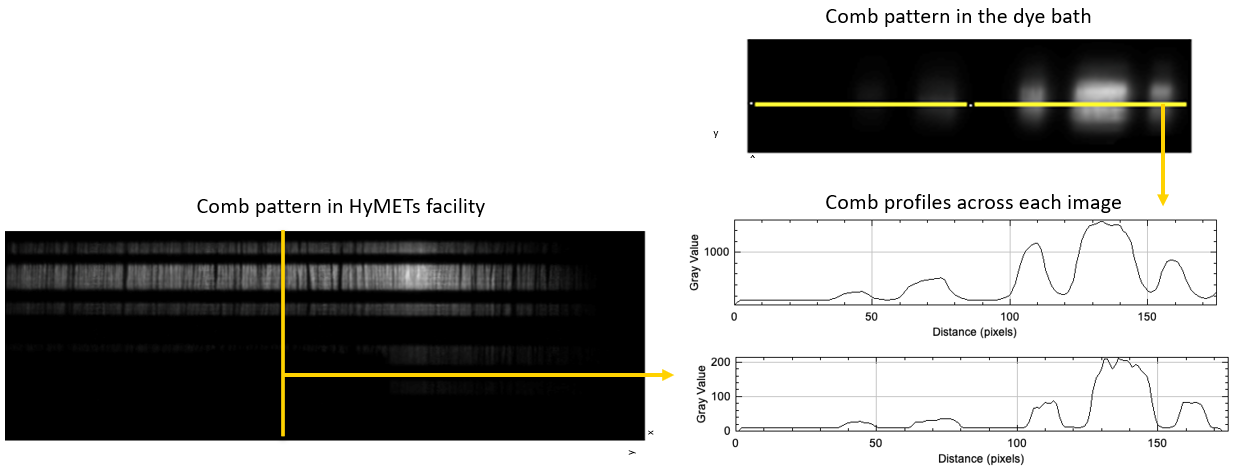

Figure 5.5: The scaling alignment process.

5.2.5 Pulse energy correction

Shot-to-shot laser fluctuations are corrected by tracking the relative laser energy through the laser profiling camera viewing the dye bath, then normalizing the NO-PLIF image by the laser energy per pulse. On average, the laser energy fluctuates approximately 8% pulse-to-pulse, as shown in Figure 5.6. The laser energy is calculated by averaging the values across the laser thickness between the full-width half-maximum, which is labelled the "core" of the laser in Figure 5.7. This calculation produces a vector of laser energies across the length of the run. The vector is normalized by dividing by the maximum laser value in the vector. The PLIF images are then divided by the vector element corresponding to that time point during the run, therefore normalizing the image for pulse-to-pulse energy differences. This correction reduces the noise in the spectral data to achieve higher accuracy measurements.

5.2.6 Gaussian filtering

Arc-jet facilities produce unsteady flow into the test section, leading to fluctuations in flow properties. These fluctuations are observed in the NO-PLIF images as well. A 2D Gaussian moving average filter (symmetric kernel size of 3) is used to reduce spatial noise in the data while not blurring important flow regions such as the shear layers and bow shock.

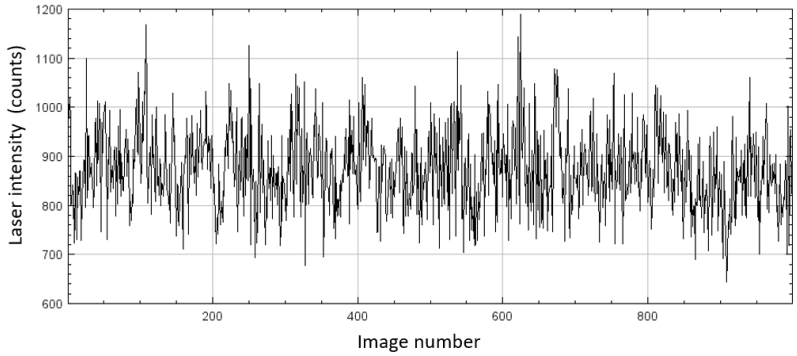

Figure 5.6: Fluctuations in laser energy over run R2 as captured by the sheet profiling camera.

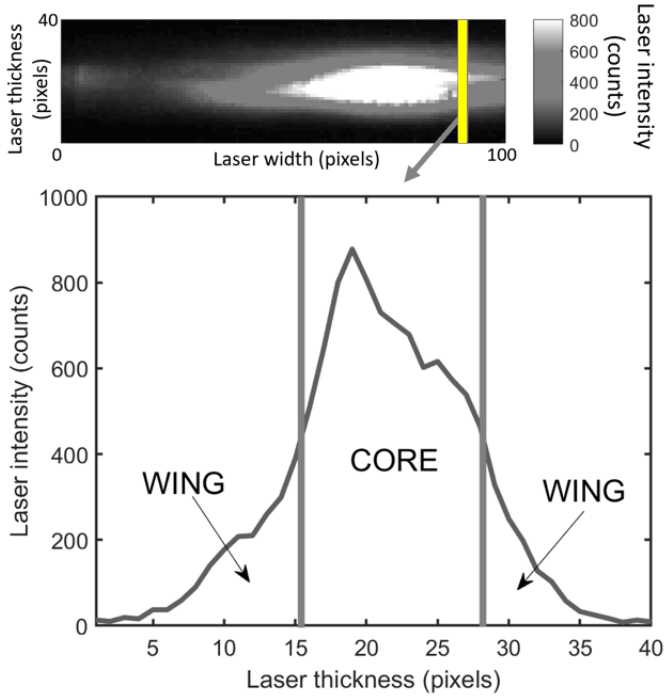

Figure 5.7: Laser profiling camera image for Run R1 with the laser intensity plotted at one location. Core and wing regions are identified on the profile.

5.2.7 Field-of-view cropping

Laser absorption occurs in the flow as the laser propagates across the field of view of the NO-PLIF camera. The beam is absorbed as it traverses the test section in a way that is dependent on the spectral location of lines, the strength of the absorption lines, and how the laser profile has been affected by absorption earlier in the line path. Therefore, to minimize the effects of absorption, the NO-PLIF images are cropped at the centerline such that only the side of the image is kept that is nearest to the optical window. This way, the data that is most distorted by absorption is removed and only the near-side is considered in the quantitative analysis. Prior studies in the literature have corrected for this effect using more complex techniques, however they are incompatible with the current data set, as discussed later in Chapter 8. Laser absorption is unlikely to occur in the stagnant region, and has not been considered in previous studies, and is therefore not accounted for in the current work.

5.3 Initial studies

This section describes the methodology used for three initial studies that require completion prior to completing the main quantitative measurements. Overall, the purpose of these studies is to reduce uncertainty in the NO-PLIF data, or remove/correct for systematic errors that could affect the quantitative measurements. These studies include minimizing unsteadiness in the facility by determining the optimal arc-jet gas injection configuration, quantifying laser saturation occurring in the flow for use in the rotational temperature measurement, and measuring the spectral linewidth of the laser for use in the translational temperature measurement. The results of these studies are also presented in this section, as they are needed for context in subsequent chapters.

5.3.1 Unsteadiness minimization study

Due to large scale unsteadiness identified in the flow from previous PLIF studies undertaken at the HyMETS facility [Inman et al., 2013], an effort was made in the current work to reduce unsteadi-

ness by changing the gas injection parameters of the arc generator. The facility has 3 injection locations, denoted “back”, “middle” and “nozzle” across the length of the cylindrical arc generator. During a single experimental run (R7), the gas injection was varied between the “middle” and “nozzle” injection locations, while keeping “back” at a constant 40% injection fraction. The laser was tuned to the center of transition group #5 for the duration of the run. Six test configurations varied the nozzle injection from 5% to 50%, and approximately 10 seconds of data was acquired for each configuration. If nozzle injection was increased, the “middle” injection point was decreased proportionally. The overall flow rate was kept constant throughout the experimental run. NO-PLIF data was captured to quantify unsteadiness through fluctuations in the LIF signal. Note that at the beginning of the experimental campaign, this study was completed qualitatively using a trial run of the facility to determine the ideal 20% nozzle injection configuration. After the other experimental data was gathered (R1-R6), a run dedicated to the current quantitative analysis (R7) was acquired. Therefore, the exact unsteadiness measurements presented in this section were not known at the time of the experimental campaign, but qualitative observations were known from the trial run. Therefore, the results presented in this section were produced after the experimental campaign was acquired.

The results from the unsteadiness minimization study are presented in three different ways in Figures 5.8 and 5.9. Firstly, the raw temporal data is presented which shows the large difference in unsteadiness between the 5% and 40% nozzle injection data in Figure 5.8a. Secondly, the standard deviation of the fluorescence in a 10x10 pixel region at the center of the free-stream (centerline, x = 12 mm) is presented for each nozzle injection configuration in Figure 5.8b. Finally, a pixel-by-pixel standard deviation map is shown for each injection configuration across the free-stream and shear-layer regions of the flow in Figure 5.9.

From the information provided in Figure 5.8, nozzle injection greater than 10% greatly reduces unsteadiness in the flow. There was approximately a 40% reduction in free-stream fluctuations between the 5% and 15% nozzle injection configurations. Based on qualitative observations from

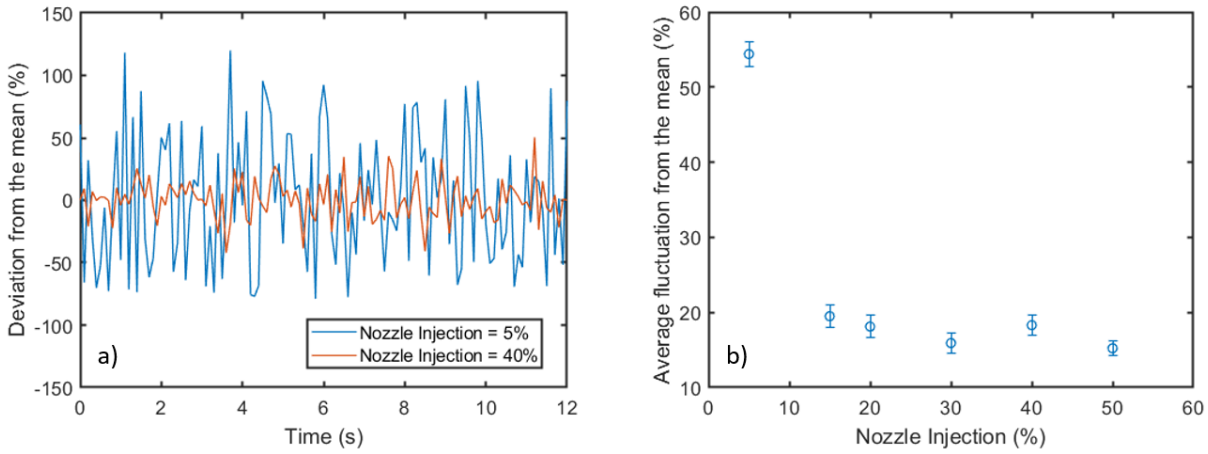

Figure 5.8: Unsteadiness minimization results: a) an example of temporal fluctuations in the free-stream at two different nozzle injection configurations, b) the temporally-averaged fluctuation from the mean at six different injection configurations.

the trial run that generally reflect these quantitative results, all runs (R1-R6) were acquired with 20% nozzle injection (40% back injection, and 40% middle injection). Figure 5.9 indicates that unsteadiness decreases most significantly in the free-stream core flow when compared to reductions in the shear-layer. There were no flow regions within the FOV that increased in unsteadiness with increased nozzle injection. Run R7 was completed without the specimen inserted into the flow, therefore the post-shock region was not investigated.

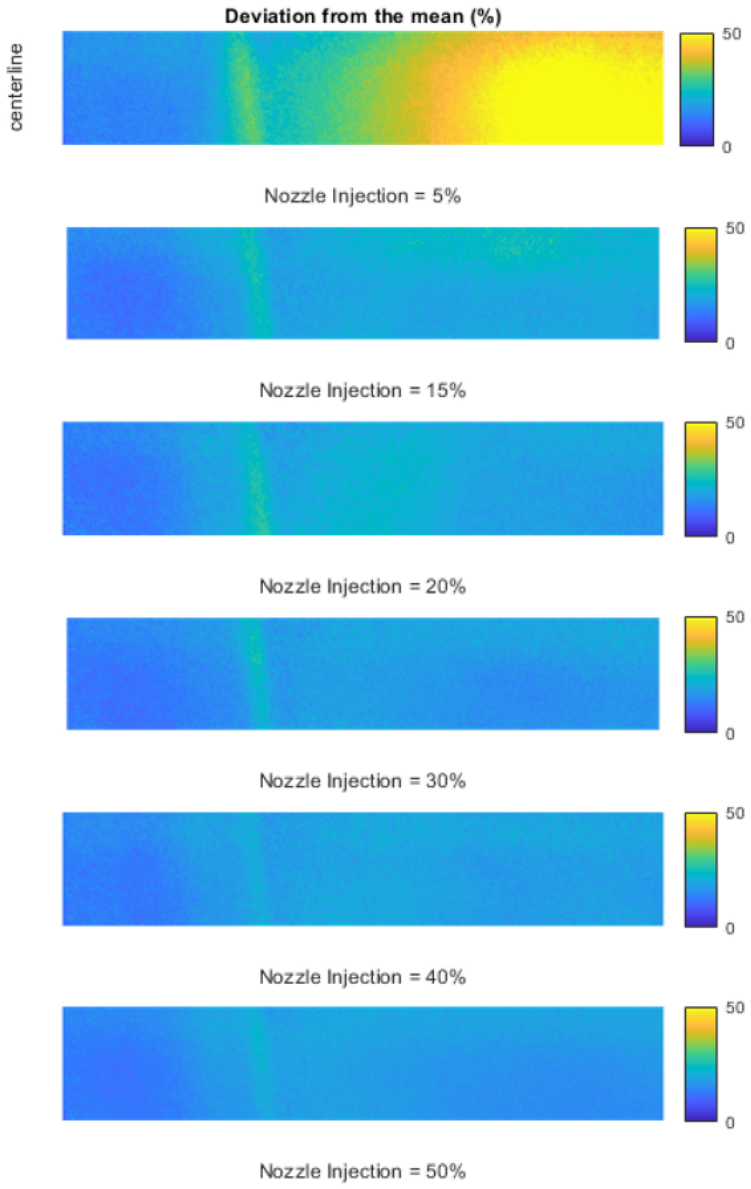

Figure 5.9: Spatially-resolved measurement of deviation from the mean shown across the laser-side of the imaging region.

This initial study has shown that increasing nozzle injection has a stabilizing effect on the flow in the test section of the facility. This result is possibly due to the stabilization of the arc within the arc generator from a more optimal gas injection configuration. As mentioned in Chapter 4, tangential injection in the HyMETS facility should theoretically spin-stabilize the arc in the center of the arc generator cylinder [Splinter et al., 2011]. In prior studies, the injection configuration was 40% (back), 55% (middle) and 5% (nozzle), compared to the current configuration of 40% (back), 40% (middle) and 20% (nozzle) [Inman et al., 2013]. By adjusting the injection configuration to be more uniform across the injection ports, the arc may be more stable in the generator, leading to less flow instability propagating into the facility test section. By reducing the unsteadiness in the free-stream through optimizing the injection configuration, less uncertainty will propagate into the quantitative measurements in the current work.

5.3.2 Saturation study

Transition saturation can introduce a significant systematic error into the rotational thermometry measurement. Therefore, a saturation experiment (R1) was undertaken to determine the saturation point, I_{SAT}, and ensure the laser energy was tuned below the saturation point for most of the experimental campaign. In this way, large systematic errors introduced by saturation were minimized in the experimental runs used for quantitative measurements. Note that this process does not fully eliminate the saturation effect from the data, therefore the measured saturation term is included in the model for the rotational temperature measurement. The analytical equation for the saturation term (s) is described in Chapter 3. This equation needs to be calibrated using a separate saturation experiment, as noted in the literature [Palma et al., 1999]. A saturation experiment consists of tuning the laser sheet to a specific transition and varying the laser sheet energy. The transition pair used was the overlapped ${}^{Q}Q_{11}(6.5)$ and ${}^{Q}P_{21}(6.5)$ transitions. The fluorescence signal is plotted against the laser energy to determine the saturation point, where the relationship between laser energy and fluorescence becomes non-linear. The experimental data is fit with the saturation equation, leaving I_{SAT} as a free-parameter.

Additional complexity was added to the method outlined by Palma et al. [1999] to capture the saturation effect. Due to laser energy non-uniformities across the laser thickness, the NO in the laser path will saturate to different levels in different areas in the flow. Since the camera is oriented perpendicular to the laser sheet, the resulting LIF signal is line-integrated across the thickness of the laser sheet, resulting in a signal consisting of saturated and unsaturated LIF emissions. For the saturation study, the laser energy is measured as an average across the full-width half-maximum of the laser. This measurement is used as an estimate of the bulk laser energy at each laser width position. The fluorescence is measured in the free-stream region of the flow between the shear layers, and is completed on a pixel-by-pixel basis to produce an array of I_{SAT} values. This method is possible due to the mapping of the laser profiling camera to the NO-PLIF images presented earlier in this chapter. The mean and standard deviation of the array is taken to determine the final I_{SAT} value used in the saturation modelling, and the associated uncertainty, respectively. The equation fit to the experimental fluorescence data produced by the transitions pair at each pixel is given by:

$$S_f = A\left[\frac{B_{12(1)}}{1+\frac{I_L}{I_{SAT_1}}}+\frac{B_{12(2)}}{1+\frac{I_L}{I_{SAT_2}}}\right] \tag{5.1}$$

where A is a free scaling constant, S_f is the experimental fluorescence signal, and I_{SAT_1} and I_{SAT_2} is the saturation point of the first and second overlapped transitions respectively. The Einstein B absorption coefficients are included to weight the relative strength of each overlapped line. The relationship between the first and second saturation points is known and is given by the following equation:

$$I_{SAT_2} = (3.325)I_{SAT_1} \tag{5.2}$$

where 3.325 is the conversion between the two transitions theoretical saturation values, obtained from the analytical equation presented in Chapter 3. Therefore, the free-parameters fit in Equation 5.1 are A (a scaling constant) and I_{SAT_1}. Note that since the saturation term s is a ratio of the laser

energy to the saturation value, both of these values can be left as signal intensity values from the camera, as conversion to radiative flux units is unnecessary. The saturation term s for a specific transition is determined by taking the ratio of the laser energy to the transition-specific fitted I_{SAT} value, which can be calculated using Equation 5.1.

The results of the saturation study are detailed in Figure 5.10. Saturation curves are presented at 3 points in the free-stream, labelled P1(x = 12 mm, y = 0 mm), P2(x = 11 mm, y = 1 mm), and P3(x = 10 mm, y = 2 mm). The saturation analysis was completed on every location within the free-stream region, excluding the shear layer, and averaged to produce an I_{SAT} value of 255 $\pm$ 45 counts on the laser profiling camera, which is labelled on Figure 5.10. This I_{SAT} value is specific to the ${}^{Q}Q_{11}(6.5)$ transition, but can be converted to all other transition I_{SAT} values using the saturation term definition from Equation 5.1. The laser energy was tuned below the saturation point for all transitions for R3 - R6. A saturated run (R2) was retained to compare thermometry results against the unsaturated runs, to determine how well the saturation modelling would correct the rotational temperature measurement. The saturation value is not dependent on temperature or pressure, due to the low density of the flow minimizing the effect of collisional quenching [Palma et al., 1999].

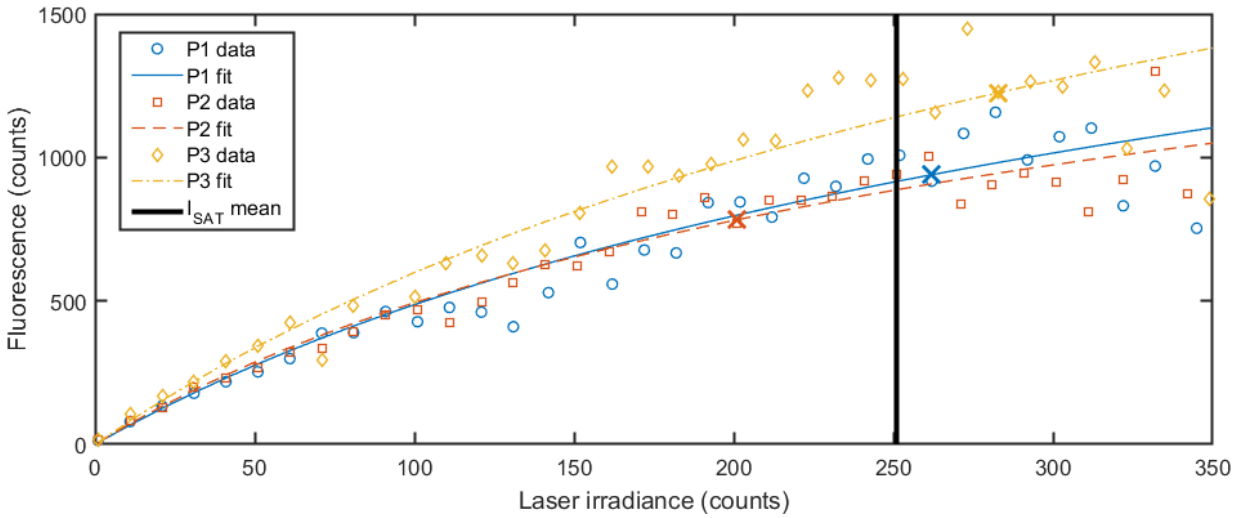

Figure 5.10: Saturation curves generated from R1 at three spatial locations within the core flow. "X" symbols indicate the individual point measured I_{SAT} values. Data plotted represents every tenth data point, however the full data set was used for the fitting procedure.

Figure 5.10 indicates the saturation value calculated at various locations across the free-stream are fairly consistent, and do not skew higher/lower based on the spatial location of the measurement. This observation adds significant confidence to the saturation study results, as the laser energy is variable across each spatial location. Laser absorption could also systematically affect the saturation measurement from NO absorption across the core free-stream flow. However, due to the consistency of the saturation measurement across these multiple spatial locations, and the absence of a systematic shift in the results, it is likely the current methodology is capturing the saturation effect accurately.

5.3.3 Gas cell study

The gas cell run (G1) was used in the current study to measure the spectral linewidth of the laser, which is needed for the translational temperature measurement. A description of the gas cell experimental set-up is provided in Chapter 4. A separate spectral range (spectral range C) was used for this study to have greater spectral resolution. To measure the laser linewidth, other broadening sources need to be quantified. Since the gas cell is kept at low pressure, collisional broadening is negligible. Doppler broadening, due to the thermal motion of the gas, is calculated using the room temperature (295 K) combined with theory presented in Chapter 3. The total absorption linewidth of the $J'' = 6.5$ transition was measured by fitting a Gaussian function to the LIF signal. The Doppler broadening term is then subtracted in quadrature from the total absorption linewidth, which produces the laser linewidth. The laser linewidth was determined to be 0.097 ± 0.008 cm^{-1}. This measurement is slightly broader than the specifications for the laser (0.07 nm). Uncertainty in the linewidth is provided by uncertainty in the fit parameter.

Chapter 6

QUANTITATIVE MEASUREMENT METHODOLOGY

This chapter presents methodologies that are used in the current work to measure quantitative variables from NO-PLIF data acquired. Each measurement methodology depends on a non-linear least-squares (NLLS) fitting process, where Gaussian function(s) is fitted to experimental LIF spectra, leaving the targeted measurement as a free parameter in the fit. Each measurement technique was developed and implemented by the author, but is based upon previous work in the literature [Palma et al., 1999]. Each Gaussian-based fitting function is based upon the fluorescence equation terms presented in Chapter 3. Note that all "*W*" variables and subscripts indicate a variable that is included as a free parameter, but is not utilized in the measurement.

6.1 Radial velocity

To measure the radial velocity of the flow, the velocity dependence of the Doppler shift term in the fluorescence equation is utilized. If the absorber gas, NO, has a velocity either parallel or anti-parallel to the laser sheet propagation direction, the line center will shift. From this shift, the velocity in that plane can be calculated. In the current work, the laser propagates perpendicular to the flow direction, therefore the radial velocity component can be measured. Figure 6.1 shows the simulated effect at different areas of the arc-jet using a generated spectral line.

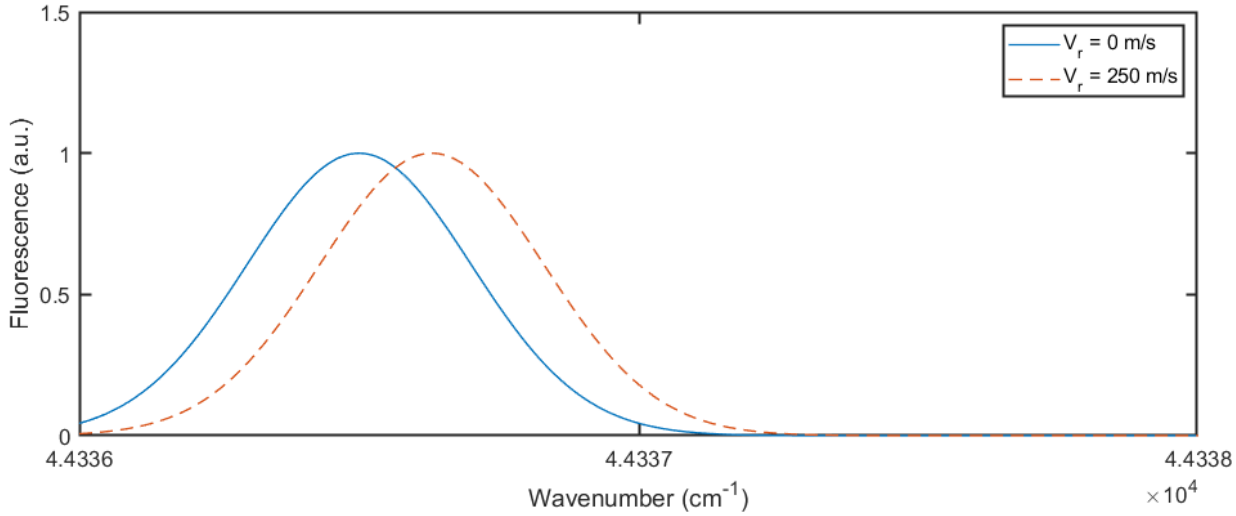

Figure 6.1: Generated spectral line shifting at two radial velocities.

To obtain the velocity either parallel or antiparallel to the laser propagation direction, Doppler Shift Velocimetry (DSV) is performed. DSV involves measuring the shift in line center of a spectral line by fitting a Gaussian function to the fluorescence spectra [Inman et al., 2013]. To make absolute measurements of velocity using the DSV method, a reference point is required where the velocity is equal to zero. The DSV function is fitted to a transition of the experimental PLIF spectra, leaving the velocity V_r as a free parameter:

$$DSV(V_r) = \delta_u + W_A e^{\frac{-4ln(2)(\nu-\nu_o-\delta_D(V_r)-\delta_r)}{\Delta_W^2}} \tag{6.1}$$

where W_A is a free parameter given by:

$$W_A = \frac{\chi_{NO} N_T I_L \Phi}{Z_p \sqrt{\Delta_W^2}} B_{12} \frac{F_b}{Z} t_{det} V_o \frac{\Omega}{4\pi} \eta \tag{6.2}$$

and $\delta_D(V_r)$ is the shift due to in-plane velocity (the radial velocity) given by Equation 3.9, and δ_r is the shift measured at a reference point where the velocity is zero.

To determine the radial velocity from the NO-PLIF data set, single-line DSV is performed. The data chosen for this analysis needs to have high spectral resolution to determine an accurate line center. Therefore, runs R4-R6 are used for this analysis due to their high spectral resolution. Tran-

sition line #18 ($J'' = 11.5$) was chosen for this analysis, since it is an independent transition (not an overlapped pair), therefore there is no added uncertainty from the slight off-set of overlapped transitions. Additionally, the spectral line is detected in all regions of the flow, meaning it can be used to acquire the velocity in the entire FOV in a single run. As mentioned, the DSV method requires a reference point where the velocity is zero, which in the current work is the centerline of the flow. As a result, the in-plane velocity could only be determined to the specimen surface, and not beyond it, since there is no centerline reference point. Therefore, the area illuminated by the laser to the side of the specimen is removed from NO-PLIF images for the DSV analysis.

Note that since the laser sheet is angled slightly toward the surface of the specimen, the velocity measured is not perfectly perpendicular to the flow direction. Therefore, an angular correction is applied to the measured velocity field that converts the measurement to the desired radial velocity perpendicular to the flow.

6.2 Rotational temperature

To measure the rotational temperature of the flow, the rotational temperature dependence of the Boltzmann fraction of each transition is utilized. Since the Boltzmann fraction represents the population fraction of a ground state energy level, the relative intensity of spectral lines changes based on rotational temperature. This effect is shown in Figure 6.2 where the transitions in spectral range B are generated at three different temperatures.

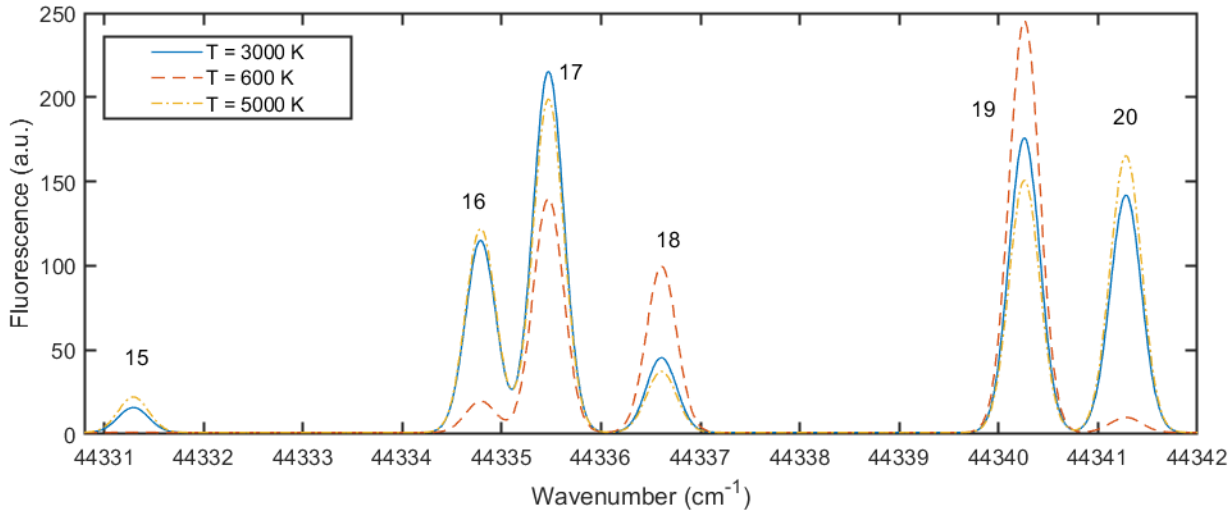

Figure 6.2: Generated spectra of transitions in Range B at expected three temperatures, with transition groups labelled.

The Boltzmann fraction rotational temperature dependence can also be visualized by plotting the term over a range of temperatures, as shown in Figure 6.3. This figure shows a range of transitions at different J'' values, and how the ground state population changes with temperature. Therefore, to maximize temperature sensitivity, a wide range of J'' values is needed. Spectral range A features transitions with lower J'' values, meaning it is appropriate for lower temperature regions such as the free-stream and shear-layer. Spectral range B features a wider range of J'' values, which indicates it can be used in both low and high temperature regions [Palma et al., 1999].

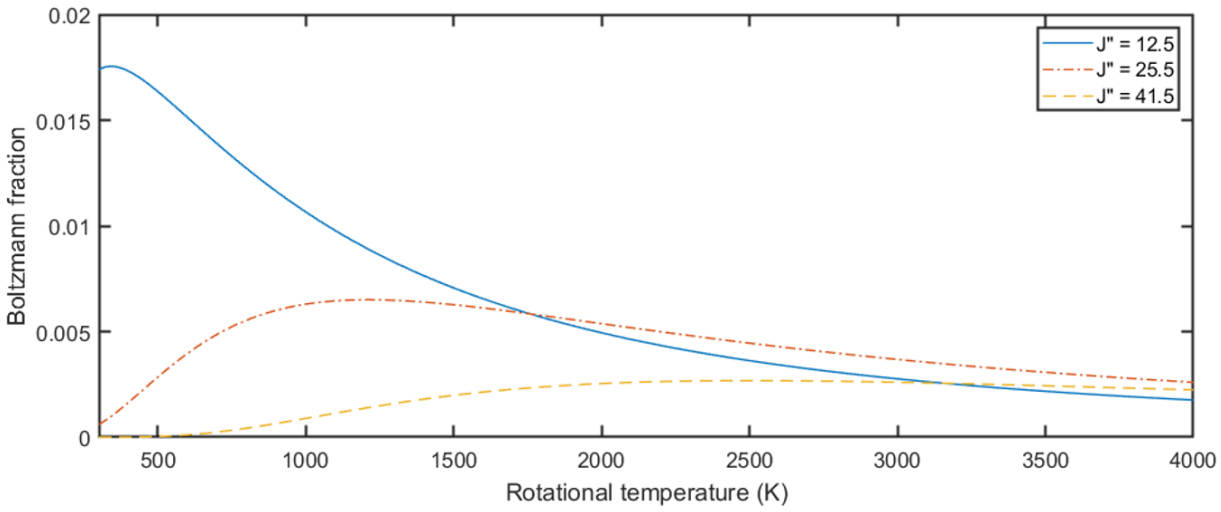

Figure 6.3: Boltzmann fractions for the $J'' = 12.5$, $J'' = 25.5$, and $J'' = 41.5$ transitions.

To obtain the rotational temperature, Spectral Peak Thermometry (SPT) is performed on the NO-PLIF spectra [McDougall et al., 2020a,b]. SPT is completed by fitting the following equation to two or more selected transition groups from the experimental NO-PLIF spectra, leaving the rotational temperature T_r as a free parameter:

$$SPT(T_r,k) = \delta_u + W_B \sum_{k=1}^{k} \frac{B_{12}(k)F_b(T_r,k)}{1+s(k)} e^{\frac{-4ln(2)(\nu-\nu_o(k)-\delta_W)}{\Delta_W^2}} \tag{6.3}$$

where k is a specific transition, and W_B is a free parameter given by:

$$W_B = \frac{\chi_{NO} N_T I_L \Phi}{Z_p \sqrt{\Delta_W^2}} t_{det} V_o \frac{\Omega}{4\pi} \eta \tag{6.4}$$

and F_b is given by Equation 3.13.

To determine the rotational temperature, multi-line SPT is performed for spectral ranges A and B over runs R2-R6. For run R2, the spectra is in the saturated regime, while runs R3 and R4 are below the saturation point. For all runs, the saturation value I_{SAT} along with the laser profile value I_L is used to calculate the saturation term s, regardless if the run is above or below the saturation point. Runs R2-R4 are analyzed at the same enthalpy condition, and will provide information about the repeatability of applying SPT in the arc-jet flow at different laser energies, spectral ranges and

spectral resolutions.

Note that an alternative thermometry technique was also developed over the course of the current work, which assumed the rotational and translation temperatures were in equilibrium. Due to initial observations of trans-rotational non-equilibrium occurring in the flow, this technique was determined to not be appropriate for this data set. The technique is described in Appendix C.

6.3 Translational temperature

To measure the translational temperature of the flow, the temperature dependence of the Doppler broadening of the transitions is utilized. A transition will broaden as the translational temperature increases, as described in Chapter 3. This effect is shown using generated spectra in Figure 6.4 where the spectral line is shown at two different translational temperatures.

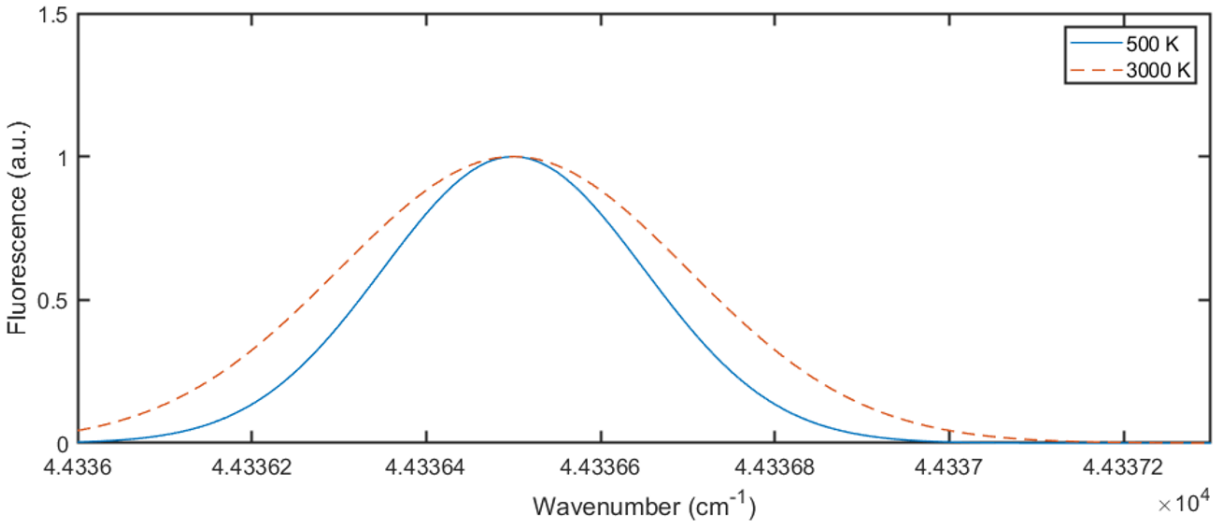

Figure 6.4: Generated spectral line broadening expected by Doppler broadening at two temperatures.

To obtain the translational temperature in each region of the flow, Doppler Broadening Thermometry (DBT) is performed [McDougall et al., 2020a,b]. DBT involves measuring the thermal Doppler broadening effect of the spectral lines to determine the translational temperature. Note that since the facility is at low pressure, collisional broadening is not significant, and is not in-

cluded in the model. DBT is completed by fitting the following equation to a transition from the experimental PLIF spectra, leaving the translational temperature T_t as a free parameter:

$$DBT(T_t) = \delta_u + W_C e^{\frac{-4ln(2)(\nu-\nu_o-\delta_W)}{\Delta_D(T_t)^2+\Delta_L^2}} \tag{6.5}$$

where W_C is a free parameter given by:

$$W_C = \frac{\chi_{NO} N_T I_L \Phi}{Z_p \sqrt{\Delta_D(T_t)^2 + \Delta_L^2}} B_{12} \frac{F_b}{Z_p} t_{det} V_o \frac{\Omega}{4\pi} \eta \tag{6.6}$$

and $\Delta_D(T_t)$ is given by Equation 3.8.

In the current work, single-line DBT is performed for spectral range B over runs R4-R6, utilizing transition #18 (J'' = 11.5). This is the only transition in Range B that is not overlapped (single transition), which ensures the most accurate measurement of the Doppler broadening term. Additionally, this transition is populated in all regions of the flow, so translational temperature can be obtained in each region. For each run analyzed, the laser is tuned below the saturation point, therefore saturation broadening is not considered significant, which normally occurs when the spectra is highly saturated [Palma et al., 1999]. The laser linewidth produced in the initial gas cell study is required for this measurement and is included as the Δ_L term in the DBT fit equation. Spectral range A is not used for this measurement due to the coarse spectral resolution, which would lead to an inaccurate determination of the width of the transition.

Chapter 7

COMPUTATIONAL METHODOLOGY

This chapter details the quasi-1D three-temperature solver developed in the current work to investigate thermal non-equilibrium in the arc-jet nozzle. Three-temperature modelling is not found in previously used solvers for simulating arc-jet facilities, and is added to a 1D solver here. The chapter begins with an overview of the solver, followed by sections detailing the governing equations, discretization scheme, and an assessment of the solver.

7.1 Overview

To numerically evaluate the complex thermal non-equilibrium effects occurring in the HyMETS arc-jet facility under a wide variety of conditions, a low-fidelity quasi-1D solver was developed in the current work. The solver (referred to as the Aerothermodynamic Relaxation Code - ARC1D) is a transient, three temperature (translational, rotational and vibrational) non-equilibrium solver and was developed to determine the properties in the nozzle of the HyMETS facility. The solver employs the explicit MacCormack predictor-corrector finite-difference scheme to solve the unsteady 1D Navier-Stokes equations through the nozzle [Anderson Jr, 2006]. The time-dependence of the analysis is used as a "means to an end" to achieve a steady-state solution [Anderson Jr, 2006]. The vibrational-translational and rotational-translational energy exchange between modes of the diatomic species are modelled in the current solver. The Landau-Teller relaxation model was used to approximate the vibrational energy mode, while the Parker model was used to capture the rotational energy mode [Landau and Teller, 1936; Parker, 1959]. The airNASA9 library was utilized to calculate needed flow variables for the solver [Goodwin et al., 2009]. This library has a valid temperature range up to 20,000 K for the species modelled in the current work. Chemical reaction modelling is not included in the nozzle calculation since chemical reactions are largely frozen

from the entrance of the nozzle onward, based on prior CFD and experimental results [Brune et al., 2019; Johansen et al., 2016]. ARC1D employs Cantera, an open source equilibrium chemical kinetics and thermodynamics solver, to determine the equilibrium composition of the mixture in the plenum (reservoir) at a given enthalpy condition [Goodwin et al., 2009]. The species mixture is used to then calculate the boundary conditions for the ARC1D solver. Note that the nozzle geometry used for this analysis is identical to the HyMETS facility nozzle, which is shown in Figure 2.5. The electronic mode of molecules is not modelled in the current study.

7.2 Governing equations

The ARC1D solver was developed based on information from Anderson Jr [1970] that employed trans-vibrational non-equilibrium modelling. The current work includes an additional energy equation for rotational non-equilibrium. The following non-dimensionalized equations, representing the conservation of continuity, momentum, and energy (split into individual equations for each of the translational, rotational and vibrational modes) are discretized using the MacCormack method to produce the solution within the nozzle:

$$\frac{\partial Z}{\partial t'} = -u' \left[\frac{\partial ln(A'_r)}{\partial x'} + \frac{\partial V}{\partial x'} + \frac{\partial Z}{\partial x'} \right] \tag{7.1}$$

$$\frac{\partial V}{\partial t'} = -\frac{T'_t}{\gamma_o u'} \left[\frac{\partial \phi}{\partial x'} + \frac{\partial Z}{\partial x'} \right] - u' \frac{\partial V}{\partial x'} \tag{7.2}$$

$$\frac{\partial \phi}{\partial t'} = -\frac{2}{3} \left[u' \frac{\partial V}{\partial x'} + u' \frac{\partial ln(A')}{\partial x'} + \frac{w_d}{T_t} (e'_{vib} \frac{\partial \theta}{\partial t'} + e'_{rot} \frac{\partial \Omega}{\partial t'} + u' e'_{vib} \frac{\partial \theta}{\partial x'} + u' e'_{rot} \frac{\partial \Omega}{\partial x'}) \right] - u' \frac{\partial \phi}{\partial x'}; \tag{7.3}$$

$$\frac{\partial \theta}{\partial t'} = \frac{1}{\tau'_v} \left[\frac{e^{eq'}_{vib}}{e'_{vib}} - 1 \right] - u' \frac{\partial \theta}{\partial x'} \tag{7.4}$$

$$\frac{\partial \Omega}{\partial t'} = \frac{1}{\tau_r'}\left[\frac{e_{rot}^{eq'}}{e_{rot}'} - 1\right] - u'\frac{\partial \Omega}{\partial x'} \tag{7.5}$$

where $Z = ln(\rho')$, $V = ln(u')$, $\phi = ln(T')$, $\theta = ln(e_{vib}')$, $\Omega = ln(e_{rot}')$, τ_v is the vibrational relaxation time, τ_r is the rotational relaxation time, A_r is the area ratio of the nozzle, e_{vib} is the vibrational energy, e_{rot} is the rotational energy, u is the axial velocity, T_t is the translational temperature, ρ is the gas density, and w_d is the diatomic species mass fraction. The "eq" superscript indicates the equilibrium value of the term, and the primed superscript indicates a non-dimensionalized value. These variables are non-dimensionalized using the plenum variable values (nozzle entrance) or the nozzle throat diameter. Derivations of the continuity and momentum equations are found in the literature [Anderson Jr, 2006]. For the derivation of the energy equations, see Appendix A.

The vibrational relaxation time τ_v is determined using an equation of the same form as Landau-Teller:

$$\tau_v = \frac{C_1}{p} e^{(\frac{C_2}{T_t})^{1/3}} \tag{7.6}$$

The rotational relaxation time is calculated using the Parker model [Parker, 1959]:

$$\tau_r = \frac{\tau_c Z_\infty}{1 + \pi(1 + \frac{\pi}{4})\frac{T_{or}}{T_t} + \frac{\pi^{3/2}}{2}\sqrt{\frac{T_{or}}{T_t}}} \tag{7.7}$$

where Z_∞ is the infinite temperature collision number, T_{or} is a reference temperature, τ_c is the mean collision time, given by the following expression:

$$\tau_c = \frac{\pi \mu}{4p} \tag{7.8}$$

where μ is the dynamic viscosity, calculated using the Sutherland viscosity model.

The solver requires a large number of experimentally or theoretically derived constants that are found in the literature [Parker, 1959; Anderson Jr, 2006]. In the case where a constant was not available for NO, the constants for O_2 and N_2 were averaged, as has been previously done in the

Table 7.1: Non-equilibrium rate constants.

Variable	N_2	O_2	NO
C_1 (atm μs)	7.12×10^{-3}	5.42×10^{-5}	4.86×10^{-3}
C_2 (K)	1.91×10^{6}	2.95×10^{6}	1.37×10^{5}
T_{or} (K)	91.5	113.5	100
Z_∞	23.3	16.5	19.5

literature [Abe et al., 2005]. The averaged constants are computed by a weighted average based on the species mass fraction from equilibrium chemistry calculations from Cantera. The constants used in the current work are listed in Table 7.1.

7.3 Discretization scheme

The ARC1D solver uses the MacCormack explicit finite difference predictor-corrector scheme to discretize and solve the governing equations outlined in the previous section [MacCormack, 2003]. The method consists of two steps, a "predictor" step and a "corrector" step. Beginning with the predictor step, the following equation can be defined for a variable X:

$$X_{i,p}^{t+\Delta t} = X_i^t + \left(\frac{\partial X}{\partial t}\right)_p \Delta t \tag{7.9}$$

where i is a node/grid point, subscript p indicates the predictor step, and Δt is the time step. To solve this equation, all derivatives are replaced with forward differences in the governing equations. The result is then used to replace the predictor time derivative in Equation 7.9 to determine predicted values for any variable X_p for that time step.

The corrector step then replaces all spatial derivatives in the governing equations with rearward differences, while using the predictor step variables X_p. The result is then used to replace the corrector time derivative in the following equation, along with the predictor time derivative already found:

$$\left(\frac{\partial X}{\partial t}\right)_{avg} = \frac{1}{2}\left(\left(\frac{\partial X}{\partial t}\right)_p + \left(\frac{\partial X}{\partial t}\right)_c\right) \tag{7.10}$$

where subscript c indicates the corrector step. Then, the final variable values can be calculated using the following equation:

$$X_i^{t+\Delta t} = X_i^t + \left(\frac{\partial X}{\partial t}\right)_{avg} \Delta t \tag{7.11}$$

This process is completed at all grid points for a large number of time steps. After a sufficient number of time steps have been calculated, the solution will converge on a steady state solution for all variables. In this way, using this time-marching approach is a method of obtaining the steady state solution [Anderson Jr, 2006].

For non-equilibrium flows, a time step must be chosen that is shorter than the fastest process in the flow, which in current work is the rotational relaxation time, τ_r. Therefore, the time step of ARC1D must satisfy the following criterion:

$$\Delta t < \beta \tau_r \tag{7.12}$$

where β is a dimensionless constant normally less than unity for the MacCormack method to reach a stable solution. In the current work, a β value of 0.5 was determined to produce consistently stable results. The rotational relaxation times are normally on the order of 10^{-5} seconds for the conditions simulated in the current work, therefore the time step Δt is on this order of magnitude as well. This is a significantly shorter time step than other works that have implemented the MacCormack method, which is due to the quick rotational relaxation time [Anderson Jr, 2006].

Since the equations are solved for the translational temperature and the rotational and vibrational energy terms, the remaining temperature fields are calculated from the definition of each energy mode, where vibrational energy is defined as:

$$e_{vib} = \left[\frac{h\nu/kT_v}{e^{h\nu/kT_v} - 1}\right] RT_v \tag{7.13}$$

and rotational energy is defined as:

$$e_{rot} = RT_r \tag{7.14}$$

Since the vibrational temperature is implicitly defined in Equation 7.13, the Newton-Raphson numerical method was used to solve for T_v.

7.4 Model assessment

ARC1D was assessed using data that was readily available at the time of publication. There is a limited availability of experimental data for nozzle flows with thermal non-equilibrium occurring across all three temperatures of a gas. Therefore, this section attempts to verify and validate the ARC1D model as thoroughly as possible with the data available. Future work, as more experimental and high fidelity computational data becomes available, includes completing a systematic verification and validation of the ARC1D model.

The number of time steps for convergence to the steady state solution were analyzed in the current work. The steady state distribution is reached after a certain number of time steps have proceeded, until the property fields of the simulation are unchanging. This process can be visualized by plotting the residuals (the change in value of a specific property between time steps). Once the residuals approach zero and are unchanging, the steady state solution has been found. Due to the short time frame of the rotational relaxation process, the required time step is significantly smaller, and therefore more time steps are required than what has been reported in the literature for vibrational non-equilibrium nozzle flows [Anderson Jr, 1970]. The residuals of the flow properties over time, and the convergence to the steady state solution of the rotational temperature field, is shown in Figure 7.1. This figure shows the solution is sufficiently stable over approximately 4000 time steps. The current work allows the solution to proceed to 10,000 time steps, well past this threshold.

A grid resolution study was completed on ARC1D to determine the resolution necessary to

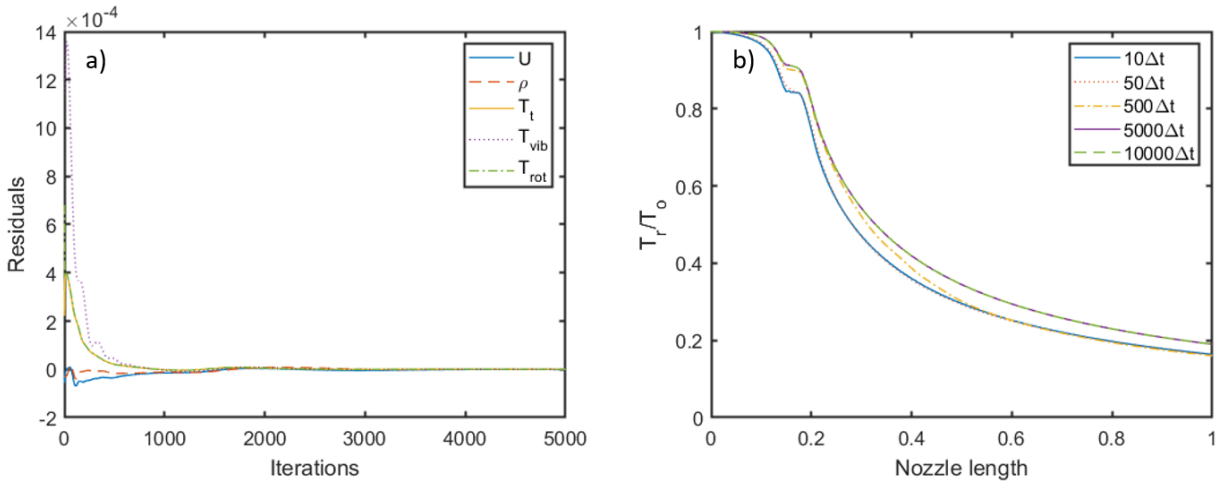

Figure 7.1: Time step convergence study of the ARC1D solution showing a) the residuals of flow properties and b) the rotational temperature field at specific time steps. This analysis was performed at the 5.7 MJ/kg enthalpy condition.

ensure the solution is independent from the grid size used. The number of nodes (n) spaced evenly through the nozzle were increased across the range from 10 to 250. The results from this analysis are shown in Figure 7.2, where the rotational, vibrational and translational temperatures and axial velocity are plotted at various grid sizes. It was determined that above 200 nodes was sufficient for grid independence. The current work uses 500 nodes, as this still minimized computation time (on the order of minutes) while providing a grid well above the minimum grid resolution. Note that the twist in the property profiles at a nozzle length of approximately 0.2 in Figure 7.2 is expected due to the sharp geometry of the nozzle throat (see Figure 2.5).

The ARC1D solver was verified against results found in the literature for vibrational non-equilibrium [Anderson Jr, 1970]. The verification data is shown in Figure 7.4, where the ARC1D solver produces the same vibrational temperature in the nozzle as Anderson Jr [1970] to within 1% relative error, on average. A reason for small discrepancies could be due to digitization of data acquired from a printed work. ARC1D was also used to compare to a high-fidelity, axisymmetric simulation completed of the HyMETS facility. Figure 7.3 shows the non-dimensionalized translational, rotational and vibrational temperatures calculated for the 10.5 MJ/kg enthalpy condition presented by Brune et al. [2019]. The results are overlayed with the axisymmetric two-temperature

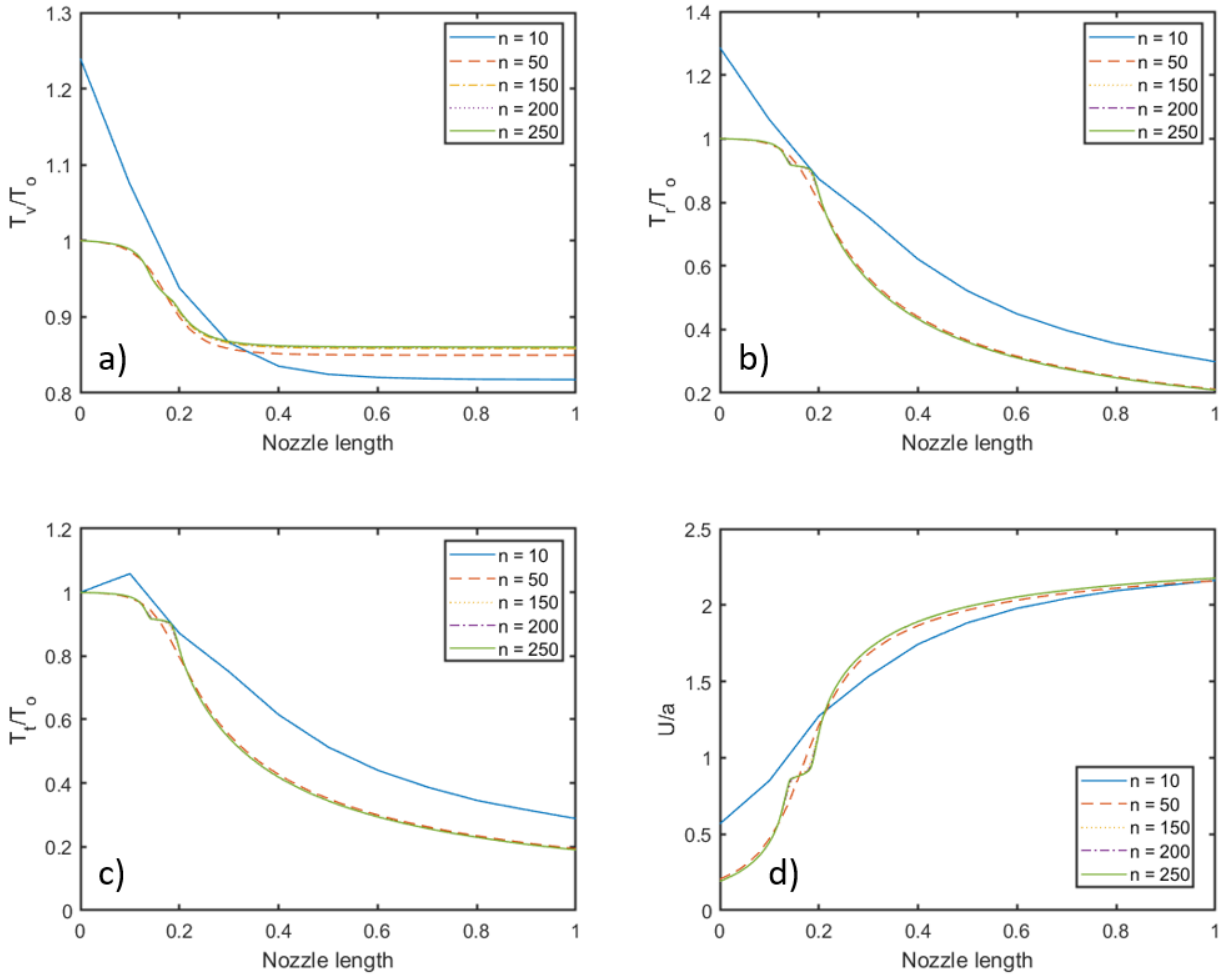

Figure 7.2: Grid convergence study of the ARC1D solution for a) vibrational, b) rotational and c) translational temperatures, and d) the axial velocity, at the 5.7 MJ/kg enthalpy condition.

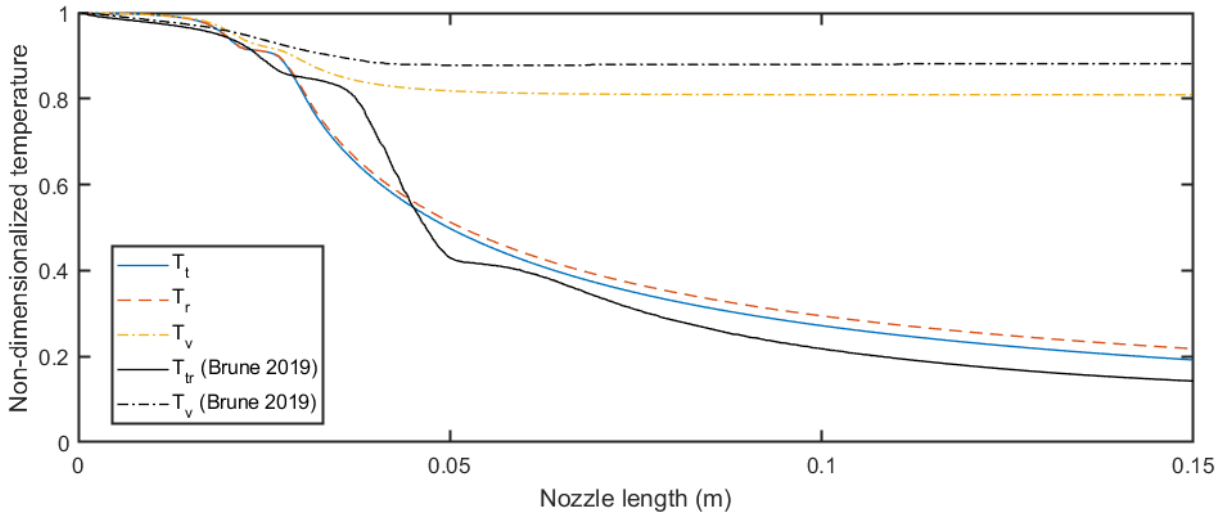

Figure 7.3: Comparison between ARC1D and full CFD simulation by Brune et al. [2019] at a bulk enthalpy condition of 6.7 MJ/kg.

CFD results from Brune et al. [2019]. Reasonable agreement is observed, considering the comparison is between axisymmetric and quasi-1D models. The study by Brune et al. [2019] adds additional complexity such as determining an enthalpy profile across the plenum, which cannot be captured with ARC1D. The plots from the axisymmetric CFD are presented on the centerline of the flow. ARC1D is on average within 10% of the CFD values. The vibrational temperature for the 1D model reaches a constant temperature lower than in the axisymmetric results. Data could not be found to verify or validate the 3-temperature non-equilibrium modelling due to a lack of studies that report this data. Due to the similarities in how the rotational model is treated in the literature to the vibrational model presented by Anderson Jr [1970], there is reasonable confidence ARC1D is accurately capturing the three-temperature model [Parker, 1959].

The primary purpose of the 3-temperature ARC1D solver in the current study is to evaluate the effects of vibrational and rotational non-equilibrium in the HyMETS nozzle and determine if assumptions of trans-rotational equilibrium made in previous studies are valid. The previous studies all completed computational or experimental works in the HyMETS facility [Danehy et al., 2012; Johansen et al., 2016; Brune et al., 2019; Inman et al., 2013]. The results from ARC1D are presented in the following chapter.

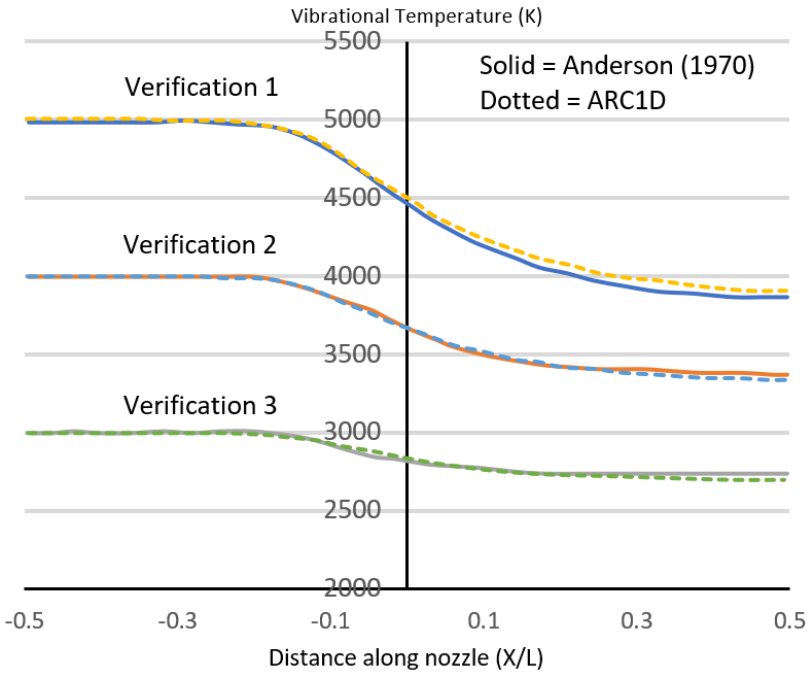

Figure 7.4: Verification of trans-vibrational non-equilibrium ARC1D model against data from Anderson Jr [1970].

Chapter 8

RESULTS & DISCUSSION

This chapter presents the results from the quantitative measurements completed in the current study, as well as the computational results from ARC1D. Comparisons with previous works from the literature are also included near the end of the chapter. In addition to providing unique velocity and temperature data to characterize the HyMETS arc-jet facility and providing a means to validate numerical models for these high-enthalpy hypersonic flows, the results presented in this chapter focus on the thermal non-equilibrium effects that are observed. A combination of experimental results, simulation prediction, and results reported in the literature are used to understand the importance of thermal non-equilibrium effects that occur in this facility. Uncertainty bars are calculated using the methodology outlined in Appendix B, unless otherwise noted. The total uncertainty in the current work is normally dominated by flow unsteadiness which is captured in the NLLS fit uncertainty, while other contributions are generally minor. In all figures with quantitative measurement profiles, only every tenth data point is included for viewing clarity. The quantitative measurement maps are presented at full resolution. Refer to Table 4.2 for the complete set of conditions for each experimental run referred to in the current chapter. Note that discussion on the initial study results is not provided in this chapter and is located in Chapter 5.

Based on the results and interpretation presented in this chapter, additional experimental data was desired, but due to access and expense limitations of the HyMETS facility during the course of this work, only the data from the experimental campaign detailed in Chapter 4 was able to be obtained and analyzed.

8.1 Velocimetry

Using the DSV methodology outlined in Chapter 6, contours of radial velocity are presented at each enthalpy condition for runs R4 (5.7 MJ/kg), R5 (6.9 MJ/kg) and R6 (8.4 MJ/kg) in Figure 8.1. While the SNR deteriorates at higher enthalpy conditions due to a reduction of NO in the flow, the velocity distribution appears qualitatively similar across all of the enthalpy conditions. Figure 8.2 shows transverse profiles of radial velocity at stream-wise locations in the free-stream (x = 12mm) and in the post-shock (x = 4 mm). Note that x = 0 mm corresponds to the specimen surface. Also presented are the DSV NLLS fits to the experimental NO-PLIF spectra in Figure 8.3.

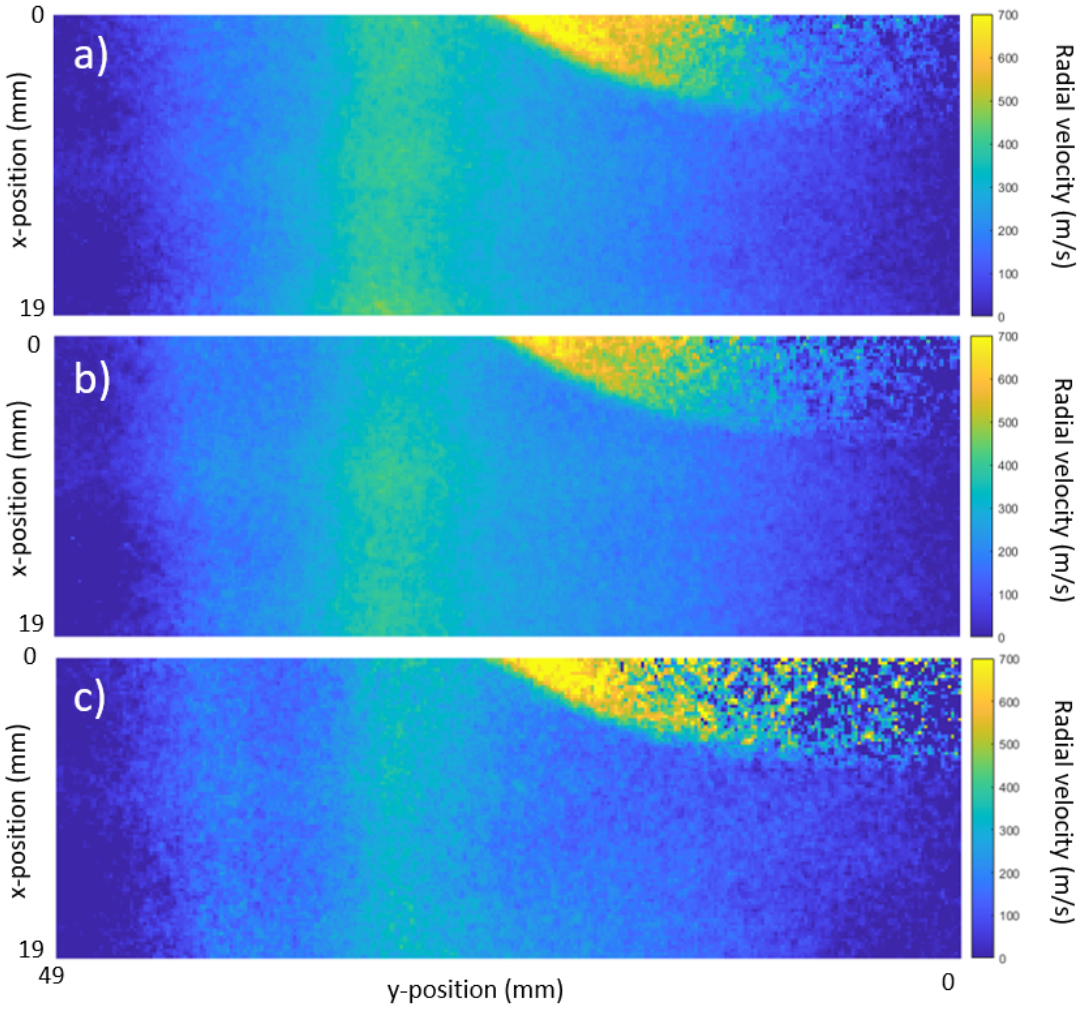

Figure 8.1: DSV radial velocity maps for each enthalpy condition: a) R4 - 5.7 MJ/kg, b) R5 - 6.9 MJ/kg, c) R6 - 8.4 MJ/kg.

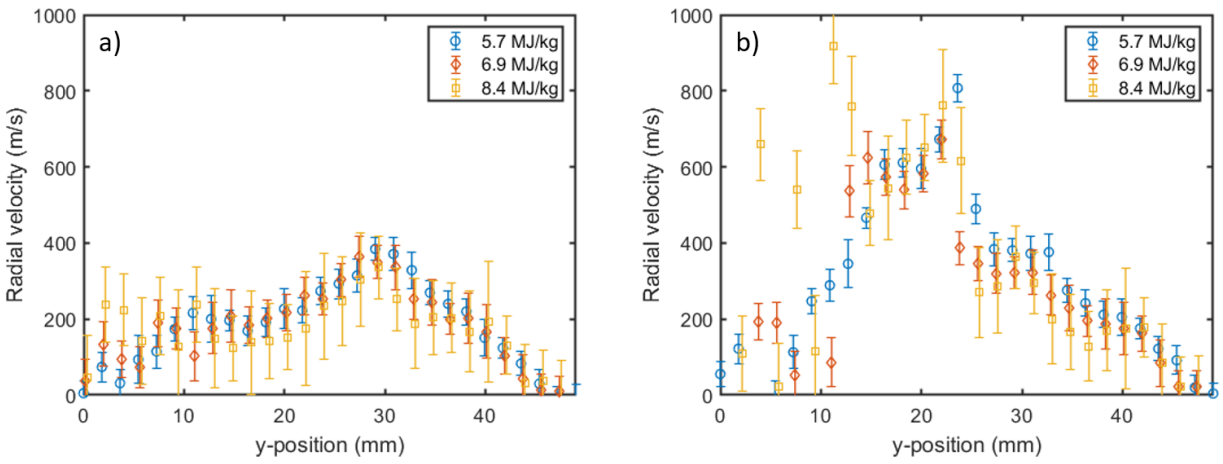

Figure 8.2: Velocity profiles at a) x = 12 mm and b) x = 4 mm.

As expected, the radial velocity results confirm that the flow is expanding in the free-stream. The shear-layer region shows a significant radial velocity component of approximately 300-400 m/s. The expanding flow indicates the facility nozzle is underexpanded, where the test section pressure is less than the nozzle exit pressure. The radial component appears to decrease at higher enthalpy conditions, and is supported by previous velocimetry completed by Inman et al. [2013], as shown in Figure 2.3. In general, this observation was unexpected when considering a typical equilibrium nozzle flow. As the enthalpy was increased from Runs R4 to R6, the mass flow rate was held constant. As a result, the plenum pressure was increased from Runs R4 to R6. With a constant test section pressure, the flow would be expected to be more underexpanded as the enthalpy is increased. Therefore, the nozzle was expected to be further underexpanded at higher enthalpy due to higher exit pressure, and subsequently produce a higher radial velocity component in the core flow during expansion in the test section. This is also supported by the facility-measured plenum and test section pressures (Table 8.1), which show a slightly increasing pressure ratio as enthalpy is increased. A likely explanation for the decrease in radial velocity is due to measurement error, since the radial velocity measurement becomes less accurate as enthalpy is increased due to decreasing NO in the flow, which is inversely related to enthalpy condition [Inman et al., 2013]. Alternatively, chemical and thermal non-equilibrium effects may explain this unexpected

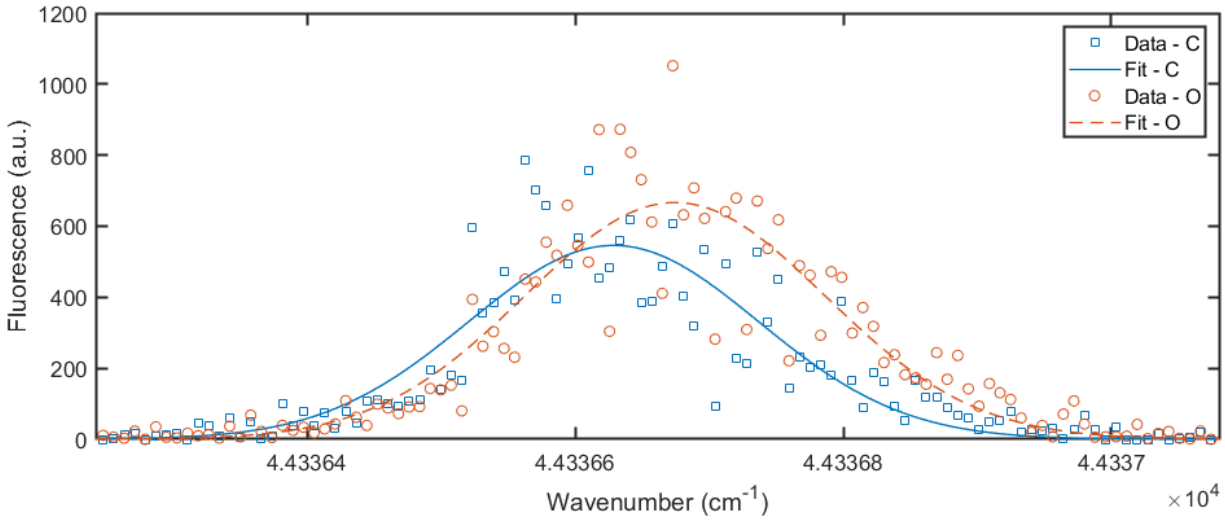

Figure 8.3: DSV spectral fits overlayed on experimental NO-PLIF spectra at x = 12 mm at the 5.7 MJ/kg enthalpy condition on the centerline (C) and off-center (O) at y = 25 mm.

Table 8.1: Measured facility pressures.

Run	Bulk enthalpy (MJ/kg)	Plenum pressure (kPa)	Test section pressure (Pa)	Pressure ratio (10^3)
R4	5.7	98	166	0.59
R5	6.9	108	173	0.62
R6	8.4	116	184	0.64

observation. Bulk enthalpy of the flow determines the species mixture in the plenum produced from the injected gases, which is then chemically frozen through the nozzle, and can affect the exit velocity due to the properties of the mixture [Brune et al., 2019]. Additionally, the vibrational temperature of the diatomic species in the flow is frozen through the nozzle, as predicted in a previous computational study [Brune et al., 2019]. The energy locked in the vibrational mode is unavailable to the translational or rotational modes, and therefore skews these temperatures lower at the nozzle exit than they would be under thermal equilibrium conditions. These chemical and thermal effects, when considered together, may explain why the nozzle becomes less underexpanded as the enthalpy of the flow is increased.

In past studies, radial velocimetry has been used to validate computational solvers [Inman et al., 2013; Brune et al., 2019]. The results from the current work show that radial velocity is relatively

insensitive to enthalpy condition when considering the associated uncertainty with the DSV measurement. Therefore, the radial velocimetry data acquired is not ideal for the validation of CFD models on its own. Ideally, a validation data set would present significantly different radial velocity fields at varied input conditions. With the current velocimetry data, a CFD solver could not be validated effectively within the associated uncertainty range of the experimental measurements. To produce a significantly different radial velocity field, the pressure ratio across the nozzle needs to be tuned such that the nozzle expansion process changes. Varying the pressure ratio variable would change the radial velocity field, and result in a more diverse data set that can be used effectively for CFD validation.

The NLLS fit uncertainty associated with the velocity measurement was highly variable across each spatial location in the flow. This variability can be observed in Figure 8.2 as the main contributor to the uncertainty bars. This variation is likely due to unsteadiness in the flow, which results in highly scattered experimental data, especially around the peak of the spectral line, as shown in Figure 8.3. This uncertainty is slightly larger in the post-shock region. However, due to larger spectral shifting (due to higher radial velocity) in the off-center post-shock regions, the uncertainty does not scale to the same level as the unsteadiness detected in the post-shock region. This scatter in the spectral peak results in highly variable uncertainty in the line center, which is reflected as variations in uncertainty bars in the reported velocimetry data.

As shown in Figure 8.1, radial velocities in the post-shock region were measured up to approximately 750 m/s as the flow expands around the flat-faced specimen. There is no clear relationship observed between the post-shock velocity and the enthalpy condition of each run. This work is the first velocimetry data acquired in the post-shock region around a sample in the HyMETS arcjet facility. In both the free-stream and shear-layer regions, the spectral fits appear to capture the experimental spectra shape accurately, as shown in Figure 8.3. The velocimetry results presented form a data set that could be used to validate computational solvers, as has been done in prior studies [Brune et al., 2019]. However, additional data should be added at varied pressure ratios to

diversify the data set to be more effective in validation studies, as mentioned earlier in this section.

8.2 Thermometry

Using the SPT and DBT methodologies outlined in Chapter 6, rotational and translational temperatures were measured from the experimental NO-PLIF data. The effects of the spectral scanning range, spectral resolution and laser energy on rotational temperature measurements were investigated first on data from runs R2-R4, followed by high spectral resolution SPT and DBT analysis covering three enthalpy conditions in runs R4-R6.

The rotational temperature measurement radial and centerline profiles for the 5.7 MJ/kg enthalpy condition from runs R2-R4 are shown in Figure 8.4. The results are shown to compare the SPT method across multiple spectral ranges, spectral resolutions and laser energies. Post-shock results are not included, as spectral range A does not include higher ground state transitions (i.e. high J'' values), meaning the range has low temperature sensitivity at high temperatures.

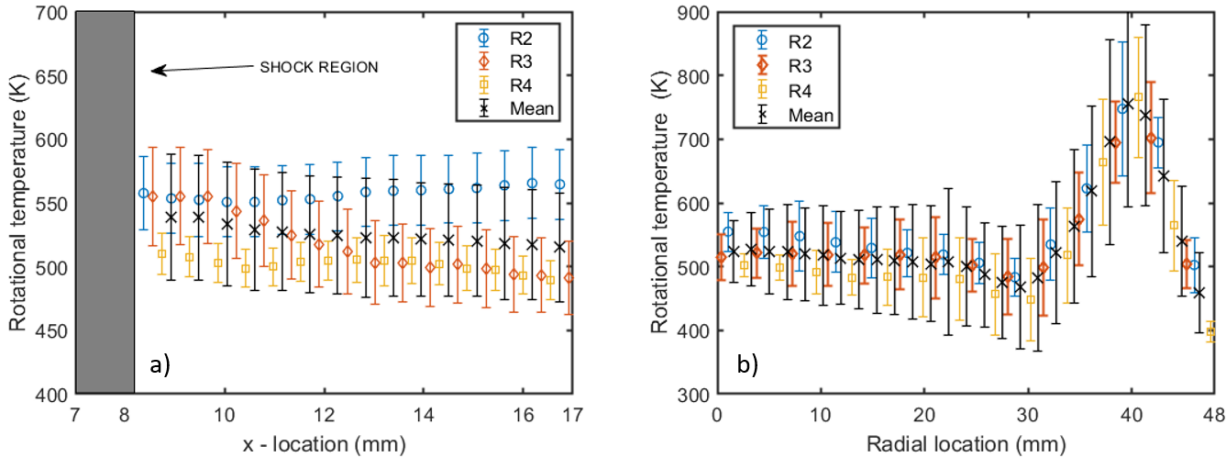

Figure 8.4: SPT free-stream rotational temperature measurements for runs R2, R3 and R4, as well as the mean temperature, on the a) centerline and b) radial profile at x = 12 mm, at the 5.7 MJ/kg enthalpy condition.

The results in Figure 8.4 show how the input spectral range and laser energy have a larger relative impact on temperature trends in the stream-wise direction than perpendicular to the flow. When analyzing the results in Figure 8.4a closer, the centerline trends between each run are no-

ticeably different. Moving toward the bow shock, the temperature measurement from run R2 is decreasing in rotational temperature while runs R3 and R4 are increasing. The exact cause of this trend is not known, but may be due to a systematic error in a stream-wise variable included in the SPT model such as the saturation term. The laser energy is measured at each stream-wise location using the sheet profiling camera data, which is then used to calculate the saturation parameter, s. Since the sheet profile is quite non-uniform across the sheet cross section (as shown in Figure 5.7), the saturation modelling in the SPT model could have varying accuracy across the laser sheet width (corresponding to different stream-wise positions), and across different spectral ranges, resulting in a systematic error in the SPT outputs.

Also presented in Figure 8.4 is the mean of the runs R2-R4, with associated uncertainty bars that are calculated from the average deviation between the runs. This analysis produced uncertainty bars which indicate the temperature measurement has an uncertainty of approximately $\pm$ 52K. In prior works in the literature, quantitative measurements have fluctuated significantly between runs in the HyMETS facility, indicating the facility itself may produce different flow conditions between experiments [Danehy et al., 2012]. Overall, the repeatability results show close agreement between runs when considering the unsteadiness of the flow, and the lack of experimental repeatability observed previously in the HyMETS arc-jet [Danehy et al., 2012]. These results provide an assessment of the uncertainty of the SPT model, which is based on the physics of the rotational temperature dependence of the LIF signal over multiple spectral ranges, spectral resolutions and laser energies.

The high spectral resolution runs R4-R6 are analyzed using SPT and DBT to produce rotational and translational temperature measurement maps for three enthalpy conditions (5.7 MJ/kg, 6.9 MJ/kg, 8.4 MJ/kg) in Figure 8.5. The corresponding radial and centerline profiles are presented in Figure 8.6. Spatial averages of rotational and transitional temperature in the freestream (8 mm $<$ x $<$ 15 mm) and post-shock (1 mm $< x <$ 5 mm) regions were computed and are shown in Figure 8.8.

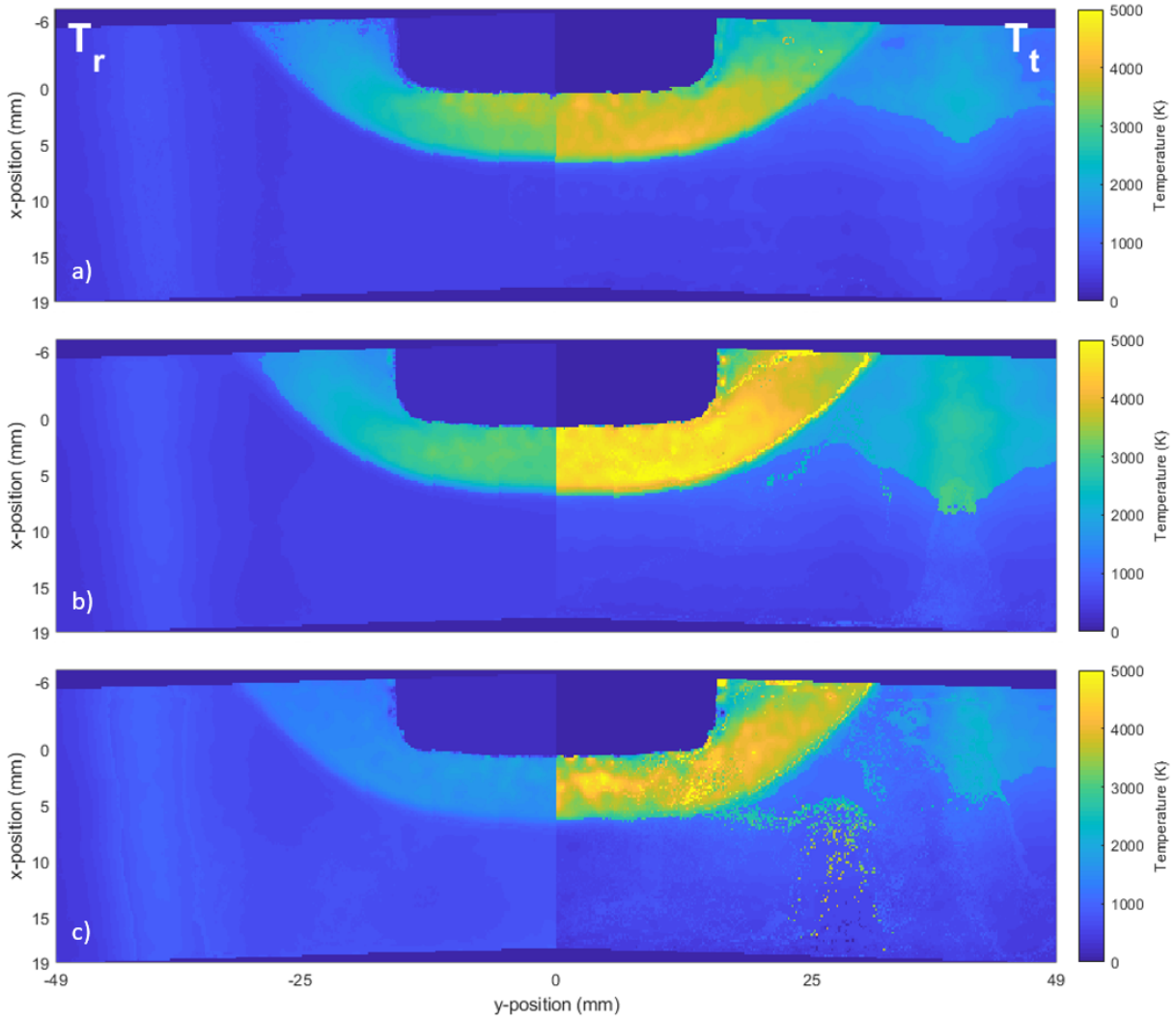

Figure 8.5: Rotational & translational temperature maps for each enthalpy condition: a) R4 - 5.7 MJ/kg, b) R5 - 6.9 MJ/kg, and c) R6 - 8.4 MJ/kg.

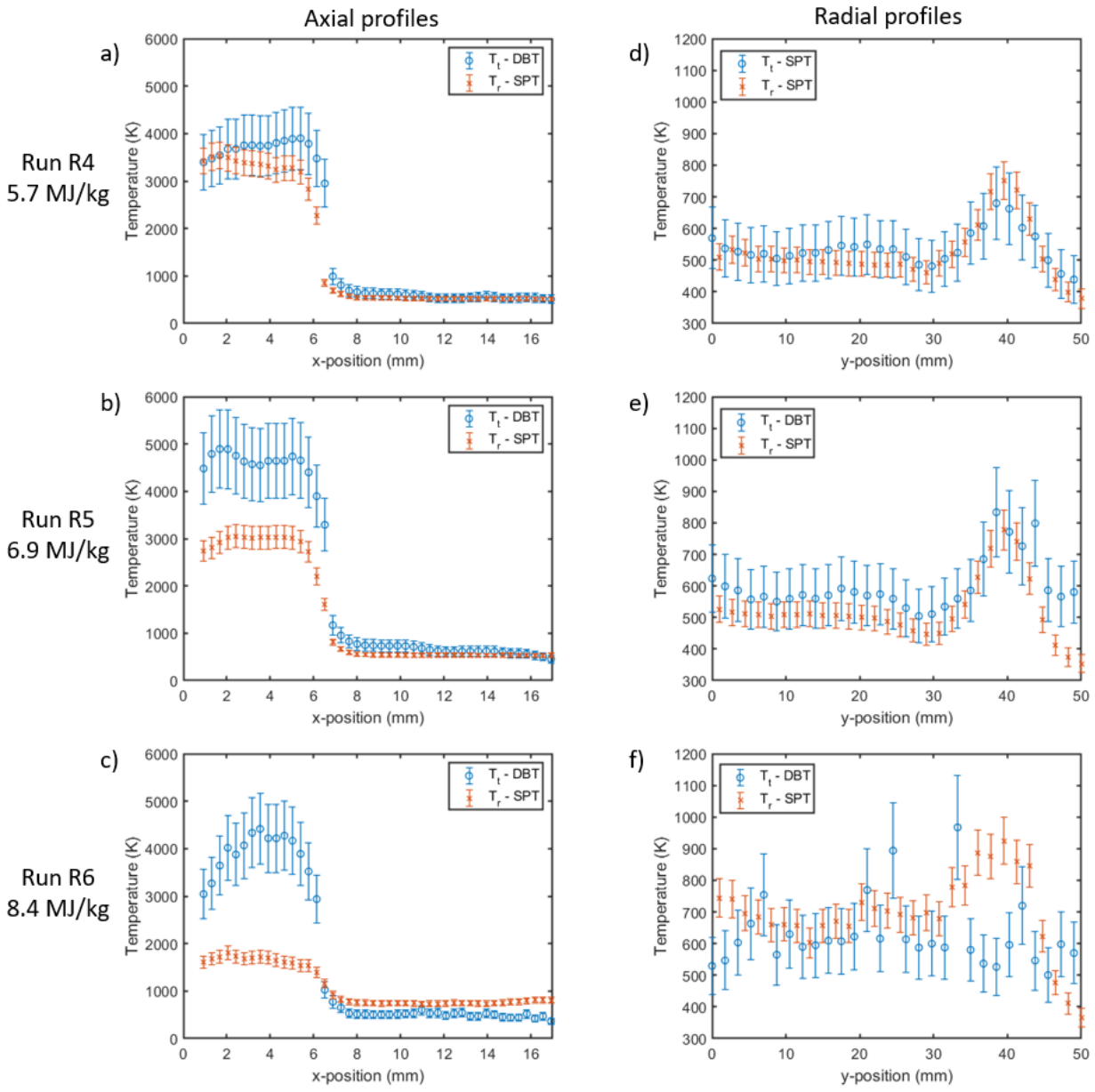

Figure 8.6: SPT and DBT along the centerline (a-c) and radial profiles (d-f) at x = 12 mm.

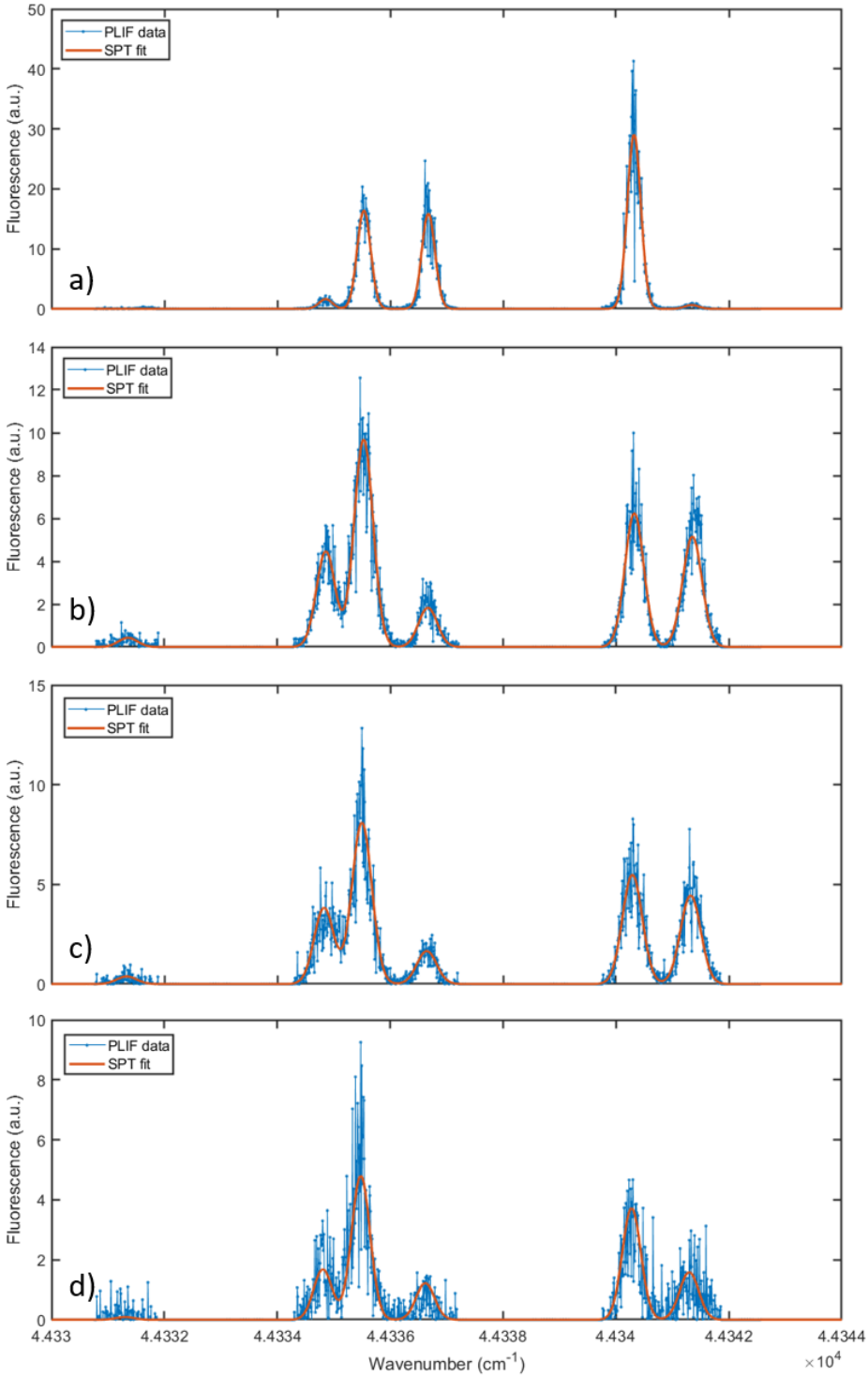

Figure 8.7: SPT fits for a) R4 (5.7 MJ/kg) free-stream, b) R4 (5.7 MJ/kg) post-shock, c) R5 (6.9 MJ/kg) post-shock, and d) R6 (8.4 MJ/kg) post-shock regions.

The SPT NLLS spectra fits are presented in Figure 8.7. The fits for DBT (translational temperature measurement) are identical to DSV, and are shown for two locations in Figure 8.3. These fits are constrained by terms of the fluorescence equation that are dependent on the rotational and translational temperature, as outlined in Chapter 6. The SPT spectral fits conform closely to the experimental data, indicating the fluorescence modelling used in the current work is capturing the physics occurring in the spectra. When combined with the repeatable results shown in Figure 8.4, the current work shows high confidence in the SPT method when performance is quantified in multiple ways (spectral fits, run repeatability over multiple laser energies, spectral resolutions and spectral ranges). The DBT fits conform well to the NO-PLIF data in runs R4-R6. However, the repeatability of this measurement was not quantified, due to a lack of high spectral resolution data which is required for the DBT method. Overall, there is higher confidence in the rotational temperature measurement, and this should be considered when interpreting the results in the current chapter.

In runs R4 and R5 (enthalpy conditions 5.7 and 6.9 MJ/kg, respectively), results in the free-stream in Figure 8.6 agree well between the translational and rotational temperatures, indicating the flow is in trans-rotational thermal equilibrium. Run R6 produced a lower translational temperature than rotational temperature in the free-stream. This could indicate the flow is experiencing trans-rotational non-equilibrium. However, when observing the spread in translational measurements in the radial profile in Figure 8.6f, it is likely that this observation is due to a measurement error. As enthalpy condition increases, the NO fluorescence observed in the flow decreases, as observed in the current and previous studies [Inman et al., 2013], which can affect the quantitative DBT measurement due to decreased SNR.

In the post-shock region, the translational and rotational temperatures diverge, indicating trans-rotational non-equilibrium is occurring. Trans-rotational non-equilibrium occurs across a shock-wave when the rotational mode cannot exchange energy with the translational mode on a short time scale to remain in equilibrium, therefore the temperatures diverge. This measured non-equilibrium

in the thermometry results increases as enthalpy condition increases, as shown in Figure 8.6. In the literature, a computational study by Gardner and Agarwal [2019] noted post-shock non-equilibrium in front of a blunt body at high Knudsen numbers, as shown in Figure 2.6. This study determined the free-stream Knudsen number to be an important predictor of trans-rotational non-equilibrium in the post-shock region in front of a blunt body. Using the same methodology as Gardner and Agarwal [2019] (blunt body diameter used as the reference length), the Knudsen number in the current work is estimated in the flow at $Kn = 0.0025 \pm 0.0005$ in the free-stream, and is within this range for each of the enthalpy conditions from runs R4-R6. Gardner and Agarwal [2019] began observing post-shock trans-rotational non-equilibrium at $Kn = 0.002$, with more deviation between the translational and rotational temperatures as the Knudsen number increases. Unfortunately, the current study does not include enthalpy runs at higher Knudsen numbers, so this effect cannot be thoroughly investigated. However, due to the matching trends between the current work and Gardner and Agarwal [2019], it is possible the Knudsen number of the current experiments are larger than what has been calculated. The work by Gardner and Agarwal [2019] was the only prior study found in the literature that has investigated this form of thermal non-equilibrium in front of a flat-faced blunt body in a hypersonic flow.

Figure 8.8 shows the average temperature in the free-stream and post-shock regions over each enthalpy condition. The free-stream data is difficult to interpret completely, as the data points at the 8.4 MJ/kg enthalpy condition are within range of the uncertainty bars. Overall, the temperatures, when considered together, appear to increase slightly with enthalpy, which is an expected result. In the post-shock region, the rotational temperature consistently decreases as enthalpy increases. The translational temperature has a local maxima at the 6.9 MJ/kg enthalpy condition, then decreases at the 8.4 MJ/kg enthalpy condition. These were unexpected results, as the temperatures were expected to increase in the post-shock as enthalpy increased. A possible explanation for these results are due to the vibrational mode being frozen at a higher energy as enthalpy increases, therefore decreasing the energy available to other modes. However, the current work cannot quantify the

vibrational temperature, and therefore cannot test this theory. Overall, there is no clear explanation from the current data for the decreasing temperature trend with enthalpy in the post-shock region.

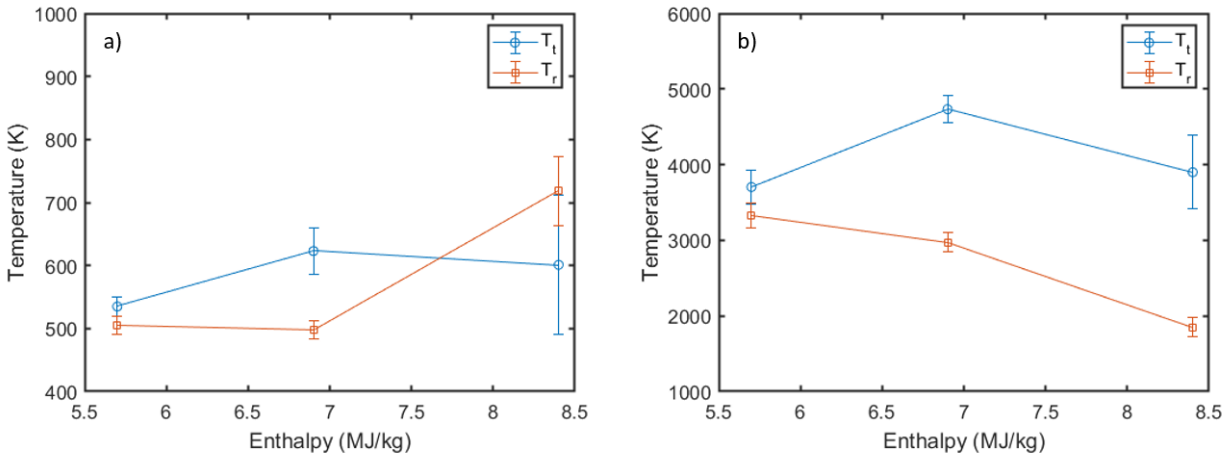

Figure 8.8: Averaged temperature for each enthalpy condition in the a) free-stream (x = 1 mm to x = 5 mm) and b) post-shock (x = 8 mm to x = 15 mm) regions.

Figure 8.9 shows raw spectral NO-PLIF data from two transitions at each enthalpy condition. As described in Chapter 3, as rotational temperature increases, higher J'' states are populated, as governed by the Boltzmann fraction term. As the enthalpy condition increases, it is expected that the rotational temperature in the post-shock would also increase, however the opposite is observed in Figure 8.8. The J'' = 33.5 transition decreases in amplitude as the enthalpy condition is increased, indicating the post-shock region is cooling. This observation fundamentally supports the rotational temperature results reported in the current work. If the post-shock region was increasing in temperature with enthalpy, the opposite trend would be observable in the spectra. Overall, based on the spectral data presented in Figure 8.9, the raw data indicates the post-shock rotational temperature does decrease as enthalpy increases, which supports the SPT results reported in Figure 8.6.

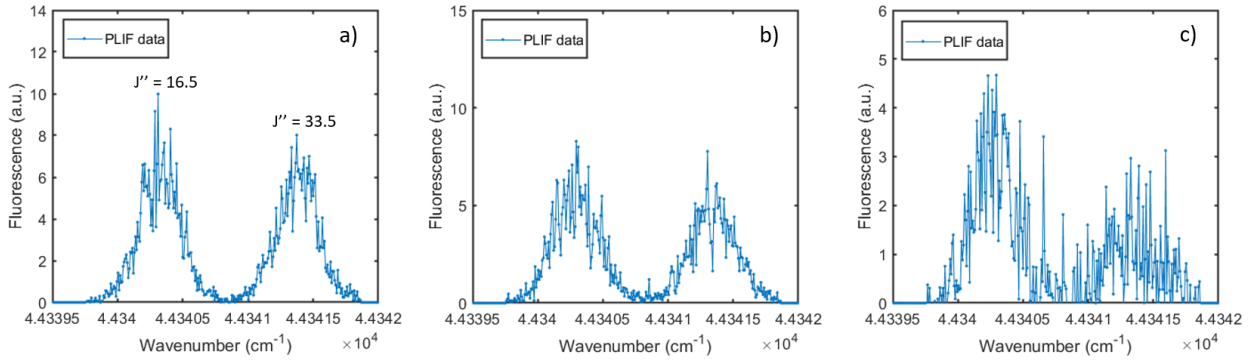

Figure 8.9: Raw NO-PLIF spectral data of the $J'' = 16.5$ and $J'' = 33.5$ transitions in the post-shock region ($x = 4$ mm) at each enthalpy condition: a) R4 - 5.7 MJ/kg, b) R5 - 6.9 MJ/kg, c) R6 - 8.4 MJ/kg.

The bow shock can be seen in Figure 8.6(a-c), and shows signs of blurring as the enthalpy condition increases. Blurring is observed as a decrease in slope near the shock temperature rise ($x \approx 6$ mm). This blurring may be due to shock unsteadiness as reported in prior studies in the HyMETS facility [Danehy et al., 2012], however it was not observed that unsteadiness significantly changed with enthalpy condition in the current work. An alternate explanation is that the blurring of the shock may be due to molecular effects beginning to manifest in the flow, as also predicted by Gardner and Agarwal [2019]. Figure 2.6 from Gardner and Agarwal [2019] shows as the Knudsen number increases, the bow shock begins to blur and become less discontinuous. However, in the current work, free-stream Knudsen number does not change significantly across each enthalpy condition. Although multiple explanations for this phenomena are plausible, the exact cause of the shock blurring trend with increasing enthalpy is unknown based on the current data.

The current work shows evidence of a hot shear layer (a shear layer temperature that is higher than the free-stream temperature) forming at approximately 40 mm from the centerline of the flow, which is reflected in both translational and rotational temperature measurements. This result also supports the observation from the DSV results that the nozzle is underexpanded, and is expanding into the free-stream, forming a shear-layer on the edges of the core flow. However, previous computational results reported by Brune et al. [2019] predict temperature in the shear-layer region to be cooler than the free-stream temperature (CFD temperature data can be found in McDougall

et al. [2020b]). The reason for this discrepancy between the current work and these previous computational results is not known. However, the current work identifies a hot shear layer in all temperature measurement runs (Runs R2-R6) across multiple spectral ranges and laser energies, and therefore there is high confidence in the measurement of a hot shear layer region. Therefore, this temperature data can be valuable for the validation of CFD models applied to the HyMETS facility, specifically in the viscous modelling required in the shear layer.

The DBT method measures a significantly higher temperature in the shear layer downstream. This measurement is likely due to spectra fitting problems in the shear layer due to flow instability over the duration of scanning the transition. During the experimental runs in the current work, the shear layer location fluctuates significantly, and is more pronounced the further downstream from the nozzle that the measurement is taken. This fluctuation introduces a large uncertainty into the spectra due to the large change in temperature in the shear-layer when compared to the free-stream flow. Additionally, since the DBT measurement is based on a single transition, and therefore a single spectral fit, the fit can be significantly affected by shear-layer unsteadiness. The radial velocity in this region is also significant, therefore if the shear-layer is fluctuating into the free-stream, it can cause broadening to occur in the regions immediately surrounding the shear-layer due to the spectral shift in line center. The NLLS spectral fitting process was examined for local minima errors, however the fit had achieved a global minima at the reported temperature.

The NLLS fit uncertainty reported in the rotational temperature measurements is homogeneous across regions of the flow. Since the SPT method uses multiple spectral lines, the method is more time-averaged than, for example, the DSV measurement. Individual fluctuations due to unsteadiness do not affect the SPT uncertainty as drastically as the DSV measurement. However, SPT is affected by the regional unsteadiness level. Therefore, in the post-shock, the uncertainty in the rotational temperature measurement significantly increases when compared to the free-stream, but there is very little variation in associated uncertainty between local spatial locations within the post-shock region. The DBT NLLS fit uncertainty, while overall of a larger magnitude, is similarly

insensitive to local spatial unsteadiness variations. This is likely due to the width of the spectra being dependent on more data from the spectral line, unlike DSV where few spectral peak values can influence the fit uncertainty of the line center to a large degree.

8.3 Simulations

This section details the results produced by the quasi-1D three-temperature finite difference solver created in the current work, ARC1D. The simulated results show the translational, rotational and vibrational temperatures through the nozzle of the HyMETs facility. ARC1D was used to simulate the flow in the nozzle at the three enthalpy conditions targeted in the current study. The plenum (reservoir) temperature for each condition was found by interpolating from the bulk enthalpy experimental measurement, as has been done previously in the literature [Johansen et al., 2016]. The results are shown on Figure 8.10. ARC1D is also used to simulate four experiments detailed in the literature completed in the HyMETS facility, which are shown in Figure 8.11. Finally, ARC1D is used to produce a non-equilibrium map for a range of normal operating conditions of the facility, which is presented in Figure 8.12.

The goal of the ARC1D analysis was to evaluate the thermodynamics of the flow in the nozzle, where NO-PLIF is optically inaccessible, and to particularly determine if the flow was in thermodynamic non-equilibrium while leaving the nozzle into the free-stream of the facility. The results in Figure 8.10 show the vibrational temperature freezing at a high temperature early in the nozzle geometry, as expected from a previous computational study by Brune et al. [2019]. The vibrational temperature is frozen much higher than the translational and rotational temperatures, and enters the free-stream of the facility in this state. In the cases presented in Figure 8.10, the translational and rotational temperatures appear to remain in equilibrium as the flow enters the facility. These results appear to predict higher free-stream temperatures (T_r = 760 K, T_t = 724 K) for the 5.7 MJ/kg enthalpy condition when compared to the experimental SPT results (approximately T_r = 500 K, T_t = 520 K). However, since the nozzle is underexpanded (as confirmed by velocimetry and ther-

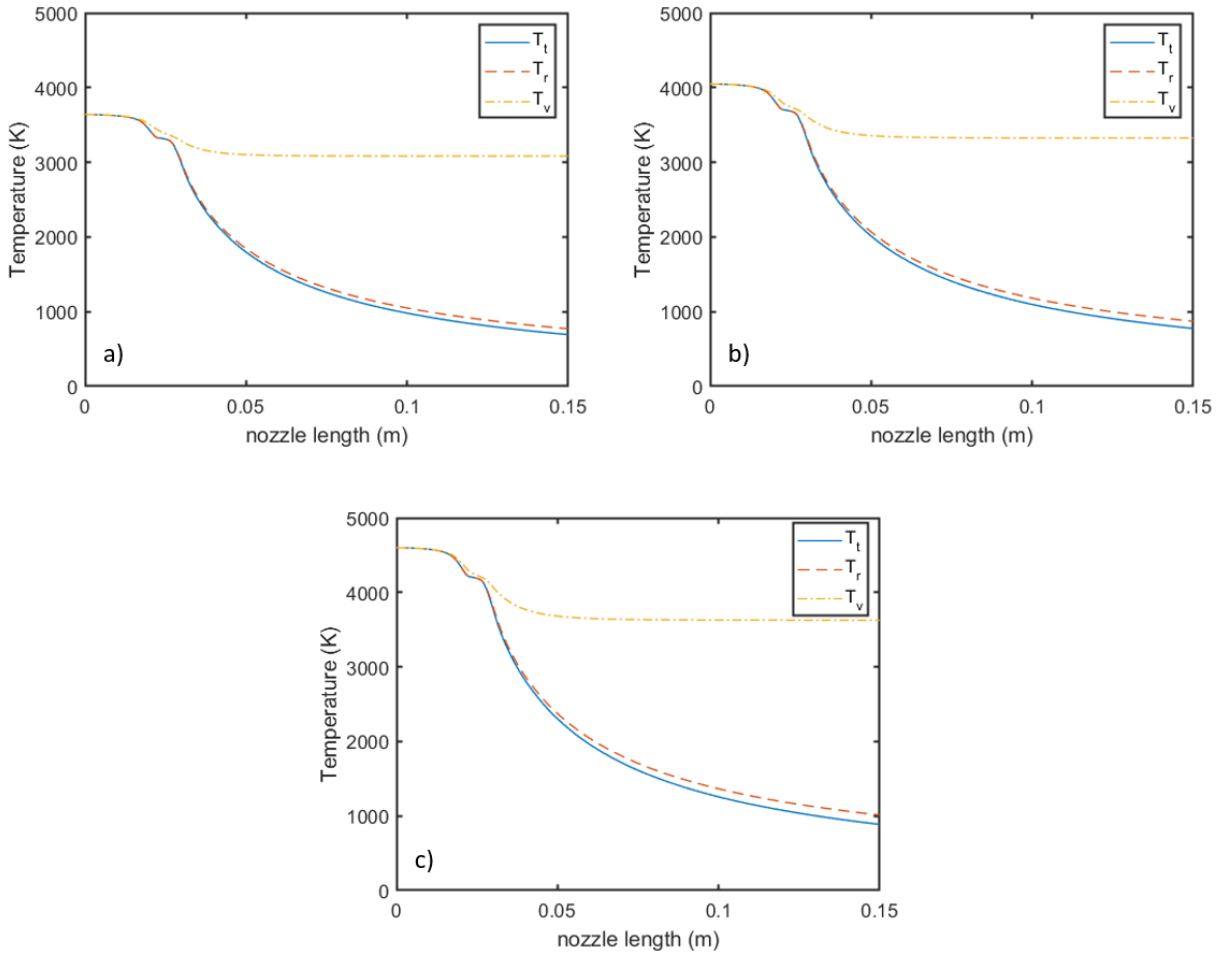

Figure 8.10: ARC1D results for the enthalpy conditions in the current work: a) 5.7 MJ/kg, b) 6.9 MJ/kg, c) 8.4 MJ/kg.

mometry results) the flow continues to expand into the free-stream of the facility, and it is likely the temperature decreases from the nozzle exit to the NO-PLIF imaging region. Note the ARC1D simulations assume perfectly expanded flow. Additionally, the nozzle is underexpanded at all enthalpy conditions, as indicated by the velocimetry measurements, and therefore the same effect occurs at the 6.9 MJ/kg and 8.4 MJ/kg conditions when comparing ARC1D to the experimental data. Overall, these results appear similar to the experimental data, and predict that the translational and rotational temperatures are in equilibrium in the free-stream for each of the enthalpy conditions considered in the current work.

ARC1D was also used to simulate four other experiments completed in previous studies. The studies conducted experiments at a range of enthalpies, but at higher arc currents and lower mass flow rates, resulting in a less dense flow theoretically more likely to produce non-equilibrium effects. This analysis was completed to determine if the HyMETS facility is capable of producing trans-rotational non-equilibrium in the nozzle if the mass flow rate of injected gasses was decreased, and if this phenomenon would explain some observations in those studies. ARC1D results for these previous studies are shown in Figure 8.11, and are explained below.

A flow visualization study by Inman et al. [2013] completed an experiment in the HyMETS facility at 15.4 MJ/kg at a mass flow rate of 102 SLPM. The matched ARC1D results for this condition shown in Figure 8.11a indicate trans-rotational non-equilibrium is occurring in the flow as it exits the nozzle (T_r = 1747 K, T_t = 1064 K, Kn = 0.017). This study noted that tuning the facility to enthalpies below 10 MJ/kg maximized the NO fluorescence for flow visualization and quantitative measurements, due to lack of NO fluorescence observed above that enthalpy level. The line being examined in this work was a $J'' = 6.5$ transition, which if probed under the conditions predicted by ARC1D in the free-stream (1747 K) has a low ground state population at high temperatures, therefore emitting little fluorescence. The thermal non-equilibrium predicted by ARC1D may provide an explanation for the low fluorescence signal produced in this study.

Another study completed in the HyMETS arc-jet by Johansen et al. [2016] completed exper-

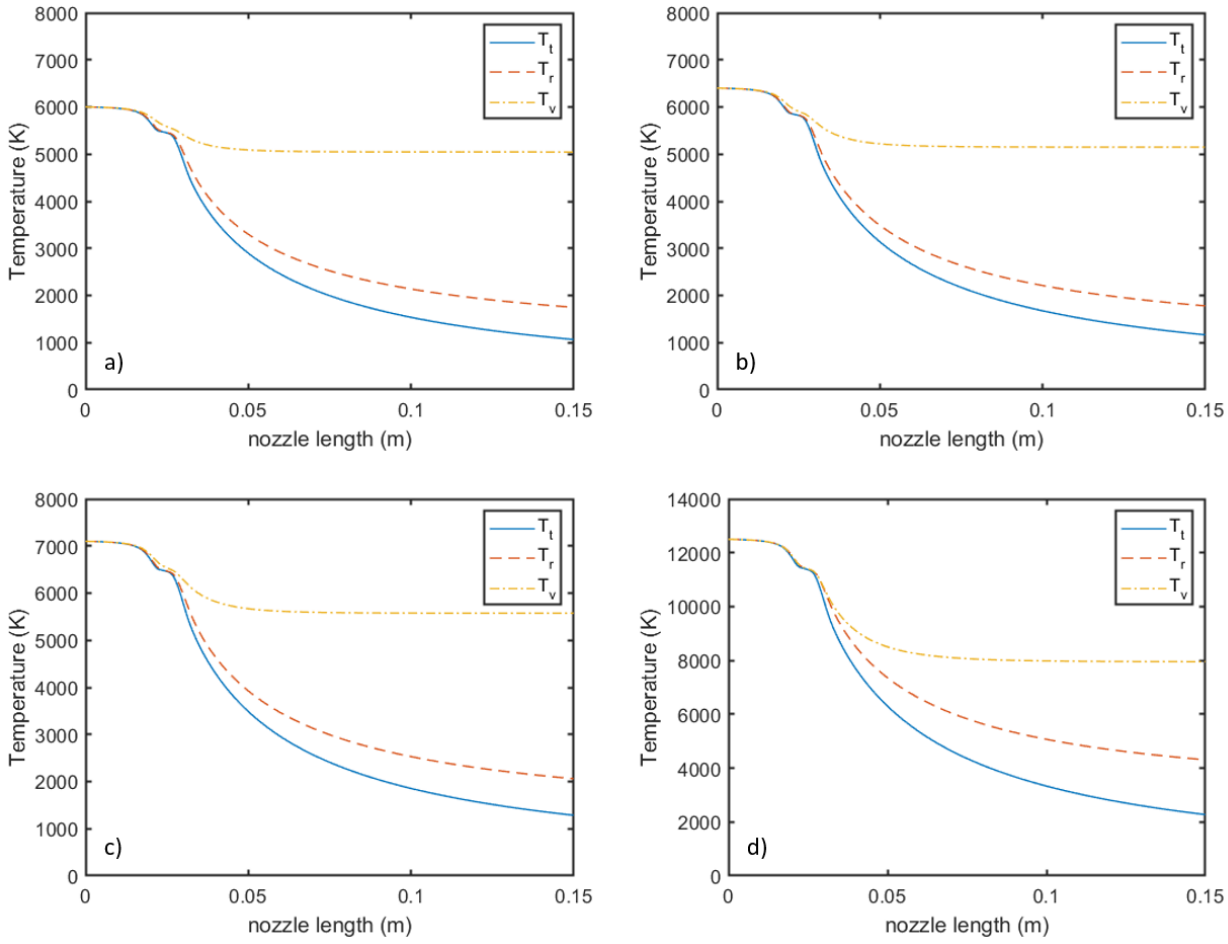

Figure 8.11: ARC1D results simulating four other studies that have completed studies at the HyMETS arc-jet: a) 15.4 MJ/kg experiment by Inman et al. [2013], b) 18.5 MJ/kg experiment by Johansen et al. [2016], c) 27.5 MJ/kg experiment by Brune et al. [2019], d) 45 MJ/kg experiment by Danehy et al. [2012].

iments at a range of enthalpies, with the highest enthalpy run of 18.5 MJ/kg at a mass flow rate of 129 SLPM. The matched ARC1D results for this condition are shown in Figure 8.11b. These results also indicate trans-rotational non-equilibrium is occurring in the flow as it exits the nozzle (T_r = 1778 K, T_t = 1164 K, Kn = 0.014). That study used a simultaneous NO/O-atom LIF technique and compared the results to calculations of the relative fluorescence based on an equilibrium assumption through the nozzle, as shown in Figure 2.2. The disagreement between simulated O-LIF and experimental O-LIF becomes large for run conditions that are predicted by ARC1D to be in rotational nonequilibrium. Although the O-atom species does not have rotational or vibrational modes, it is part of the "translational pool" of energy and therefore if energy is frozen in rotational modes of other molecules, and can affect the O-atom translational temperature. Additionally, results from Johansen et al. [2016] at large enthalpies indicate the NO equilibrium theory deviates from the experimental measurements as well. Therefore, a correction for trans-rotational non-equilibrium may improve agreement between the theory presented and the experimental results in this study.

A computational study completed by Brune et al. [2019] performed a probe-based experiment and a computational study at an enthalpy of 27.4 MJ/kg and mass flow rate of 165 SLPM. The matched ARC1D results for this condition are shown in Figure 8.11c. The ARC1D simulations of this experiment predict trans-rotational non-equilibrium at the nozzle exit (T_r = 2060 K, T_t = 1285 K, Kn = 0.13). The computational study simulated flow using a two-temperature model, assuming the translational and rotational temperatures were in equilibrium. The purpose of this computational study was to evaluate the heat transfer to the surface of a slug calorimeter. As the flow crosses the bow shock and reaches the surface of the calorimeter, the flow decreases in velocity and increases in density, therefore likely reaching thermodynamic equilibrium due to increased molecular collisions. Calorimeter data was used to validate the model used in the simulations. However, the heat flux data is accurate regardless of if a two or three temperature model is used, since the total energy content of the flow does not change in a non-equilibrium flow, it is just

partitioned in the translational, rotational and vibrational modes. Due to this, non-equilibrium could not have been detected with the experimental probe-based methodology used.

Another study completed in the HyMETS arc-jet by Danehy et al. [2012] performed an experiment at 45 MJ/kg enthalpy and a mass flow rate of 155 SLPM. As shown in Figure 8.11d, ARC1D predicts significant trans-rotational non-equilibrium at the nozzle exit (T_r = 4309 K, T_t = 2285 K, Kn = 0.12). The study gathered emission spectroscopy data from the HyMETs facility over a large range of test conditions. It was observed in this study that the bow shock was blurred due to bow shock fluctuations, however the blurring effect is much more extreme in Danehy et al. [2012] than in the current study for similar enthalpy conditions. The shock is blurred across approximately 4 mm in Danehy et al. [2012] compared to approximately 2 mm in the current study. Instead of shock blurring due to unsteadiness, this may indicate the shockwave is forming in rarefied flow, where the shock is blurred out due to molecular effects. This blurring effect is also seen in the results presented by Gardner and Agarwal [2019] in Figure 2.6. These observations from the experiment, while also considering results from ARC1D and Gardner and Agarwal [2019], indicate trans-rotational non-equilibrium was likely occurring in these experimental conditions.

Comparing other experimental runs from these works to the present study, the arc current and mass flow rate conditions in the present work produced lower bulk enthalpy flows when compared to previous studies completed at identical arc current and mass flow conditions. Inman et al. [2013] and Johansen et al. [2016] both completed experiments in the HyMETS facility at bulk enthalpies of 6.5 and 6.7 MJ/kg flows, respectively, for 100 A arc current and 400 SLPM mass flow rate. The present study, which matched the arc current and mass flow rate conditions of those prior studies, produced a bulk enthalpy of 5.7 MJ/kg. This is approximately a 15% lower enthalpy than the previous studies. This result indicates the energy balance has changed on the arc generator. This observation also impacts the ability of computational studies to match enthalpy conditions during validation. Due to this unknown error, the ARC1D results presented in this section may not reflect the exact enthalpy condition of each study.

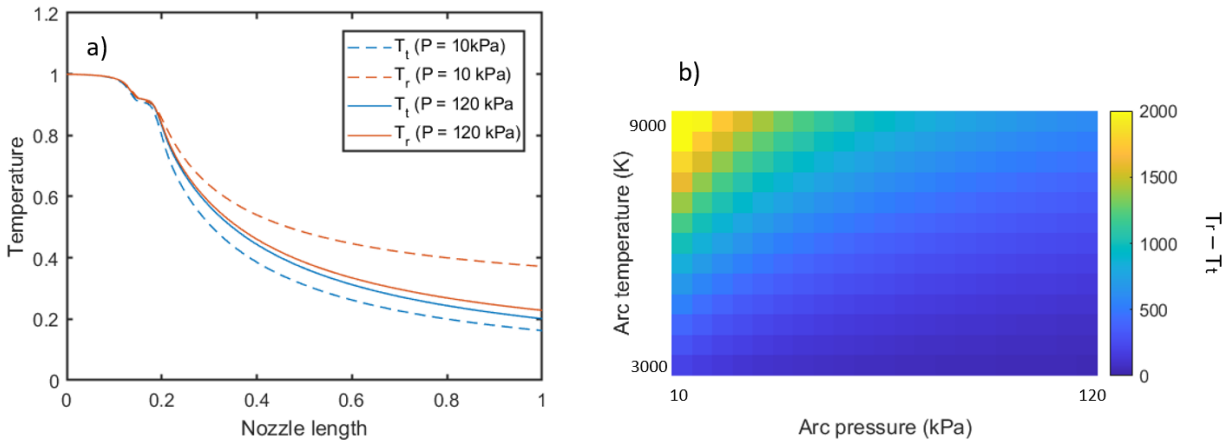

Figure 8.12: Non-equilibrium effects due to reservoir temperature & pressure: a) Constant reservoir temperature (T = 5000 K) while varying reservoir pressure, and b) a colourmap showing the difference in nozzle exit rotational & translational temperature when varying reservoir temperature and pressure.

The four studies examined each operated at low mass flow rate conditions compared to the current work. Fundamentally, the properties that affect the mass flow rate and enthalpy of the flow are the reservoir (or plenum/arc) temperature and pressure. Figure 8.12a shows the effect of changing the reservoir pressure while keeping the temperature constant. As shown, the reservoir pressure has a large effect on the trans-rotational non-equilibrium occurring in the flow, due to the relation with mass flow rate through the nozzle. This observation can be generalized across a range of reservoir temperatures and pressures, as shown in Figure 8.12b. This figure illustrates a range of normal operating conditions of the HyMETS facility, and which conditions produce the largest thermal non-equilibrium at the nozzle exit. As shown, a combination of low pressure and high temperature in the reservoir lead to the largest difference in rotational and translational temperatures at the nozzle exit. These results can be used to design studies either to maximize or minimize thermal non-equilibrium in the HyMETS arc-jet by first calculating mass flow rate and enthalpy from the given reservoir temperature and pressure, while setting the facility to the required configuration.

Chapter 9

CONCLUSIONS & RECOMMENDATIONS

9.1 Conclusions

In the present work, nitric oxide planar laser-induced fluorescence was applied to the Hypersonic Materials Environmental Test System arc-jet facility at three enthalpy conditions to characterize aerothermodynamic properties of the flow around a flat-faced blunt body model. A series of experimental design considerations were made to tailor the planar laser-induced fluorescence imaging technique to the arc-jet environment, such as using an off-laser image to subtract luminosity from the flow. Image processing steps were completed to minimize sources of uncertainty and remove sources of error. Initial studies were completed to minimize facility unsteadiness, correct for laser saturation effects, and measure the spectral linewidth of the laser. The facility free-stream unsteadiness was reduced by approximately 40% by optimizing the gas injection configuration of the arc generator. The saturation study was completed on a pixel-by-pixel basis by mapping the laser profile to the experimental image to produce an accurate saturation value for use in the rotational temperature measurement. This saturation study methodology represents a significant increase in complexity from saturation quantification in the literature, and was observed to be accurate based on the high quality spectral fits from the rotational temperature measurement. A high spectral resolution experiment in a gas cell was completed to accurately measure the linewidth of the laser, which was then subsequently used in the translational temperature measurement.

Radial velocimetry was performed by measuring the Doppler shift of a spectral line from the laser-induced fluorescence spectra. The velocimetry results showed the flow continuing to expand in the free-stream of the test section, indicating that the arc-jet nozzle is underexpanded during operation. Additionally, it was determined that the radial velocity field is relatively insensitive to the enthalpy conditions tested in the current work. Finally, radial velocities were measured up to

750 m/s in the post-shock region, representing the first velocimetry measurements in the post-shock in this facility.

Rotational thermometry was performed by modelling the rotational temperature dependence of the Boltzmann fraction, and fitting the model to multiple spectral lines. The method produced repeatable results over multiple laser energies, spectral ranges, scan step sizes, and temperature ranges, achieving agreement within 52 K in the free-stream and shear-layer flow regions. The translational temperature was determined by measuring the Doppler broadening of a spectral line. The rotational and translational temperature measurements reported are the first spatially-resolved temperature measurements in this facility. When comparing the rotational and translational temperature measurements in the post-shock region near the specimen, trans-rotational thermal non-equilibrium was observed. These measurements are the first experimental evidence of trans-rotational non-equilibrium in this arc-jet facility. The results are also supported by computational results found in the literature for a similar blunt body flow. These results also highlight that the facility used in the current work is ideal for studying thermal non-equilibrium, since the arc-jet can easily generate these effects while running within normal operating conditions.

A three-temperature finite difference solver was created to investigate the effect of input parameters such as arc current and mass flow rate on the flow within the nozzle. The solver is also coupled with a chemical kinetics and thermodynamics solver, Cantera, to determine the equilibrium species mixture in the reservoir. The results produced by this solver generally reflected the measurements from the experiments, where the translational and rotational temperatures are predicted to be in equilibrium in the free-stream of the facility. The solver was also used to simulate previous studies completed in this facility and found that trans-rotational non-equilibrium is predicted to occur in many common operating conditions at low mass flow rates. This is the first computational evidence of trans-rotational non-equilibrium occurring in this arc-jet. Finally, a range of conditions covering common operating conditions of the facility were simulated to produce a trans-rotational non-equilibrium prediction map for the free-stream of the arc-jet.

9.2 Recommendations

A number of recommendations are outlined in this section that can be applied to future arc-jet experimental and computational studies.

The experimental design methodology described in the current work can be improved. Firstly, free-stream absorption effects should be investigated further due to the fluorescence signal discrepancies observed between the present and past works. The current work observed an increase in fluorescence as the laser sheet propagates through the flow, while a prior work observed a decrease in fluorescence. This observation indicated the laser sheet may not be perfectly collimated in the current work, where the laser sheet could be becoming thicker as it propagates across the imaging region, illuminating a large volume of nitric oxide at a lower level of saturation, therefore producing a larger signal amplitude. Correcting for absorption by assessing the collimation of the laser sheet, a systematic error can be removed that has an unknown effect on the current work. Secondly, repeatability studies while holding the laser energy, spectral range, spectral scan step size, and enthalpy condition constant would allow further quantification of the uncertainty run-over-run for each quantitative measurement. A comprehensive data set assessing each of these variables individually would allow for measurement uncertainty to be more thoroughly quantified. In general, repeatability experiments should be completed for all quantitative analysis to properly determine the associated uncertainty. Thirdly, the spectral scans in the current work could be adjusted such that multiple data points are acquired at each laser wavelength for a single run, which would reduce the impact of flow unsteadiness on the quantitative measurements. Finally, the energy balance on the arc-generator should be assessed due to the varied enthalpies produced over multiple studies using identical arc current and mass flow rate settings. This assessment would allow future computational or experimental studies to closely match flow conditions to studies from the literature.

The unsteadiness minimization study used fluctuations in the NO-PLIF signal as an indicator for unsteadiness in the flow, however other less complex imaging methods could be used to achieve

the same measurement, such as schlieren photography. Alternatively, this study could be completed with probe-based techniques instead of imaging techniques, as unsteadiness could be measured by pressure fluctuations from the pitot probe already available in the arcjet facility. A single run is analyzed for the unsteadiness minimization study, while changing the nozzle injection "on the fly" as the facility is operating. This methodology could be improved by dedicating an experimental run for each injection configuration, which would hold the configuration constant over the duration of the run. Additional improvements to the methodology include increasing the resolution of the study (i.e. changing injection by 1% increments rather than 5-10% increments), and inclusion of repeatability studies to determine if the unsteadiness improvement observed in the current work is consistently detected.

The saturation study quantified the saturation term which was used in the rotational temperature measurement, but can be improved in a number of ways. Firstly, the laser energy profile in the current work is quite heterogeneous, which is not ideal for saturation analysis. The ideal spatial profile is a box function with a consistent laser irradiance across the thickness of the beam. By applying the current saturation study methodology to a more refined laser profile, the measurement of the saturation value would become more accurate. Additionally, single, non-overlapped transitions should be targeted to avoid additional uncertainty propagating into the measurement due to the imperfect overlap of transitions. Finally, the experimental run could be extended to gather more data, which would reduce the possibility of error or uncertainty being introduced into the measurement due to random fluctuations from flow unsteadiness.

The gas cell study achieved a high degree of accuracy and precision in the current work, but can be improved in future studies to better quantify sources of uncertainty. The transition group chosen consisted of two overlapped transitions that are off-set slightly in the spectral domain. This off-set is accounted for in the current work, but introduces a difficult to quantify source of uncertainty into the laser linewidth measurement. Using a single transition in future studies would remove this source of uncertainty and increase the precision of the measurement. Secondly, the

lineshape is approximated in the current work as a Gaussian, however the spectral lineshape is truly a Voigt profile, as described in Chapter 3. The laser spectral profile is a Lorentzian lineshape, which is then convolved with a Gaussian thermal (Doppler) broadened lineshape as the laser is scanned spectrally across the transition. Therefore, a future study could de-convolve the Gaussian thermal lineshape of the spectra to produce the Lorentzian laser lineshape. Then, when measuring translational temperature from Doppler broadening, the laser lineshape can be de-convolved from the lineshape of the spectra, producing the Doppler-broadened Gaussian absorption lineshape. This proposed method would require a higher resolution spectral scan than what was acquired in the current work, and would need to be validated in a controlled experiment prior to use in a complex flow like an arc-jet.

Future studies can improve the velocimetry methodology used in the current work. Firstly, multiple, non-overlapped, isolated transitions should be targeted in each run to reduce the dependence on a single transition. This improvement would significantly reduce the uncertainty in the line center location and therefore the velocity measurement. Secondly, future studies could vary the mass flow rate of injection gases in the facility to determine the effect on the radial velocity. The current work varied the arc current, which affects the bulk enthalpy of the flow, but held mass flow rate constant for each run.

In future work, the trans-rotational non-equilibrium detected in the temperature measurements of the current study should also be investigated further to comprehensively quantify this effect. By completing experiments at lower flow rates, as has been done in previous studies, the non-equilibrium hypothesis can be evaluated in both the free-stream and post-shock regions. Additionally, future studies should quantify the vibrational temperature by targeting a set of vibrational lines and applying a similar thermometry analysis to the spectra. This analysis would include modelling the vibrational Boltzmann fraction dependence to determine temperature from multiple spectral lines. The addition of vibrational thermometry would allow for a complete measurement of the thermodynamic state of the flow within the arc-jet.

The finite difference three-temperature nozzle flow solver described in the current work can be extended to model a blunt body in the flow path. This addition was not attempted in the current work due to the significant complexity in the post-shock region due to chemistry effects becoming a factor. Therefore, a multi-species reactions model needs to be used in the post-shock region to capture the physics occurring. Additionally, radiation modelling may be necessary due to the natural emissions observed in the shock layer. These added complexities to the modelling would also be difficult to verify and validate, but would be useful if the solution accurately reflected the physics occurring in the post-shock.

Bibliography

K.-i. Abe, T. Kameyama, H. Kihara, M. Nishida, K. Ito, and H. Tanno. Computation and experiment of a nonequilibrium nozzle flow of arc-heated air. *Journal of thermophysics and heat transfer*, 19(4):428–434, 2005.

R. Abernethy, R. Benedict, and R. Dowdell. Asme measurement uncertainty. 1985.

J. D. Anderson Jr. A time-dependent analysis for vibrational and chemical nonequilibrium nozzle flows. *AIAA Journal*, 8(3):545–550, 1970.

J. D. Anderson Jr. *Hypersonic and high-temperature gas dynamics*. American Institute of Aeronautics and Astronautics, 2006.

C. Arisman, C. T. Johansen, W. Galuppo, and A. McPhail. Nitric oxide chemistry effects in hypersonic boundary layers. In *43rd AIAA Fluid Dynamics Conference*, page 3104, 2013.

S. C. Bailey, D. Bauer, F. Panerai, S. C. Splinter, P. M. Danehy, J. M. Hardy, and A. Martin. Experimental analysis of spallation particle trajectories in an arc-jet environment. *Experimental Thermal and Fluid Science*, 93:319–325, 2018.

P. F. Barker, A. M. Thomas, T. J. McIntyre, and H. Rubinsztein-Dunlop. Velocimetry and thermometry of supersonic flow around a cylindrical body. *AIAA journal*, 36(6):1055–1060, 1998.

B. F. Bathel, P. M. Danehy, J. A. Inman, S. B. Jones, C. B. Ivey, and C. P. Goyne. Velocity profile measurements in hypersonic flows using sequentially imaged fluorescence-based molecular tagging. *AIAA journal*, 49(9):1883–1896, 2011.

W. G. Bessler and C. Schulz. Quantitative multi-line no-lif temperature imaging. *Applied Physics B*, 78(5):519–533, 2004.

H. Blackwell, C. Scott, S. Arepalli, H. Blackwell, C. Scott, and S. Arepalli. Measured nonequilibrium temperatures in a blunt body shock layer in arc jet nitrogen flow. In *32nd Thermophysics Conference*, page 2522, 1997.

D. Bose, J. A. Santos, E. Rodriguez, T. R. White, and M. Mahzari. Mars science laboratory heat shield instrumentation and arc jet characterization. In *44th AIAA Thermophysics Conference*, page 2778, 2013.

A. J. Brune, W. E. Bruce III, D. E. Glass, and S. C. Splinter. Computational predictions of the hypersonic material environmental test system arcjet facility. *Journal of Thermophysics and Heat Transfer*, 33(1):199–209, 2019.

A. Calomino, W. Bruce, P. Gage, D. Horn, M. Mastaler, D. Rigali, J. Robey, L. Voss, J. Wahlberg, and C. Williams. Evaluation of the nasa arc jet capabilities to support mission requirements. *NASA technical report*, 2010.

P. Danehy, D. Hires, C. Johansen, B. Bathel, S. Jones, J. Gragg, and S. Splinter. Quantitative spectral radiance measurements in the hymets arc jet. In *50th AIAA Aerospace Sciences Meeting including the New Horizons Forum and Aerospace Exposition*, page 856, 2012.

P. M. Danehy, B. F. Bathel, C. T. Johansen, M. Winter, S. O'Byrne, and A. D. Cutler. Molecular-based optical diagnostics for hypersonic nonequilibrium flows. *Hypersonic Nonequilibrium Flows: Fundamentals and Recent Advances*, pages 343–470, 2015.

R. S. Davuluri, H. Zhang, and A. Martin. Numerical study of spallation phenomenon in an arc-jet environment. *Journal of Thermophysics and Heat Transfer*, 30(1):32–41, 2016.

W. Demtröder. *Laser spectroscopy: basic concepts and instrumentation*. Springer Science & Business Media, 2013.

J. B. Dence. Heat capacity and the equipartition theorem. *Journal of Chemical Education*, 49(12): 798, 1972.

M. D. Di Rosa. High Resolution Line Shape Spectroscopy of Transitions in the Gamma Bands of Nitric Oxide. 1996.

Ü. Düzel, O. M. Schroeder, H. Zhang, and A. Martin. Numerical simulation of an arc jet test section. *Journal of Thermophysics and Heat Transfer*, pages 1–11, 2019.

K. Edquist, A. Dyakonov, M. Wright, and C. Tang. Aerothermodynamic design of the mars science laboratory heatshield. In *41st AIAA Thermophysics Conference*, page 4075, 2009.

D. Ellington. Approximate method for hypersonic nonequilibrium blunt body airflows. *AIAA Journal*, 1(8):1901–1904, 1963.

R. Engleman. Beta and Gamma Systems of Nitric Oxide. Technical report, Los Alamos Scientific Laboratory, 1970.

S. T. Gardner and R. K. Agarwal. Effects of rarefaction and thermal non-equilibrium on a blunt body and a bicone in hypersonic flow and their shape optimization for reducing both drag and heat transfer. In *AIP Conference Proceedings*, volume 2132, 2019.

T. Gokcen. Effects of freestream nonequilibrium on convective heat transfer to a blunt body. *Journal of thermophysics and heat transfer*, 10(2):234–241, 1996.

D. G. Goodwin, H. K. Moffat, and R. L. Speth. Cantera: An object-oriented software toolkit for chemical kinetics, thermodynamics, and transport processes. *Caltech, Pasadena, CA*, 124, 2009.

V. Gopal, D. Palmquist, L. Maddalena, L. E. Dogariu, and A. Dogariu. Fleet velocimetry measurements in the onr-uta arc-jet wind tunnel. *Experiments in Fluids*, 62(10):1–17, 2021.

J. Grinstead, D. Stewart, and C. Smith. High enthalpy test methodologies for thermal protection systems development at nasa ames research center. In *AIAA/CIRA 13th international space planes and hypersonics systems and technologies conference*, page 3326, 2005.

J. Grinstead, B. Porter, and E. Carballo. Flow property measurements using laser-induced fluorescence in the nasa ames interaction heating facility arc jet. In *49th AIAA Aerospace Sciences Meeting including the New Horizons Forum and Aerospace Exposition*, page 1091, 2011.

J. H. Grinstead, D. M. Driver, and G. A. Raiche. Radial profiles of arcjet flow properties measured with laser-induced fluorescence of atomic nitrogen. In *20th International Congress on Instrumentation in Aerospace Simulation Facilities.*, pages 278–286, 2003.

E. P. Hartman. *Adventures in Research: A History of Ames Research Center, 1940-1965*, volume 4302. Scientific and Technical Information Division, 1970.

J. Inman, P. Danehy, B. Bathel, and R. Nowak. Laser-induced fluorescence velocity measurements in supersonic underexpanded impinging jets. In *48th AIAA Aerospace Sciences Meeting Including the New Horizons Forum and Aerospace Exposition*, page 1438, 2010.

J. A. Inman, B. F. Bathel, C. T. Johansen, P. M. Danehy, S. B. Jones, J. G. Gragg, and S. C. Splinter. Nitric-oxide planar laser-induced fluorescence measurements in the hypersonic materials environmental test system. *AIAA journal*, 51(10):2365–2379, 2013.

C. Ivey, P. Danehy, B. Bathel, A. Dyakonov, J. Inman, and S. Jones. Comparison of plif and cfd results for the orion cev rcs jets. In *49th AIAA Aerospace Sciences Meeting including the New Horizons Forum and Aerospace Exposition*, page 713, 2011.

C. T. Johansen, D. A. Lincoln, B. F. Bathel, J. A. Inman, and P. M. Danehy. Simultaneous nitric oxide/atomic oxygen laser-induced fluorescence in an arcjet facility. *Journal of Thermophysics and Heat Transfer*, 30(4):912–918, 2016.

S.-W. Kang. Nonequilibrium, ionized, hypersonic flow over a blunt body at low reynolds number. *AIAA Journal*, 8(7):1263–1270, 1970.

T. P. Kaseman, L. M. Le Page, S. B. O'Byrne, and S. L. Gai. Visualization and thermometry in

hypersonic wedge and leading-edge separated flows. In *55th AIAA aerospace sciences meeting*, 2017.

E. D. Katzen and G. E. Kaattari. Inviscid hypersonic flow around blunt bodies. *AIAA Journal*, 3 (7):1230–1237, 1965.

M. Kirschner, A. S. Pudsey, F. Koroll, T. Sander, and C. Mundt. Laser-induced fluorescence investigations for temperature measurements in a carbon dioxide flow. *Journal of Thermophysics and Heat Transfer*, 32(1):216–225, 2018.

G. Kychakoff, R. D. Howe, R. K. Hanson, and J. C. McDaniel. Quantitative visualization of combustion species in a plane. *Applied Optics*, 21:3225–3226, 1982.

L. Landau and E. Teller. Physik. zeits. sowjetunion. 1936.

J. G. Liebeskind, R. K. Hanson, and M. A. Cappelli. Laser-induced fluorescence diagnostic for temperature and velocity measurements in a hydrogen arcjet plume. *Applied optics*, 32(30): 6117–6127, 1993.

R. W. MacCormack. The effect of viscosity in hypervelocity impact cratering. *Journal of spacecraft and rockets*, 40(5):757–763, 2003.

C. C. McDougall, W. S. Hinman, C. T. Johansen, B. F. Bathel, J. A. Inman, and P. M. Danehy. Nitric oxide planar laser-induced fluorescence thermometry measurements in a hypersonic boundary layer. In *2018 Aerodynamic Measurement Technology and Ground Testing Conference*, 2018a.

C. C. McDougall, W. S. Hinman, C. T. Johansen, B. F. Bathel, J. A. Inman, and P. M. Danehy. Quantitative analysis of planar laser-induced fluorescence measurements in a hypersonic boundary layer. In *2018 Lisbon Laser Symposium; Lisbon, Portugal.*, 2018b.

C. C. McDougall, W. S. Hinman, C. T. Johansen, B. F. Bathel, J. A. Inman, and P. M. Danehy. Evaluation of nitric oxide laser-induced fluorescence thermometry techniques in a hypersonic boundary layer. *Experiments in Fluids*, 61(4):1–19, 2020a.

C. C. McDougall, C. T. Johansen, R. Herrmann-Stanzel, P. M. Danehy, S. C. Splinter, and J. G. Gragg. Nitric oxide laser-induced fluorescence rotational thermometry in a hypersonic non-equilibrium flow. In *AIAA Scitech 2020 Forum*, page 0920, 2020b.

P. Palma, T. McIntyre, and A. Houwing. Plif thermometry in shock tunnel flows using a raman-shifted tunable excimer laser. *Shock Waves*, 8(5):275–284, 1998.

P. C. Palma et al. *Laser-induced fluorescence imaging in free-piston shock tunnels*. PhD thesis, Australian National University, 1999.

J. Palmer and R. Hanson. Single-shot velocimetry using planar laser-induced fluorescence imaging of nitric oxide. In *29th Joint Propulsion Conference and Exhibit*, page 2020, 1993.

F. Pan, R. Sánchez-González, M. H. McIlvoy, R. D. W. Bowersox, and S. W. North. Simultaneous three-dimensional velocimetry and thermometry in gaseous flows using the stereoscopic vibrationally excited nitric oxide monitoring technique. *Opt. Lett.*, 41(7):1376–1379, 2016.

J. Panda and G. Adamovsky. Laser light scattering by shock waves. *Physics of Fluids*, 7(9): 2271–2279, 1995.

C. Park. Review of chemical-kinetic problems of future nasa missions. i-earth entries. *Journal of Thermophysics and Heat transfer*, 7(3):385–398, 1993.

C. Park, G. A. Raiche, D. M. Driver, J. Olejniczak, I. Terrazas-Salinas, T. M. Hightower, and T. Sakai. Comparison of enthalpy determination methods for an arc-jet facility. *Journal of thermophysics and heat transfer*, 20(4):672–679, 2006.

J. Parker. Rotational and vibrational relaxation in diatomic gases. *The Physics of Fluids*, 2(4): 449–462, 1959.

A. Passaro, D. Carinhana Jr, E. A. Gonçalves, M. M. d. Silva, A. P. L. Guimarães, N. M. Abe, and A. M. d. Santos. The use of molecular spectra simulation for diagnostics of reactive flows. *Journal of Aerospace Technology and Management*, 3:13–20, 2011.

R. B. Pope. Measurements of enthalpy in low-density arc-heated flows. *AIAA Journal*, 6(1): 103–110, 1968.

J. R. Reisel, C. D. Carter, and N. M. Laurendeau. Einstein Coefficients for Rotational Lines of the (0,0) Band of NO. *J. Quant. Spectrosc. Radiat. Transfer*, 47(1):43–54, 1992.

M. A. Rob, L. H. Mack Jr, S. Arepalli, and C. D. Scott. Characterization of plenum spectra in an arcjet wind tunnel. *Journal of thermophysics and heat transfer*, 11(3):339–345, 1997.

T. Sakai, T. Suzuki, K. Fujita, and T. Ito. Calculation of high-enthalpy aerothermal environment in an arcjet facility. *Journal of thermophysics and heat transfer*, 21(1):249–251, 2007.

R. Sánchez-González and S. W. North. Nitric oxide laser-induced fluorescence imaging methods and their application to study high-speed flows. In *Frontiers and Advances in Molecular Spectroscopy*, pages 599–630. Elsevier, 2018.

R. Sánchez-González, R. D. Bowersox, and S. W. North. Simultaneous velocity and temperature measurements in gaseous flowfields using the vibrationally excited nitric oxide monitoring technique: a comprehensive study. *Applied optics*, 51(9):1216–1228, 2012.

R. Savino, M. D. S. Fumo, D. Paterna, A. Di Maso, and F. Monteverde. Arc-jet testing of ultra-high-temperature-ceramics. *Aerospace Science and Technology*, 14(3):178–187, 2010.

D. V. Schroeder. An introduction to thermal physics, 1999.

S. Splinter, K. Bey, J. Gragg, and A. Brewer. Comparative measurements of earth and martian entry environments in the nasa langley hymets facility. In *49th AIAA Aerospace Sciences Meeting including the New Horizons Forum and Aerospace Exposition*, page 1014, 2011.

J. Taylor. *Introduction to error analysis, the study of uncertainties in physical measurements*. 1997.

P. Ventura Diaz, S. Yoon, F. Panerai, and N. N. Mansour. Simulation of hymets flowfield around baby-sprite entry probe. In *AIAA Aviation 2019 Forum*, page 3262, 2019.

M. Winter and M. Auweter-Kurtz. Boundary layer investigation in front of a blunt body in a subsonic air plasma flow by emission spectroscopic means. In *7th AIAA/ASME Joint Thermophysics and Heat Transfer Conference*, page 2460, 1998.

M. Winter, G. Raiche, I. Terrazas-Salinas, F. Hui, B. White, and J. Taunk. Measurements of radiation heat flux to a probe surface in the nasa ames ihf arc jet facility. In *43rd AIAA Thermophysics Conference*, page 3189, 2012.

M. W. Winter, C. Srinivasan, R. Charnigo, and D. K. Prabhu. Spectroscopic analysis of nonequilibrium excited state chemistry in a nasa arc jet. *Journal of Thermophysics and Heat Transfer*, 32(4):1088–1098, 2018.

M. W. Winter, I. Terrazas-Salinas, F. C. Hui, B. White, and J. S. Taunk. Measured radiation heat flux to a probe in a nasa ames arc jet. *Journal of Thermophysics and Heat Transfer*, 33(4): 1112–1126, 2019.

J. Yoo, D. Mitchell, D. Davidson, and R. Hanson. Planar laser-induced fluorescence imaging in shock tube flows. *Experiments in fluids*, 49(4):751–759, 2010.

X. Zhang, P. Hu, J. Han, and S. Meng. Ablation behavior of zrb2–sic ultra high temperature ceramics under simulated atmospheric re-entry conditions. *Composites Science and Technology*, 68(7-8):1718–1726, 2008.

Appendix A

Energy equation derivation

Each of the governing equations begins with the equation for unsteady quasi-one-dimensional flow found in Anderson Jr [2006]. The reader is directed to that reference for the initial derivation to that point. Provided is the five governing equations (continuity, momentum, internal energy, vibrational energy and rotational energy) of a thermal non-equilibrium unsteady nozzle flow:

Continuity:

$$\frac{\partial \rho}{\partial t} = -\frac{1}{A_r}\frac{\partial(\rho u A_r)}{\partial x} \tag{A.1}$$

Momentum:

$$\frac{\partial u}{\partial t} = -\frac{1}{\rho}\left(\frac{\partial P}{\partial x} + \rho u \frac{\partial u}{\partial x}\right) \tag{A.2}$$

Internal energy:

$$\frac{\partial e}{\partial t} = -\frac{1}{\rho}\left(P\frac{\partial u}{\partial x} + \rho u \frac{\partial e}{\partial x} + Pu\frac{\partial ln(A_r)}{\partial x}\right) \tag{A.3}$$

Vibrational energy:

$$\frac{\partial \theta}{\partial t} = \frac{1}{\tau_{vib}}\left(\frac{(e_{vib})_{eq}}{e_{vib}} - 1\right) - u\frac{\partial \theta}{\partial x} \tag{A.4}$$

Rotational energy:

$$\frac{\partial \Omega}{\partial t} = \frac{1}{\tau_{rot}}\left(\frac{(e_{rot})_{eq}}{e_{rot}} - 1\right) - u\frac{\partial \Omega}{\partial x} \tag{A.5}$$

Note that the rate equations for vibrational and rotational energy are both in the Landau - Teller model form [Landau and Teller, 1936; Anderson Jr, 2006]. The continuity and momentum equations can be derived easily using term replacements described in text, therefore only the energy equation is derived below.

The energy equation is given by:

$$\frac{\partial e}{\partial t} = -\frac{1}{\rho}\left(P\frac{\partial u}{\partial x} + \rho u \frac{\partial e}{\partial x} + Pu\frac{\partial ln(A_r)}{\partial x}\right) \tag{A.6}$$

which is expanded to become

$$\rho\frac{\partial e}{\partial t}+\rho u\frac{\partial e}{\partial x}=-P\frac{\partial u}{\partial x}-Pu\frac{\partial ln(A_r)}{\partial x} \tag{A.7}$$

Note that the energy of the gas can be described as the partition of energy between modes:

$$e=\frac{3}{2}RT_t+w_d[e_{rot}+e_{vib}] \tag{A.8}$$

which is then inserted for e in Equation A:

$$\frac{3}{2}\rho R\frac{\partial T_t}{\partial t}+w_d\rho\frac{\partial e_{rot}}{\partial t}+w_d\rho\frac{\partial e_{vib}}{\partial t}+\rho u\frac{3}{2}R\frac{\partial T_t}{\partial x}+\rho u\frac{\partial e_{rot}}{\partial x}+\rho u\frac{\partial e_{vib}}{\partial x}=-P\frac{\partial u}{\partial x}-Pu\frac{\partial ln(A_r)}{\partial x} \tag{A.9}$$

From this equation divide all terms by $\frac{3}{2}\rho R$, then isolate for the term $\frac{\partial T}{\partial t}$:

$$\frac{\partial T}{\partial t}=-\frac{2}{3}\left(T\frac{\partial u}{\partial x}+Tu\frac{\partial ln(A_r)}{\partial x}+\frac{w_d}{R}\left(\frac{\partial e_{rot}}{\partial t}+\frac{e_{vib}}{\partial t}+u\frac{\partial e_{rot}}{\partial x}+u\frac{\partial e_{vib}}{\partial x}\right)\right)-u\frac{\partial T}{\partial x} \tag{A.10}$$

Replace all terms in the equation using the corresponding non-dimensionalized value, for example the vibrational energy term is replaced with:

$$e_{vib}=e'_{vib}RT_o \tag{A.11}$$

where the reference temperature T_o is the reservoir temperature. After non-dimensionalizing all terms, and making replacements based on the definitions in-text, this results in the following energy equation found in Chapter 7 (note the primed terms are non-dimensionalized):

$$\frac{\partial\phi}{\partial t'}=-\frac{2}{3}\left(u'\frac{\partial V}{\partial x'}+u'\frac{\partial ln(A'_r)}{\partial x'}+w_d(\frac{e'_{vib}}{T'_t}\frac{\partial\theta}{\partial t'}+\frac{e'_{rot}}{T'_t}\frac{\partial\Omega}{\partial t'}+u'\frac{e'_{vib}}{T'_t}\frac{\partial\theta}{\partial x'}+u'\frac{e'_{rot}}{T'_t}\frac{\partial\Omega}{\partial x'})\right)-u'\frac{\partial\phi}{\partial x'}; \tag{A.12}$$

Appendix B

Error & uncertainty analysis

This appendix summarizes the error & uncertainty analysis developed for the current work. In general, the current work corrected for sources of error, and quantified sources of uncertainty. Therefore, the only contribution to the uncertainty bars presented in the figures in this work are from uncertainty. The main method to propagate uncertainty from an input variable into the final measurement was by assessing how each variable independently affects the quantitative measurements. Each input variable was varied across it's 95% confidence interval (as recommended by ASME standards - [Abernethy et al., 1985]), and the analysis was re-completed to produce the final measurement. The range of results in the final measurement is then considered the uncertainty contribution from the varied input variable, and is summed in quadrature across other sources of uncertainty, as described later in this chapter.

Sources of error:

Sources of error in the current study were mainly mitigated with corrections or experimental design decisions produced by the initial studies. Examples of sources of error that have been corrected or removed from the study include laser saturation and laser linewidth measurements. Some errors were treated as uncertainty, for example the rotation correction. Likely, the rotation correction was not perfect when applied, and skewed the image a certain direction, introducing a systematic error. However, completing a sensitivity analysis by acquiring the measurement multiple times, the current work was able to capture the uncertainty introduced by that measurement. Sensitivity analysis was applied to many of the preprocessing steps to capture the uncertainty in that measurement.

Sources of uncertainty:

The strategy to quantify uncertainty was to complete sensitivity analysis of a number of input variables that the quantitative measurements are dependent on. This subsection reviews the sources of uncertainty, and how that uncertainty was quantified. Each source of uncertainty is then propagated into the measurement through the sensitivity analysis described.

Run repeatability is an important factor to consider when characterizing a facility like the current work aims to do. The uncertainty in run conditions is accounted for in the current study by acquiring multiple data sets at the 5.7 MJ/kg enthalpy condition such that analysis can be performed on both sets, and the uncertainty can be quantified as it propagates into the measurements.

Flow unsteadiness introduces fluctuations in the thermodynamic and flow variables that describe the arc-jet flow. Therefore, this unsteadiness also propagates into the NO-PLIF data, and affects the accuracy of quantitative measurements. In spectral scans, this manifests as noise overlayed on top of the spectra. Therefore, this uncertainty is captured during the NLLS fitting processes of DSV, SPT and DBT, where an associated uncertainty is produced for the respective fit parameter.

The rotation correction completed in the preprocessing part of the analysis pipeline potentially introduces a spatial measurement error. Since the correct rotation angle cannot be exactly known, this error can be quantified by applying the correction multiple times to observe any differences introduced by user error. The upper and lower limits of this range of rotation angles was taken and considered the uncertainty in the rotation correction.

The scaling correction is completed in a similar way as the rotation correction. Therefore, this uncertainty is treated the same way.

The gas cell study uses a similar methodology of fitting a Gaussian, therefore this source of uncertainty is treated similarly to the pulse energy correction uncertainty above.

The saturation study contributes uncertainty due to the fitting procedure used in the study. There is an associated uncertainty with the I_{SAT} value fit, where the 95% confidence interval is

considered the uncertainty in this value.

Propagation of uncertainty:

The total uncertainty in a measurement is normally calculated by using the propagation of uncertainty technique [Taylor, 1997]. Due to the sensitivity analysis produced in the current work, all uncertainties are already defined on the final measurement itself, and are all considered to be uncorrelated. Therefore, the uncertainties can be summed in quadrature [Taylor, 1997]:

$$\Delta_{total}^2 = \sum^{i} \Delta_i^2 + \Delta_{i+1}^2 \cdots \tag{B.1}$$

where Δ_{total} is the total uncertainty of the measurement, and Δ_i is a contribution of uncertainty to the measurement. This equation is used to estimate the total uncertainty on a quantitative measurement due to contributions from each sensitivity analysis.

Initial studies:

Table B.1 identifies the sources of uncertainty that were used with Equation B to determine the total uncertainty on a measurement. Notably absent is the run repeatability source of uncertainty, since each of these studies only had 1 experimental run.

Table B.1: Uncertainty contributions in initial studies.

	Unsteadiness min. study	Saturation study	Gas cell study
Variable/Figure:	Figure 5.8b	I_{SAT}	I_L
Sources of Uncertainty:			
Run repeatability	X	X	X
Flow unsteadiness	✓	✓	✓
Rotation correction	✓	✓	✓
Scaling correction	✓	✓	✓
Saturation value			
Linewidth value			

✓ = applicable & included; X = applicable, not included; blank = N/A

Quantitative measurements:

Table B.2 identifies the sources of uncertainty that were used with Equation B to determine the total uncertainty on a measurement.

Table B.2: Uncertainty contributions in quantitative measurements.

	DSV	SPT	DBT
Variable/Figure:	V_r	T_r	T_t
Sources of Uncertainty:			
Run repeatability	X	✓	X
Flow unsteadiness	✓	✓	✓
Rotation correction	✓	✓	✓
Scaling correction		✓	
Saturation value		✓	
Linewidth value			✓

✓ = *applicable & included; X = applicable, not included; blank = N/A*

Sample calculation:

This section provides a sample uncertainty calculation for the radial velocity at x = 12 mm, y = 35 mm for the 5.7 MJ/kg enthalpy condition.

Δ_{RU} - Rotation correction:

There is an uncertainty in the rotation angle to bring the PLIF image in line with the pixel grid. In the current work, the rotation angle was 1.8 $\pm$ 0.2 degrees. This analysis produces three image stacks, which are each used to produce a radial velocity measurement with DSV. The range of velocities varied by 6.4 m/s, or $\pm$ 3.2 m/s around the mean velocity, which is considered the associated uncertainty due to rotation.

Δ_{UU} - Flow unsteadiness:

Flow unsteadiness is taken into account in the spectral fit completed during DSV. The associated 95% confidence interval with the fit parameter V_R is given as 456 $\pm$ 31 m/s.

Sample calculation:

$$\Delta_{total} = \sqrt{\Delta_{RU}^2 + \Delta_{UU}^2} \tag{B.2}$$

$$\Delta_{total} = \sqrt{(3.2)^2 + (31)^2} \tag{B.3}$$

$$\Delta_{total} = 31.1448 m/s \approx 31 m/s \tag{B.4}$$

Appendix C

Spectral line filtering technique

The analysis outlined in this appendix was not used to produce results in the current work, however it was used to produce results for a prior publication [McDougall et al., 2020b]. Due to the evidence of trans-rotational non-equilibrium found using ARC1D and in the experimental data, this method was unusable due to the assumption that the translational and rotational temperatures were in equilibrium. In short, the work in this appendix depends on the translational temperature (determined by the DBT method) to be used as a "first guess" in a numerical method that systematically eliminates transitions that have been significantly affected by absorption, saturation, or any other effects. Refer to the following paragraphs taken from McDougall et al. [2020b] for a more detailed explanation.

Time-averaged temperature field

The method developed uses Doppler thermometry to acquire a first temperature guess. The spectral widths of the LIF transitions are analyzed to compute a translational temperature. Factors such as laser linewidth and broadening mechanisms contribute to the overall transition width. The Doppler broadening term is dependent on the translational temperature, and can be back-calculated if the other terms contributing to the transition width are known. Unfortunately, complex effects such as saturation and velocity fluctuations artificially broaden the transition, which increases the measured Doppler broadening width. In the current work, saturation effects are accounted for by measuring the transition width at two saturation levels, subtracting the laser linewidth from the measured width, and extrapolating the unsaturated width using fluorescence theory [Demtröder, 2013]. After recording the translational temperature and associated error, two-line rotational thermometry is performed on all combinations of transitions in the spectral range. While the flow is

expected to experience vibrational non-equilibrium, the rotational and translational temperatures are expected to be in thermal equilibrium [Brune et al., 2019]. Using the translational temperature and associated error, transition pairs returning a rotational temperature value outside of the translational temperature error estimate are eliminated from the two-line thermometry set. From these combinations, the best transitions are identified by quantifying how frequently they produce a rotational temperature within the error bounds of Doppler-based thermometry, which is an indicator of robustness. These best-performing transitions, currently identified as being present in two or more two-line thermometry pairs, are then chosen for multi-line thermometry. This process selects approximately 60% of the transitions, which are then used in the thermometry analysis. The spectra and multi-line model are filtered for the best-performing transitions, and an NLLS regression is performed, leaving temperature as a free parameter. This method produces a rotational temperature based on the most accurate transitions. Both filtered and unfiltered fits for temperature are compared.

Verification

To verify the methodology outlined above, a computer-simulated spectra was generated with added Gaussian noise (10%) to approximate the experimental spectra. The spectra was generated with a temperature of 600 K to approximately match the CFD free-stream temperature predicted by Brune et al. [2019]. The transitions within the synthetic spectra were then saturated equally, and repeated at different saturation levels to determine the effectiveness of the filtered thermometry technique. The most temperature sensitive and least temperature sensitive transitions were subjected to saturation ratios (I_L/I_{SAT}) of 0.1, 0.25 and 1. The spectral fits for regular multi-line thermometry and filtered multi-line thermometry are shown in Figures C.1 and C.2, where the saturation ratio is $I_L/I_{SAT} = 0.25$. The conventional multi-line method predicts a temperature approximately 50 K (approximately 8%) less than the true generated temperature. The transition filtering procedure greatly improves agreement to within 10 K (within 1.5 % of the true temperature). Similar im-

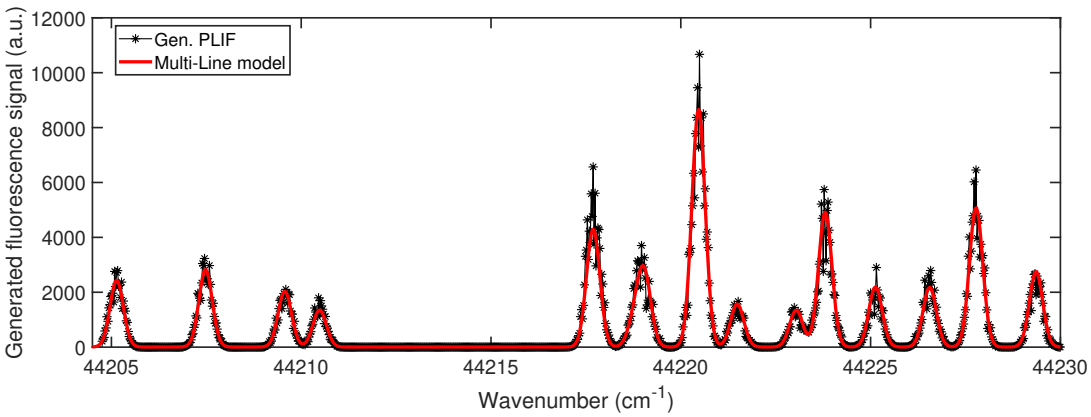

Figure C.1: Multi-line thermometry fit to a full synthetic PLIF spectra corresponding to 600 K. Fitted temperature = 555 K.

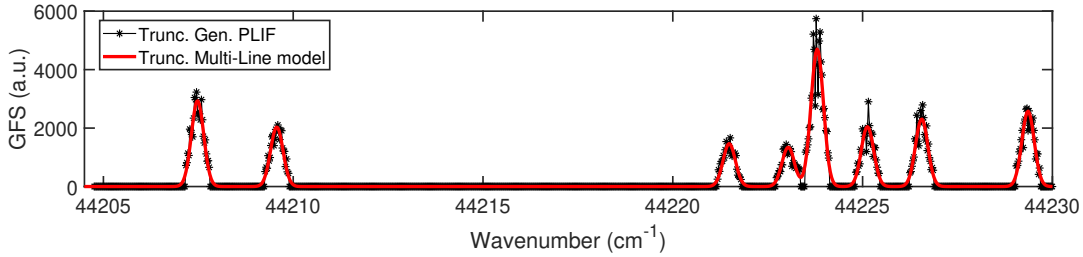

Figure C.2: Multi-line thermometry fit to filtered synthetic PLIF spectra with a corresponding temperature of 600 K. Fitted temperature = 596 K.

provement was observed for the other saturation ratios tested. This transition filtering procedure was also completed for a simulated spectra with a randomly saturated transition at a saturation ratio of $\frac{I_L}{I_{SAT}} = 0.1$. 1000 spectra were generated for this study, each with a randomized transition selected to be saturated. Agreement achieved for filtered multi-line thermometry was within 19.2 K (within 3% of the true temperature), while conventional multi-line thermometry achieved agreement within 54.7 K (8.5%) of the generated LIF temperature. Most importantly, the multi-line thermometry (using all transitions) never out-performed the filtered multi-line thermometry.

Validation

To validate the filtered multi-line LIF thermometry, a NO PLIF experiment was performed in a room temperature (300 K) gas cell. The gas cell contained 5% NO and 95% nitrogen (N_2) at 6.5

kPa (compared to 0.5 kPa free-stream and 15 kPa post-shock in the HyMETS facility for Run 1) and was placed within the HyMETS test section while the facility was not running. Rotational temperature was obtained from both the conventional and filtered multi-line techniques applied to the gas cell PLIF data over the first spectral range (A). The filtered multi-line thermometry technique improved agreement with ambient temperature (300 K) when compared to conventional multi-line thermometry (3.4% vs. 7.6% disagreement, respectively). The absolute temperature difference was 283 K $\pm$ 23 K and 311 K $\pm$ 13 K for full multi-line thermometry and filtered multi-line thermometry, respectively. The error range reported represents the 95% confidence interval extracted from the NLLS fit when using the multi-line SPT algorithm. The filtered multi-line technique reduces the uncertainty when compared to conventional multi-line thermometry.

Summary

Due to the determination that trans-rotational non-equilibrium was occurring in the flow, this method was unusable. In retrospect, the verification and validation procedures were not sufficient to apply this method to an arc-jet facility. There needed to be complete certainty of the assumption that the translational and rotational temperatures were in equilibrium. Further, the verification process made the same assumptions, while the validation process used a gas cell at equilibrium. This work is from McDougall et al. [2020b].